

ANALYSIS OF CANADIAN TROPOSPHERIC OZONE
MEASUREMENTS FROM GEOSTATIONARY ORBIT
AND AN ASSESSMENT OF NON-COINCIDENT
LIMB-NADIR MATCHING FOR MEASURING
TROPOSPHERIC NITROGEN DIOXIDE

A thesis submitted to the
College of Graduate and Postdoctoral Studies
in partial fulfillment of the requirements
for the degree of Master of Science
in the Department of Physics and Engineering Physics
University of Saskatchewan by

Ian McConkey

©Ian McConkey, May 2021. All rights reserved.

Unless otherwise noted, copyright material in this thesis belongs to
the author.

Permission to Use

In presenting this thesis in partial fulfillment of the requirements for a Postgraduate degree from the University of Saskatchewan, I agree that the Libraries of this University may make it freely available for inspection. I further agree that permission for copying of this thesis in any manner, in whole or in part, for scholarly purposes may be granted by the professor or professors who supervised my thesis work or, in their absence, by the Head of the Department or the Dean of the College in which my thesis work was done. It is understood that any copying or publication or use of this thesis or parts thereof for financial gain shall not be allowed without my written permission. It is also understood that due recognition shall be given to me and to the University of Saskatchewan in any scholarly use which may be made of any material in my thesis.

Disclaimer

Reference in this thesis to any specific commercial products, process, or service by trade name, trademark, manufacturer, or otherwise, does not constitute or imply its endorsement, recommendation, or favoring by the University of Saskatchewan. The views and opinions of the author expressed herein do not state or reflect those of the University of Saskatchewan, and shall not be used for advertising or product endorsement purposes.

Requests for permission to copy or to make other uses of materials in this thesis in whole or part should be addressed to:

Head of the Department of Physics and Engineering Physics
University of Saskatchewan
163 Physics Building, 116 Science Place
Saskatoon, Saskatchewan S7N 5E2

Canada

OR

Dean

College of Graduate and Postdoctoral Studies

University of Saskatchewan

116 Thorvaldson Building, 110 Science Place

Saskatoon, Saskatchewan S7N 5C9

Canada

Abstract

This thesis work attempts to improve the quality of surface-level pollutant concentrations retrieved from satellite-borne optical instruments. In the first part of the present work, an analysis is performed to determine potential benefits of implementing a different radiative transfer model than the one planned for retrieving Canadian tropospheric ozone concentrations with future measurements from the Tropospheric Emissions: Monitoring of Pollution (TEMPO) optical instrument, planned to be launched in 2022 into geostationary orbit to measure tropospheric pollutants over the majority of North America. The plane-parallel Earth-atmosphere geometry assumption for multiple-scattered electromagnetic radiation in the planned radiative transfer model for the TEMPO ozone retrieval algorithm has minimal effect for heritage instruments that look at angles close to straight down and measure at local times where the Sun is far above the horizon. However, it is demonstrated in the present work for simulated TEMPO measurements over the Canadian Oil Sands that the retrieval error for a radiative transfer model with a plane-parallel geometry can reach approximately 15% at 13:00 local time, 25% in March or September near local sunrise, 50% in June near local sunrise, and 80% in December near local sunrise, while a radiative transfer model with a spherical geometry results in error up to an order of magnitude smaller in each case. Further work is required to assess the effects of the geometry assumptions on different orders of scattering and of measurement noise. In the second part of the present work, a novel method of estimating tropospheric NO₂ pollution using non-coincident limb- and nadir-viewing instrument measurements is further assessed with a reanalysis using new datasets produced by the Ozone Monitoring Instrument (OMI), the Optical Spectrograph and Infrared Imager System (OSIRIS), and a photochemical box model, and an analysis using OSIRIS and the TROPospheric Monitoring Instrument (TROPOMI). A bias is demonstrated in the current publicly available OSIRIS NO₂ density profile data, leading to the development of an updated dataset that is shown to agree with a previously validated dataset within retrieval error bounds above the tropopause. The OSIRIS-OMI reanalysis demonstrates biases of up to 0.5×10^{15} molecules/cm² due to the different photochemical box model input param-

ters and up to 0.2×10^{15} molecules/cm² due to the use of the latest OMI NO₂ dataset. The OSIRIS-TROPOMI analysis demonstrates a positive average bias of approximately 0.5×10^{15} molecules/cm² in the limb-nadir matching with TROPOMI relative to that with OMI due to TROPOMI-OMI tropospheric and stratospheric NO₂ column density biases. Error range estimates of photochemical box model input parameters and of different versions of OMI datasets, further analysis of local and yearly dependencies of OSIRIS-OMI limb-nadir matching biases, and further studies on latitudinal and seasonal dependencies of TROPOMI-OMI dataset biases are recommended for future work.

Acknowledgements

I would first like to thank my supervisors Adam Bourassa and Doug Degenstein for providing endless guidance and encouragement throughout my master's degree and studies.

I am thankful to Cristen Adams for taking the time to answer questions and share sample data from her work to enhance my analysis, Chris McLinden for providing insight and connecting me with collaborators to answer my questions, and Lok Lamsal and Nickolay Krotkov for providing details of their work to aid in my analysis.

I am grateful for the valuable input and assistance from my colleagues of Physics Room 312, especially Daniel Zawada and Chris Roth.

I would like to thank the many friends who have supported me throughout my studies in Saskatoon.

Finally, I am forever thankful to my parents for always encouraging me, sharing their wisdom with me, and acting as role models for my life.

Contents

Permission to Use	i
Abstract	iii
Acknowledgements	v
Contents	vi
List of Figures	ix
List of Abbreviations	xiv
List of Symbols	xv
1 Introduction	1
2 Background	6
2.1 Atmospheric Remote Sensing	6
2.1.1 Atmosphere	6
2.1.2 Instrument Geometries	7
2.1.3 Instrument Sensors	10
2.2 Radiative Transfer	11
2.2.1 Radiometric Quantities	11
2.2.2 Scattering and Absorption	12
2.2.3 Reflection	13
2.2.4 Beer-Lambert Law	14
2.2.5 Radiative Transfer Equation	15
2.2.6 Successive Orders of Scattering	17
2.2.7 SASKTRAN	18
2.2.8 Example Simulated Radiances	19
2.2.8.1 Limb versus Nadir	19
2.2.8.2 Engine Comparison	22
2.3 Atmospheric Ozone and Nitrogen Dioxide	23
2.3.1 Ozone and Nitrogen Oxide Pollution	23
2.3.2 Diurnal Variations of Nitrogen Oxides	24
2.3.3 Remote Sensing of Tropospheric Ozone and Nitrogen Dioxide	26
2.4 Relevant Instruments and Retrieval Algorithms	29
2.4.1 OMI	29
2.4.2 TROPOMI	31
2.4.3 OSIRIS	32
2.4.4 GOME	33

2.4.5	TEMPO	33
2.4.6	MLS	35
2.5	Optimal Estimation	35
2.5.1	Derivation	36
2.5.2	Averaging Kernel Matrix	38
2.5.3	Levenberg-Marquardt Method and Convergence Criteria	39
2.6	Non-Coincident Limb-Nadir Matching	40
3	Analysis of Canadian Ozone Retrievals for Simulated TEMPO Measure-	
	ments	45
3.1	Introduction	45
3.2	Methodology	46
3.2.1	Atmospheric Model	46
3.2.2	Measurements and Instrument Models	47
3.2.3	Retrieval Parameters	48
3.2.4	GOME-Based Retrievals	50
3.2.4.1	Validation	51
3.2.5	OMI-Based Retrievals	51
3.2.5.1	Validation	52
3.2.6	TEMPO-Based Retrievals	53
3.2.6.1	Statistical Analysis	54
3.2.6.2	HRSSApprox Engine	55
3.2.6.3	Example Retrieval	58
3.3	Results and Discussion	62
3.3.1	GOME-Based Retrievals	62
3.3.2	OMI-Based Retrievals	66
3.3.3	TEMPO-Based Retrievals	68
3.4	Conclusion	75
4	Assessment of Non-Coincident Limb-Nadir Matching for Measuring Tro-	
	pospheric Nitrogen Dioxide	77
4.1	Introduction	77
4.2	Methodology	78
4.3	Results	79
4.3.1	OSIRIS NO ₂ Data Version Comparison	79
4.3.2	OSIRIS Gridded Stratospheric NO ₂ VCD Maps	82
4.3.3	OSIRIS-OMI Limb-Nadir Matching Reanalysis	87
4.3.4	OMI-minus-OSIRIS Product Validation	90
4.3.5	OSIRIS-TROPOMI Limb-Nadir Matching Analysis	93
4.3.6	TROPOMI-minus-OSIRIS Product Validation	94
4.4	Discussion	96
4.4.1	OSIRIS Gridded Stratospheric NO ₂ VCD Maps	96
4.4.2	OSIRIS-minus-OMI Tropospheric NO ₂ VCDs	96
4.4.3	TROPOMI-minus-OSIRIS Tropospheric NO ₂ VCDs	98
4.5	Conclusion and Future Work	99

4.5.1	Conclusion	99
4.5.2	Future Work	101
5	Conclusion	102
5.1	Conclusions	102
5.2	Future Work	104
	References	106
	Appendix A Maximum Latitude Difference Between TEMPO Line of Sight Intersections with Atmospheric Layers	114
	Appendix B Time Offset Between MLS and OMI Measurements Over the Same Geographic Location	116

List of Figures

2.1	Common remote sensing instrument viewing geometries for low-Earth orbits (LEOs) and geostationary orbits. The lines in each case show the edges of the range of viewing angles. The orbit altitudes and viewing angles are exaggerated for illustrative purposes.	8
2.2	Instrument viewing geometry parameters: viewing zenith angle (VZA), solar zenith angle (SZA), solar scattering angle (SSA), tangent point (TP), and tangent point altitude (z) for nadir- and limb-viewing instrument geometries.	9
2.3	Geometry for defining radiance.	12
2.4	Effect of the instrument viewing geometry on the Sun-normalized measured radiances simulated in the SASKTRAN HR engine for wavelengths relevant to the remote sensing instruments discussed herein, for an instrument at an altitude of 650 km, and for a set of solar zenith angles (SZAs). For the nadir geometry, the instrument is pointed towards 44°N-150°W with a viewing zenith angle of approximately 1°. For the limb geometry, the tangent-point is 20 km above 44°N-150°W.	21
2.5	Typical ozone absorption cross sections over wavelengths relevant to the remote sensing instruments discussed herein. Cross sections are taken from experimentally determined data (Brion et al., 1998; Brion et al., 1993; Daumont et al., 1992; Malicet et al., 1995) for the temperature at an altitude of 20 km above 0°N-0°E on 21 March 2008 in the MSIS-90 model (Hedin, 1991).	21
2.6	Comparison of the effect of using either the HR or DO SASKTRAN engine on the Sun-normalized measured radiances simulated for an instrument in geostationary orbit above 0°N-100°W, pointing towards the Canadian Oil Sands (57°N-112°W), one hour past local sunrise on the 21 st day of four different months in 2022. The solar zenith angle (SZA) corresponding to each measurement scenario is shown.	23
2.7	Empirically-derived diurnal dependencies of NO and NO ₂ volumetric concentrations (in parts per billion) near an altitude of 19 km, adapted from Wennberg et al. (1994). The diurnal dependencies are verified by Wennberg et al. (1994) using chemiluminescence and laser-diode absorption instrument measurements on 12 May 1993.	25

2.8	Typical ozone and NO ₂ absorption cross sections over wavelengths relevant to the remote sensing instruments discussed herein. Cross sections are taken from experimentally determined data (Brion et al., 1998; Brion et al., 1993; Daumont et al., 1992; Malicet et al., 1995; Vandaele et al., 1998) for the temperature at an altitude of 20 km above 0°N-0°E on 21 March 2008 in the MSIS-90 model (Hedin, 1991).	27
2.9	Ozone and NO ₂ vertical density profiles taken from respective climatological datasets by Prather and Jaffe (1990) and McPeters et al. (1997). Each profile shown is the average of profiles from ten uniformly separated days of the given month. Each NO ₂ profile is taken at 13:00 local time.	27
2.10	OMI viewing geometry, adapted from Bucsele et al. (2016). Relative lengths are exaggerated for illustrative purposes.	30
2.11	The TEMPO field of regard, with boundary data extracted from Zoogman et al. (2017).	34
3.1	Subset of TEMPO wavelengths (vertical orange lines) used to calculate the multiple-scatter contribution exactly in the HRSSApprox engine, overlaid on the ozone cross section taken from experimentally-determined data (Brion et al., 1998; Brion et al., 1993; Daumont et al., 1992; Malicet et al., 1995) for the temperature at an altitude of 20 km above 0°N-0°E on 21 March 2008 in the MSIS-90 model (Hedin, 1991).	56
3.2	Comparison of Sun-normalized radiances between the HRSSApprox and HR engines, simulated for the TEMPO instrument positioned at an altitude of 35 786 km above 0°N-100°W, pointing towards 57°N-112°W. The background and Sun are set for one hour past local sunrise on 21 March 2022, and the ozone profile is set using MLS retrieval results on 21 March 2017 at 56.1°N-112.8°W.	57
3.3	Ozone profiles for an example retrieval with a simulated TEMPO measurement over the Canadian Oil Sands (57°N-112°W) on 21 March 2022, with the true ozone profile taken from an MLS-retrieved profile on 22 March 2017. The surface albedo is 0.5. The dotted blue line denotes the true ozone profile (\mathbf{x}_{true}) used for the simulated TEMPO measurement and the dashed green line denotes the true ozone profile adjusted by the averaging kernel matrix ($\mathbf{x}_{\mathbf{a}} + A[\mathbf{x}_{\text{true}} - \mathbf{x}_{\mathbf{a}}]$).	59
3.4	Forward model UV radiance measurements for the same example TEMPO retrieval scenario as that used for the results of Fig. 3.3. The top plot shows the log of the Sun-normalized radiances and the bottom plot shows the difference in the log of the Sun-normalized radiances relative to that for the true atmospheric state.	60
3.5	Forward model visible light radiance measurements for the same example TEMPO retrieval scenario as that used for the results of Fig. 3.3. The top plot shows the log of the Sun-normalized radiances and the bottom plot shows the difference in the log of the Sun-normalized radiances relative to that for the true atmospheric state.	61

3.6	Comparison of the GOME-based ozone retrieval algorithm weighting functions from the present work to those of Hoogen et al. (1999), for a typical northern midlatitude winter scenario, solar zenith angle of 70° , and surface albedo 0.8.	63
3.7	Effect of varying the <i>a priori</i> standard deviation (std) factor (ratio of the standard deviation to the mean for the <i>a priori</i> number density) on the GOME-based ozone retrieval averaging kernels for the same scenario as Fig. 3.6. The nominal altitude is the altitude of the true ozone profile on which the retrieved profile is dependent. The true altitude is the altitude of the peak of the averaging kernel.	65
3.8	Effect of varying the <i>a priori</i> standard deviation (std) factor (ratio of the standard deviation to the mean for the <i>a priori</i> number density) on the GOME-based ozone retrieval, for the same cases as Fig. 3.7. The dotted blue line is the true ozone profile (\mathbf{x}_{true}) used for the simulated instrument measurement and the dashed green line is the true ozone profile adjusted by the averaging kernel matrix ($\mathbf{x}_{\mathbf{a}} + A[\mathbf{x}_{\text{true}} - \mathbf{x}_{\mathbf{a}}]$).	66
3.9	Percent error of OMI-based retrieval number densities ($[n_{\text{retrieved}} - n_{\text{true}}]/n_{\text{true}}$) for a path from one terminator (at 78°S) to the other (at 81°N) of an Aura satellite orbit on 31 March 2012. The top row of plots compares to the true profiles (\mathbf{x}_{true}) and the bottom row of plots compares to the true profiles adjusted by the averaging kernel matrix ($\mathbf{x}_{\mathbf{a}} + A[\mathbf{x}_{\text{true}} - \mathbf{x}_{\mathbf{a}}]$). The <i>a priori</i> profile standard deviation is 1.5 times the <i>a priori</i> profile in the first column of plots and 10 times the <i>a priori</i> profile in the second column of plots. . . .	68

3.10	TEMPO-based retrievals: <i>a priori</i> ozone profiles and the mean and standard deviation (shaded region) of the true ozone profiles for the statistical analysis.	69
3.11	TEMPO-based retrievals: Mean and standard deviation (shaded region) of the retrieved ozone profile at 13:00 local time.	71
3.12	TEMPO-based retrievals: Mean and standard deviation (shaded region) of the retrieved ozone profile at one hour past local sunrise.	72
3.13	TEMPO-based retrievals: Mean and standard deviation (shaded region) of the error in the retrieved ozone profile at 13:00 local time.	73
3.14	TEMPO-based retrievals: Mean and standard deviation (shaded region) of the error in the retrieved ozone profile at one hour past local sunrise.	74
4.1	Mean difference between version 6 and version 3 OSIRIS stratospheric NO ₂ density profiles in 2008 for 5° latitude bins between 70°S and 70°N. Grey indicates regions that are below the tropopause year-round.	80
4.2	Mean difference between version 7 and version 3 OSIRIS stratospheric NO ₂ density profiles, and mean version 7 retrieved profile error, in 2008 for 5° latitude bins between 70°S and 70°N. The colour mapping in (a) and (c) is the same as in Fig. 4.1(a) and the colour mapping of (b) is the same as in Fig. 4.1(b). Grey indicates regions that are below the tropopause year-round.	81
4.3	Comparison of 2008 gridded OSIRIS stratospheric NO ₂ VCD maps between (a) version 6 (present work), (b) version 7 (present work), and (c) version 3 (Adams et al., 2016) OSIRIS profile data. In each case, maps are shown for 4 March and 21 June 2008 (columns of maps for each subfigure) at local solar time 07:00 and 13:00 (rows of maps for each subfigure). The white or grey circles in each map show the tangent-point coordinates of OSIRIS measurements used to construct the map.	83
4.4	Difference in OSIRIS gridded stratospheric NO ₂ VCD maps on 4 March 2008 at 07:00 (first column) and 13:00 (second column) local time due to the algorithm version (top row), OSIRIS NO ₂ version (middle row), and PRATMO photochemical box model dataset (bottom row). The algorithms from the present work and from Adams et al. (2016) are denoted by “algo. 2019” and “algo. 2016”, respectively. The grey circles show the tangent-point latitude and longitude for each OSIRIS measurement used in producing the map. Grey indicates regions where there are insufficient nearby OSIRIS measurements to define these grid points of the map.	85
4.5	Percent difference in OSIRIS gridded stratospheric NO ₂ VCD maps on 4 March 2008 at 07:00 (first column) and 13:00 (second column) local time due to the algorithm version (top row), OSIRIS NO ₂ version (middle row), and PRATMO photochemical box model dataset (bottom row). The algorithms from the present work and from Adams et al. (2016) are denoted by “algo. 2019” and “algo. 2016”, respectively. The grey circles show the tangent-point latitude and longitude for each OSIRIS measurement used in producing the map. Grey indicates regions where there are insufficient nearby OSIRIS measurements to define these grid points of the map.	86

4.6	2008 mean stratospheric NO ₂ vertical column densities (VCDs) in 10° latitude bins for measurements where OMI tropospheric VCDs are less than 0.5×10^{15} molecules/cm ² . The OMI-SP version 2 data is adapted from Adams et al. (2016), where correction factors of Marchenko et al. (2015) are used to account for the positive bias in the version 2 slant column densities.	87
4.7	Monthly mean and standard deviation (shaded areas) of OSIRIS version 7 minus OMI-SP version 4 stratospheric NO ₂ VCDs for 10° latitude bins. Starting at the 65°S-centered bin, each plot line of the following latitude bin is offset by 1×10^{15} molecules/cm ² from the previous plot line. The offsets are shown as dashed black lines.	88
4.8	Mean 2008 OmO, OMI, and OmO-minus-OMI tropospheric VCD maps for a 1° × 1° latitude-longitude grid. OSIRIS version 7 and OMI-SP version 4 NO ₂ datasets are used.	89
4.9	Mean OMI-minus-OSIRIS (OmO) tropospheric NO ₂ VCDs for 2° latitude bins from 2005 to 2019. White corresponds to $+3 \times 10^{14}$ molecules/cm ² . OSIRIS version 7 and OMI-SP version 4 data is used.	90
4.10	Comparison between OmO and OMI changes in tropospheric NO ₂ VCDs relative to 2005. The regions are the same as those used for Fig. 3 of Krotkov et al. (2016); from top to bottom: Ohio River Valley and southwestern Pennsylvania (corners 38°N-81.6°W, 39°N-83°W, 40.6°N-78°W, 41.7°N-79.2°W), Maritsa Iztok power plants in Bulgaria (bounded by 40.5-43.8°N, 23.7-28.1°E), North China Plain (bounded by 34-38°N, 112-118°E), Chhattisgarh and Odisha (bounded by 21-25°N, 81-85°E), and the Persian Gulf (corners 22.6°N-54.1°E, 25.6°N-56.5°E, 29.5°N-46.9°E, 30.6°N-49.8°E).	92
4.11	Comparison of TROPomO (left column) and OmO (right column) tropospheric VCD maps for 2018-10-19 (first row), 2018-12-20 (second row), 2019-03-03 (third row), and 2019-05-18 (last row). The maps result from OSIRIS version 7, OMI-SP version 4, and TROPOMI version 1.3 NO ₂ data.	94
4.12	Mean and standard deviation (shaded regions) of OMI and TROPOMI results over the Pacific (180°W-150°W) for 2018-10-19, 2018-12-20, 2019-03-03, and 2019-05-18. OSIRIS version 7, OMI-SP version 4, and TROPOMI version 1.3 NO ₂ data are used.	95
A.1	Geometry of TEMPO line of sight atmospheric intersections when measuring towards the Canadian Oil Sands. Lengths and angles are not to scale.	115
B.1	Depiction of Aura linear distance offset and angular offset between an MLS tangent-point measurement at time $t = t_0$ and the point at time $t = t_0 + t_{\text{offset}}$ where OMI measures over the tangent-point latitude and longitude of said MLS measurement. r_{Earth} is the average radius of the Earth, z_{sat} is the average altitude of the Aura satellite above the mean Earth radius, and z_{tan} is the tangent-point altitude at time $t = t_0$. Lengths and angles are not to scale. . .	116

List of Abbreviations

AMF	Air mass factor
DO	Discrete Ordinates (SASKTRAN engine)
ERS-2	Second European Remote Satellite
ESA	European Space Agency
ETA	Effective top of the atmosphere
ETS	Effective top of the stratosphere
GMI	Global Modeling Initiative
GOME	Global Ozone Monitoring Instrument
HR	High Resolution (SASKTRAN engine)
HRSSApprox	High Resolution Single-Scatter Approximation (SASKTRAN engine)
SI	International System of Units
LEO	Low Earth orbit
LIDORT	LInearized Discrete Ordinates Radiative Transfer
LM	Levenberg-Marquardt (method)
LOS	Line of sight
MJD	Modified Julian Date
MLS	Microwave Limb Sounder
NASA	National Aeronautics and Space Administration
OMI	Ozone Monitoring Instrument
OmO	OMI-minus-OSIRIS
OSIRIS	Optical Spectrograph and InfraRed Imaging System
SAA	Solar azimuth angle
SCD	Slant column density
SCIAMACHY	SCanning Imaging Absorption SpectroMeter for Atmospheric CHartographY
SSA	Solar scattering angle
SZA	Solar zenith angle
TEMPO	Tropospheric Emission: Monitoring of POLLution
TROPOMI	TROPospheric Monitoring Instrument
TROPOmO	TROPOMI-minus-OSIRIS
UV	Ultraviolet
VAA	Viewing azimuth angle
VCD	Vertical column density
VLIDORT	Vector LInearized Discrete Ordinates Radiative Transfer
VZA	Viewing zenith angle

List of Symbols

λ	Wavelength
$d\Omega$	Solid angle differential element
$\hat{\Omega}$	Unit vector in the propagation direction
α	Area
\hat{n}	Unit vector normal to the differential area element $d\alpha$
θ	Angle between the propagation direction ($\hat{\Omega}$) and the normal (\hat{n}) of the differential area element ($d\alpha$)
E	Energy
t	Time
\mathbf{r}	Position in three-dimensional space
I	Spectral radiance, units of $\text{W cm}^{-2} \text{nm}^{-1} \text{sr}^{-1}$
F	Spectral irradiance, units of $\text{W cm}^{-2} \text{nm}^{-1}$
a	Surface albedo
s	Path length coordinate
\mathbf{r}_0	Reference point (usually at the observer); position where the path length coordinate is $s = 0$
V	Volume
N	Number of particles
k_{scatt}	Scattering extinction
k_{abs}	Absorption extinction
k	Total extinction
n	Number density, units of molecules cm^{-3}
σ_{scatt}	Scattering cross section
σ_{abs}	Absorption cross section
$\tau(s_0, s_1, \hat{\Omega})$	Optical depth from point $\mathbf{r}(s_0)$ to $\mathbf{r}(s_1)$ in direction $\hat{\Omega}$
J	Volume emission rate, units of $\text{W cm}^{-3} \text{nm}^{-1} \text{sr}^{-1}$
$\bar{p}(s, \hat{\Omega}', \hat{\Omega})$	Effective phase function at position $\mathbf{r}(s)$ from direction $\hat{\Omega}'$ to $\hat{\Omega}$
τ_s	Optical depth from the point with path coordinate s to the reference point \mathbf{r}_0
I^{end}	Radiance at the end of the instrument line of sight
I_i	Radiance resulting from electromagnetic radiation that has scattered i times
z	Altitude
\mathbf{x}	Atmospheric state vector
\mathbf{y}	Measurement vector
\mathbf{S}_y	Measurement covariance matrix
\mathbf{x}_a	<i>A priori</i> atmospheric state vector
\mathbf{S}_a	<i>A priori</i> atmospheric state covariance matrix
$F(\mathbf{x})$	Retrieval algorithm forward model for atmospheric state \mathbf{x}

χ^2	Cost function for the optimal estimation algorithm
$\mathbf{g}(\mathbf{x})$	Negative gradient of the logarithm of the <i>a posteriori</i> probability distribution, $P(\mathbf{x} \mathbf{y})$
\mathbf{K}	Weighting function matrix
\mathbf{x}_i	Atmospheric state at iteration i of the retrieval algorithm
\mathbf{A}	Averaging kernel matrix
δ	Levenberg-Marquardt damping factor
$\mathbf{x}_{\text{GN},i}$	Atmospheric state vector at iteration i calculated using the Gauss-Newton method
d	Date
V_{trop}	Tropospheric vertical column density
V_{strat}	Stratospheric vertical column density
Θ	Latitude
Φ	Longitude
Θ_i	Latitude for the i^{th} OSIRIS stratospheric VCD measurement for a given three-day period
Φ_i	Longitude for the i^{th} OSIRIS stratospheric VCD measurement for a given three-day period
σ_{Θ}	Standard deviation in the Gaussian weighting for latitude
σ_{Φ}	Standard deviation in the Gaussian weighting for longitude
$w_i(\Theta, \Phi)$	Weight for the i^{th} OSIRIS stratospheric VCD measurement for a given three-day period at the grid point with latitude Θ and longitude Φ
$V_{\text{trop}}^{\text{OmO}}$	OMI-minus-OSIRIS tropospheric vertical column density
$V_{\text{trop}}^{\text{OMI}}$	OMI tropospheric vertical column density
$V_{\text{strat}}^{\text{OMI}}$	OMI stratospheric vertical column density
$V_{\text{strat}}^{\text{OSIRIS}}$	OSIRIS stratospheric vertical column density
$A_{\text{trop}}^{\text{OMI}}$	OMI tropospheric air mass factor
$A_{\text{strat}}^{\text{OMI}}$	OMI stratospheric air mass factor
$\sigma_{a,i}$	Standard deviation in element i of the <i>a priori</i> atmospheric state vector
r_c	Correlation length
\mathbf{x}_{true}	True atmospheric state vector; the atmospheric state used to simulate an instrument measurement

1 Introduction

The present thesis has two separate goals that are linked through the objective of attempting to improve the quality of surface-level pollutant concentrations retrieved from the measurements of optical instruments in operation onboard satellite platforms. The first goal is to investigate the difference in ozone retrieval error, for retrieved tropospheric ozone concentrations over Canada using simulated measurements from the Tropospheric Emissions: Monitoring of Pollution (TEMPO) instrument, associated with the implementation of a radiative transfer model with a more realistic geometry compared to using the one planned to be implemented by the National Aeronautics and Space Administration (NASA). The second goal is to further assess the feasibility of using the relatively novel method of combining limb- and nadir-viewing remote sensing satellite-borne instruments with non-coincident measurements to derive tropospheric nitrogen dioxide (NO_2) concentrations.

The intention of the first goal is to quantify potential benefits of implementing a radiative transfer model with a spherical geometry for all orders of scattering to retrieve ozone profiles over Canada with future TEMPO measurements compared to implementing the planned Vector Linearized Discrete Ordinates Radiative Transfer (VLIDORT) model, which assumes a plane-parallel Earth-atmosphere geometry for multiple-scattered electromagnetic radiation. This goal is addressed in the thesis by comparing, between the use of a radiative transfer model with a spherical geometry for all orders of scattering and the use of a radiative transfer model with a plane-parallel geometry for all orders of scattering, the error in retrieved tropospheric ozone concentrations over Canada using simulated TEMPO measurements. The second goal is addressed in this thesis by: i) reanalyzing the results of Adams et al. (2016) with newer datasets produced by the Optical Spectrograph and Infrared Imager System (OSIRIS), the Ozone Monitoring Instrument (OMI), and the photochemical box model of

Prather and Jaffe (1990), and ii) analyzing results for the non-coincident limb-nadir matching of OSIRIS and the European Space Agency (ESA) TROPOspheric Monitoring Instrument (TROPOMI), the successor of OMI.

The past century has seen a rapid increase in the rate of anthropogenic emissions of pollution due to rising industrialization and economic development. Consequently, frequent global measurements of the troposphere, which extends from the ground to an altitude between 6 and 20 km and is characterized by a temperature that increases with altitude, is important for the monitoring of air pollution. Ground-based measurement exist, but measurements from remote sensing instruments onboard satellites have the advantage of global coverage for each instrument and have been used since the 1960's, with the quantity of these instruments growing at an increasing rate. Most satellites for the purpose of atmospheric remote sensing are in polar orbits, providing near-global coverage with any given region being measured once daily. Some recent generations of atmospheric remote sensing satellites, however, are being put in geostationary orbits, which does not permit global coverage but allows for any given region to be measured at an hourly resolution. This provides finer analyses of the temporal variations of species in the lower atmosphere, which is particularly beneficial for pollutants that result largely from quickly varying anthropogenic emissions.

The TEMPO instrument of NASA, planned to be launched in 2022, is one such instrument designed to measure the atmosphere from a geostationary orbit. TEMPO will provide tropospheric pollution measurements over the majority of North America, from Mexico City to the Canadian Oil Sands and from the Pacific Ocean to the Atlantic Ocean. The ozone retrieval algorithm, which extracts tropospheric ozone concentrations from TEMPO measurements, is based on those of two heritage instruments, the Ozone Monitoring Instrument (OMI) and the Global Ozone Monitoring Experiment (GOME), and is planned to use the VLIDORT radiative transfer model to simulate the instrument measurements for different atmospheres. The VLIDORT model assumes a spherical Earth-atmosphere geometry for the single-scattered electromagnetic radiation of simulated measurements. To reduce the computational complexity, a simpler, less realistic plane-parallel Earth-atmosphere geometry is assumed in VLIDORT for the multiple-scattered electromagnetic radiation of simulated

measurements. This assumption for multiple-scattered electromagnetic radiation has an insignificant effect on the tropospheric ozone retrievals of the heritage instruments which have viewing zenith angles (VZAs) that are low, corresponding to the instrument pointing nearly straight down, and solar zenith angles (SZAs) that are low, corresponding to the Sun being high above the horizon. For most of the regions measured by TEMPO, the geometric assumption has a low impact on the tropospheric ozone retrievals. However, for measurements over Canada, and especially close to local sunrise or sunset, there is potential for the geometric assumption to significantly affect the accuracy of the derived ozone concentrations. This provides an opportunity for Canada to investigate the potential reductions in retrieval error due to the use of an algorithm with less geometric assumptions for Canadian air pollution monitoring.

Although species such as ozone and NO_2 pose threats to the health of life on Earth when in the troposphere, they do not pose an immediate threat when in the stratosphere, and in some cases are beneficial for living organisms. For example, stratospheric ozone shields the surface of the Earth from a significant portion of harmful ultraviolet (UV) radiation from outer space, whereas tropospheric ozone near the ground can cause severe respiratory problems. A major challenge in measuring the harmful tropospheric pollution with satellite-borne instruments is that species such as ozone and NO_2 exist primarily in the stratosphere, which extends from the top of the troposphere to an altitude around 50 km and is characterized by temperature that increases with altitude. Satellite-borne remote sensing instruments, typically at altitudes above 400 km, must look through the large stratospheric species concentrations to measure the tropospheric concentrations useful for air quality monitoring. They must therefore separate out the stratospheric part from the measurements.

The measurement of tropospheric ozone vertical number density profiles is possible by taking advantage of the optical properties of ozone. Its degree of electromagnetic radiation absorption varies substantially with wavelength, resulting in sunlight of different wavelengths penetrating the atmosphere over a large range of altitudes. This in turn enables the measurement of ozone concentrations at different altitudes by measuring a range of wavelengths of electromagnetic radiation. NO_2 , on the other hand, has a degree of electromagnetic radiation

absorption that does not vary as much with wavelength, making it difficult to use this method. The measurement of tropospheric NO₂ therefore typically makes use of additional assumptions, such as low longitudinal concentration variations, global chemical transport models, cloud data to make measurements over cloudy regions, and calibrations using measurements over regions with low tropospheric pollution levels such as the Pacific Ocean.

A relatively novel troposphere-stratosphere separation method (Adams et al., 2016) demonstrates the feasibility of estimating the tropospheric NO₂ column density by taking the stratospheric column density measured by a limb-viewing remote sensing instrument and subtracting it from the combined troposphere-stratosphere column density measured by a nadir-viewing instrument, with the two instruments having non-coincident measurements. The limb- and nadir-viewing instrument measurements are matched in local time and position by taking advantage of the lower variations of NO₂ in the stratosphere and the daily global coverage of the two instruments. A photochemical box model, which models the photochemical diurnal variations in the concentrations of atmospheric species such as NO₂, is used to extrapolate the limb-measurement-derived stratospheric NO₂ concentrations in local solar time to match the local times of the nadir-viewing instrument measurements. The stratospheric NO₂ concentrations measured by the limb-viewing instrument over a period of time are interpolated and smoothed to match the geographic locations of the nadir-viewing instrument measurements. An assessment of this method with different datasets and instruments would provide further understanding of the value in using the method.

Chapter 2 comprises relevant background information, including atmospheric remote sensing fundamentals, details of the SASKTRAN radiative transfer model and the Optimal Estimation algorithm used for the TEMPO ozone retrievals, and a description of the non-coincident limb-nadir matching algorithm. Chapter 3 details the development and validation of both the heritage-instrument-based and the simulated-TEMPO-based ozone retrieval algorithms. Chapter 4 consists of comparisons between OSIRIS NO₂ profile data that lead to the development of an updated OSIRIS NO₂ profile retrieval algorithm, the reanalysis of tropospheric NO₂ density columns resulting from OSIRIS-OMI limb-nadir matching, and the analysis of tropospheric NO₂ density columns resulting from OSIRIS-TROPOMI limb-nadir matching.

Chapter 5 concludes the results of this thesis and outlines the recommendations for future work.

2 Background

2.1 Atmospheric Remote Sensing

A common method to determine the atmospheric concentration of a given species is to use satellite optical spectrometer measurements and a radiative transfer model (see Section 2.2). Remotely measuring the atmosphere with a satellite instrument has the advantage of providing long-term records with near-global coverage. The radiative transfer model is used to simulate measurements of the satellite instrument in a realistic, simulated atmosphere to determine the most plausible atmospheric state given the instrument measurements and any other *a priori* information. The radiative transfer model therefore requires models of the optical spectrometer and of the atmosphere. The process of determining atmospheric species concentrations with this method is often referred to as a retrieval algorithm. The retrieval algorithm typically involves iteratively varying parameters, such as the concentration of individual atmospheric species, in the radiative transfer model until some predefined set of constraints is satisfied. As a crude example, the concentration of ozone in the radiative transfer model could be varied until the radiance measurement simulated by the model best matches the instrument radiance measurement. The data at each step of the algorithm is often referred to by a processing level. For example, the instrument measurement data is level 1 and the retrieved species concentrations are level 2.

2.1.1 Atmosphere

The atmospheric vertical column above any point on the surface of the Earth is organized into layers separated by altitudes for which the lapse rate, defined as the negative derivative of temperature with respect to altitude, is zero. The altitudes separating the different atmo-

spheric layers vary with the time of year and with the latitude and longitude of the surface of the Earth at the bottom of the atmospheric column (Wallace & Hobbs, 2006). The two lowest layers, the troposphere and the stratosphere, contain the largest concentrations of species and are relevant to the present work. The troposphere, extending from the ground to the tropopause at an altitude between 6 and 20 km, is heated primarily by the Earth, resulting in the temperature decreasing with altitude. The tropopause altitude is dependent on factors such as latitude and time of the year. The stratosphere, extending from the tropopause to the stratopause at an altitude near 50 km (Wallace & Hobbs, 2006), is heated primarily by the absorption of UV radiation from the Sun, resulting in the temperature increasing with altitude.

2.1.2 Instrument Geometries

Atmospheric remote sensing satellites are principally in low-Earth orbit (LEO) at altitudes between 400 and 800 km (Riebeek, 2009). Remote sensing satellites in LEO are often in a Sun-synchronous orbit, meaning they measure over regions at a local time that is approximately constant for each half of the orbit. Some recent remote sensing satellites are being put into geostationary orbits, meaning their orbital period matches the period of rotation of the Earth. Satellites at geostationary orbit are at an altitude of approximately 35 786 km directly above the equator. The advantage of remote sensing from a geostationary orbit is an increased frequency of measurements over any region in the field of regard, where the field of regard is defined as the union of all possible instantaneous fields of view of the instrument. The plane containing the orbital path of a satellite is referred to as the orbital plane. The ground track of a satellite is defined as the track on the surface of the Earth that is directly below the instrument as it passes over.

Two types of satellite instrument viewing geometries relevant to the present work are the nadir and limb geometries. The nadir-viewing geometry for a LEO and for a geostationary orbit, and the limb-viewing geometry for a LEO, are illustrated in Fig. 2.1. The nadir-viewing geometry is where the instrument is pointed towards the surface of the Earth, and allows for column densities reaching down to the ground to be measured at relatively high longitudinal

and latitudinal resolutions. The limb-viewing geometry is where the instrument is pointed across the limb of the atmosphere, and allows stratospheric and upper tropospheric vertical density profiles to be measured at relatively high altitude resolutions.

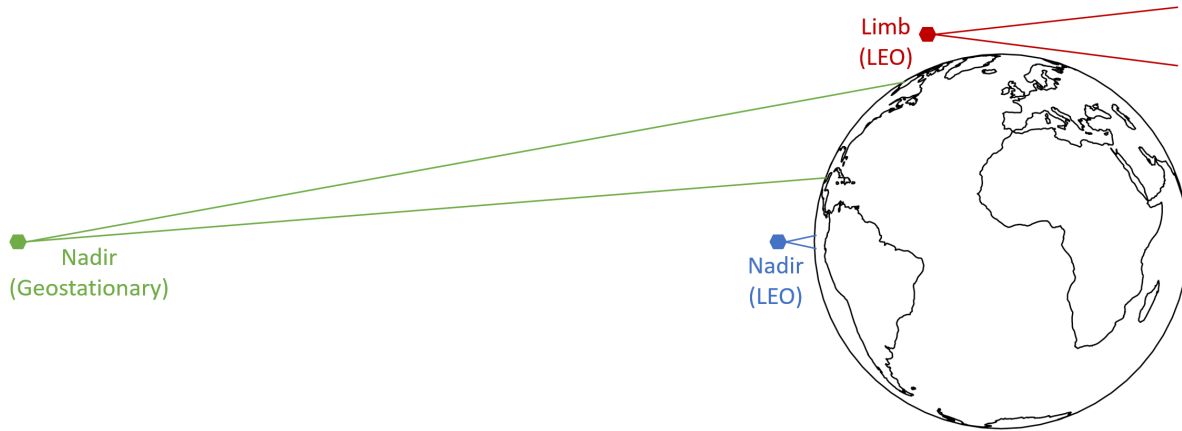


Figure 2.1. Common remote sensing instrument viewing geometries for low-Earth orbits (LEOs) and geostationary orbits. The lines in each case show the edges of the range of viewing angles. The orbit altitudes and viewing angles are exaggerated for illustrative purposes.

When a nadir-viewing instrument measures the electromagnetic radiation that originates from the Sun and is scattered and reflected along various paths through the atmosphere before reaching the instrument sensor, the column density along the effective path of electromagnetic radiation is called the slant column density (SCD). The more useful vertical column density (VCD) is the column density along a straight path of electromagnetic radiation that is perpendicular to the surface of the Earth directly below it. This path need not reach all the way down to the surface of the Earth or up to the top of the atmosphere. For example, a stratospheric VCD extends from the tropopause to the stratopause. An SCD is converted to a VCD using an air mass factor (AMF) which is defined by the ratio $AMF = SCD / VCD$, and is pre-calculated for various scenarios using radiative transfer modeling (see Section 2.2). The AMFs are dependent on factors such as the instrument viewing geometry, the relative orientation of the Sun, the vertical density profile of the species to be measured, the albedo at different points on the surface of the Earth, and the amount of clouds and aerosols (Platt

& Stutz, 2008).

Fig. 2.2 illustrates the primary parameters for nadir- and limb-viewing geometries. Note that due to the size of the Sun, the lines of solar radiation propagation can be assumed to be parallel to each other anywhere they reach the atmosphere of the Earth. The VZA of a nadir-viewing instrument is defined as the angle between the instrument line of sight (LOS) and the local zenith at the LOS-ground intersection. For example, a VZA of 0° corresponds to the instrument pointing straight down towards the Earth and a VZA of 90° corresponds to the instrument looking at the horizon, that is, with the LOS intersecting the Earth parallel to the surface. In three dimensions, the VZA and the LOS-ground intersection point restrict the possible LOSs to a cone, with the tip of the cone at the LOS-ground intersection. The viewing azimuth angle (VAA) (not shown in Fig. 2.2) further restricts the LOS to a single value. A common convention for the VAA is for 0° to correspond to the instrument looking from local north, with the VAA increasing as the LOS is rotated counter-clockwise about the local zenith when viewed from above. For example, a SAA of 90° would correspond to the instrument looking from local west.

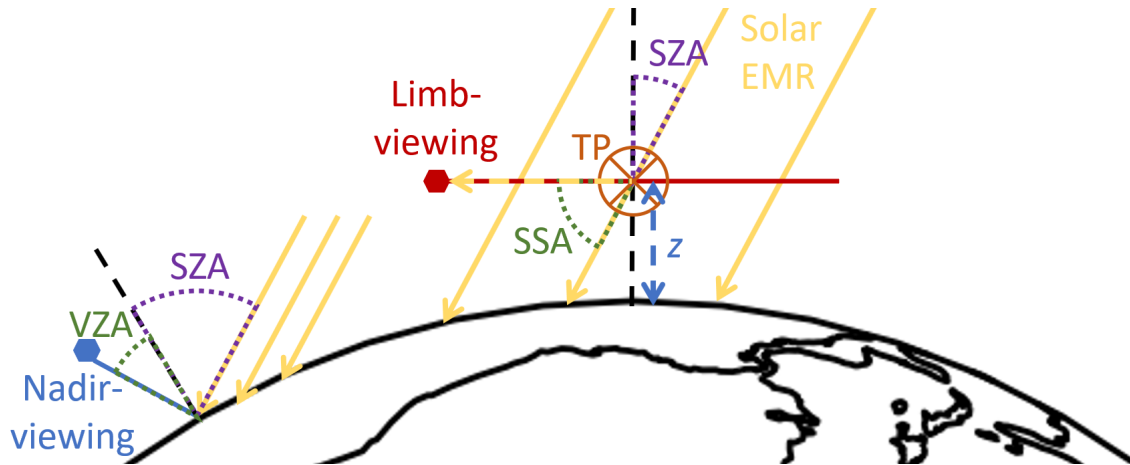


Figure 2.2. Instrument viewing geometry parameters: viewing zenith angle (VZA), solar zenith angle (SZA), solar scattering angle (SSA), tangent point (TP), and tangent point altitude (z) for nadir- and limb-viewing instrument geometries.

The SZA of a nadir-viewing instrument measurement is defined as the angle between the local zenith at the LOS-ground intersection and the line of solar radiation propagation that

intersects the LOS-ground intersection. For example, a SZA of 0° corresponds to the Sun being directly overhead the LOS-ground intersection and a SZA of 90° corresponds to the Sun being at the horizon when viewed from the LOS-ground intersection. Similar to the VAA, the solar azimuth angle (SAA) (not shown in Fig. 2.2) restricts the direction of the Sun in three dimensions to a single value, typically with a SAA of 0° corresponding to a Sun direction towards local north, a SAA of 90° corresponding to a Sun direction towards local west, and so on.

For the limb-viewing geometry, the tangent point is defined as the point along the instrument LOS where the LOS is parallel to the surface of the Earth directly below. The latitude and longitude of the point on the Earth directly below the tangent point are called the tangent-point latitude and longitude, respectively. The distance from the surface of the Earth to the tangent point is called the tangent-point altitude. The SZA of a limb-viewing instrument measurement is defined as the angle between the local zenith at the tangent point and the line of solar radiation propagation that intersects the tangent point. Similar to a nadir-viewing instrument, the SAA is normally defined such that 0° corresponds to a Sun direction towards local north, 90° corresponds to a Sun direction towards local west, and so on. The solar scattering angle (SSA) is defined as the angle between the instrument LOS and the lines of input solar radiation propagation that intersect the LOS.

2.1.3 Instrument Sensors

Three parameters of optical spectrometers relevant to the discussion herein are the spectral resolution, the spectral sampling rate, and the spectral point spread function. The spectral resolution and sampling rate describe the ability of the instrument to differentiate between different wavelengths of electromagnetic radiation. The spectral resolution is typically defined in terms of the full-width half-maximum of the sensitivity peak for a given wavelength pixel of the sensor, while the spectral sampling rate is defined by the distance between sensitivity peaks of consecutive wavelength pixels. The spectral point spread function describes the impulse response of the imaging system, that is, its response to a point source.

2.2 Radiative Transfer

Radiative transfer is the study of how energy is transferred through a medium in the form of electromagnetic radiation, which is quantized as photons. For the remainder of the discussion herein, the term “light” is taken as synonymous to “electromagnetic radiation” and therefore does not specifically refer to visible light. In the field of atmosphere science, radiative transfer involves taking into account the scattering, absorption, and emission of light off atmospheric species, as well as the reflection of light off the ground. Various software packages (e.g., Bourassa et al., 2008; Spurr, 2006; Spurr et al., 2001) have been developed to numerically approximate the transfer of light from the Sun, through the atmosphere, and into different types of optical instruments.

2.2.1 Radiometric Quantities

A useful quantity for radiative transfer with the application of remote sensing is spectral radiance. Consider Fig. 2.3, which depicts the geometry for light of wavelength λ at the point \mathbf{r} , propagating within a solid angle $d\Omega$ of the direction $\hat{\Omega}$ through an area dA , with the propagation direction, $\hat{\Omega}$, being an angle θ from the normal, \hat{n} , of the area dA . The spectral radiance is defined as the amount of energy, dE , per wavelength range $d\lambda$, time interval dt , solid angle range $d\Omega$, and projected area $\cos\theta dA$, at wavelength λ , transferred from the point \mathbf{r} in the direction $\hat{\Omega}$. This is given by

$$I(\mathbf{r}, \hat{\Omega}, \lambda) = \frac{dE(\mathbf{r}, \hat{\Omega}, \lambda)}{d\lambda \cos\theta dA d\Omega dt}, \quad (2.1)$$

where the projected area, $\cos\theta dA$, is the area dA projected onto the propagation direction $\hat{\Omega}$. Although the units for spectral radiance are $\text{W sr}^{-1} \text{m}^{-3}$ based on the International System of Units (SI), it is convenient for the application of remote sensing instruments to express the spectral radiance in terms of photons $\text{s}^{-1} \text{sr}^{-1} \text{cm}^{-2} \text{nm}^{-1}$, which can be easily understood from the definition in Eq. (2.1). The term “spectral radiance” is often shortened in literature to “radiance”, with the wavelength dependence being implicit.

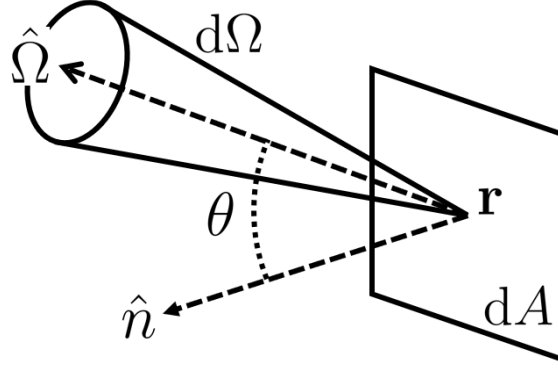


Figure 2.3. Geometry for defining radiance.

Because the spectral radiance of light is constant as it travels through a vacuum, any change in spectral radiance as the light travels through a medium gives information about the species in the medium. Thus, if light is travelling through a medium, and the input spectral radiance (e.g., from solar radiation) and output spectral radiance (e.g., measured by the instrument) are known, then the change between the two and knowledge of the optical properties of the species present in the medium can be used to determine the relative proportions of the species.

A related term to spectral radiance is the spectral flux density or spectral irradiance, which can be defined as the integral of the spectral radiance projected onto the normal, \hat{n} , of surface dA , with the integral being over all solid angles of the hemisphere on one side of area dA . It is given by

$$F(\mathbf{r}, \hat{n}, \lambda) = \int_{2\pi} I(\mathbf{r}, \hat{\Omega}', \lambda) \cos(\theta') d\Omega' = \frac{dE}{d\lambda dA dt}, \quad (2.2)$$

where θ' is the angle between the direction $\hat{\Omega}'$ and the normal, \hat{n} , of the surface dA .

For convenience in the remainder of the discussion herein, the dependence of spectral radiance and flux density on \mathbf{r} , $\hat{\Omega}$, and λ are considered implicit if the arguments are omitted.

2.2.2 Scattering and Absorption

The scattering of light is the process by which photons interact with other particles resulting in a change in trajectory of the photons. As photons propagate in a straight line in a vacuum,

their trajectory can only change through scattering or absorption and re-emission. Scattering is elastic if the photon energy is conserved or inelastic if there is a transfer of energy between the photon and the particle on which it is incident.

The absorption of light is the process where a photon transfers its energy to a particle on which the photon is incident. The energy transferred results in a change of the quantum mechanical state of the target particle. For example, ozone (O_3) in the stratosphere is dissociated into O_2 and O after absorbing UV radiation. This has the effect of shielding the Earth from a large portion of harmful solar UV radiation.

Fraunhofer absorption lines are lines in the solar spectrum where light is absorbed by the different chemicals in the photosphere of the Sun. The Ring effect, discovered by Grainger and Ring (1962), is the phenomenon where the relative depths of the Fraunhofer absorption lines are greater in direct sunlight than in light that has been scattered by the atmosphere of the Earth (Vountas et al., 1998). The Ring Effect is not entirely understood, but it is believed to be primarily due to rotational Raman scattering, which is inelastic scattering where the shift in frequency is related to the rotational properties of O_2 and N_2 molecules (Chance & Spurr, 1997; Joiner & Vasilkov, 2006).

2.2.3 Reflection

A Lambertian surface is a surface where the radiance is reflected or emitted from the surface isotropically. In this case, the spectral flux density reflected at \mathbf{r} , $F_r(\mathbf{r}, \hat{n})$, is defined using Eq. (2.2) in terms of the isotropically reflected radiance, $I_r(\mathbf{r})$, at the point \mathbf{r} as

$$\begin{aligned}
 F_r(\mathbf{r}, \hat{n}) &= \int_{2\pi} I_r(\mathbf{r}) \cos(\theta') d\Omega' \\
 &= I_r(\mathbf{r}) \int_0^{2\pi} \int_0^{\pi/2} \cos(\theta') \sin(\theta') d\theta' d\phi' \\
 &= \pi I_r(\mathbf{r}).
 \end{aligned} \tag{2.3}$$

The albedo of a surface is a value between 0 and 1 that defines how well a surface can reflect spectral flux density. It is given by

$$a(\mathbf{r}) = \frac{F_r(\mathbf{r}, \hat{n})}{F_i(\mathbf{r}, -\hat{n})}, \tag{2.4}$$

where $F_i(\mathbf{r}, -\hat{n})$ is the incident spectral flux density at \mathbf{r} . Combining Eqs. (2.3) and (2.4), the radiance reflected off a Lambertian surface in the direction $\hat{\Omega}$ can be expressed as

$$I_r(\mathbf{r}, \hat{\Omega}) = \frac{a(\mathbf{r})}{\pi} F_i(\mathbf{r}, -\hat{n}). \quad (2.5)$$

2.2.4 Beer-Lambert Law

Consider light travelling in a direction defined by the unit vector $\hat{\Omega}$ from a point \mathbf{r} to a reference point \mathbf{r}_0 , with the vectors defined in Cartesian coordinates. The position along the path of light is often parametrized in terms of the path coordinate s for a given reference point \mathbf{r}_0 and propagation direction $\hat{\Omega}$. This is given by the equation

$$\mathbf{r}(s; \mathbf{r}_0, \hat{\Omega}) = \mathbf{r}_0 + \hat{\Omega}s. \quad (2.6)$$

The reference point \mathbf{r}_0 is often chosen to be at the position of the observer. In this formulation, the observer measures light coming from the negative s direction. For convenience in the remainder of the discussion herein, the position $\mathbf{r}(s; \mathbf{r}_0, \hat{\Omega})$ is abbreviated as $\mathbf{r}(s)$, with implicit dependencies on reference point \mathbf{r}_0 and propagation direction $\hat{\Omega}$. Furthermore, any quantity with argument s is implicitly dependent on position $\mathbf{r}(s) \equiv \mathbf{r}(s; \mathbf{r}_0, \hat{\Omega})$ as per Eq. (2.6). For example, the radiance at point \mathbf{r} is denoted by $I(s) \equiv I(\mathbf{r}(s)) \equiv I(\mathbf{r}(s; \mathbf{r}_0, \hat{\Omega}))$.

Consider radiance I travelling in the direction $\hat{\Omega}$, with wavelength λ , incident on a volume V of N particles, each with an effective area α . Assume that the particles are sufficiently spread out such that when viewed from any direction, none of the effective areas of the N particles overlap with each other. After travelling a distance of ds , the decrease in radiance is

$$dI = -I \frac{N}{V} \alpha ds. \quad (2.7)$$

The so-called effective area α of the particles is analogous to a quantity called their cross section, which is directly related to the probability of a photon interacting with the particles and is in units of m^2 . The cross section is dependent on the type of particles and on the wavelength of incident photons. The scattering cross section and absorption cross section are cross sections corresponding specifically to the interaction between the photons and the particles due to scattering or absorption, respectively.

Consider the same scenario but with the existence of different types of particles or species, with species i having scattering cross section $\sigma_{\text{scatt},i}(\lambda)$, absorption cross section $\sigma_{\text{abs},i}(\lambda)$, and number density $n_i(\mathbf{r})$ at position \mathbf{r} . The scattering and absorption extinctions are defined by adding up the effects of all the species together. This is given by

$$\begin{aligned} k_{\text{scatt}}(s, \lambda) &= \sum_i n_i(s) \sigma_{\text{scatt},i}(\lambda) \text{ and} \\ k_{\text{abs}}(s, \lambda) &= \sum_i n_i(s) \sigma_{\text{abs},i}(\lambda), \end{aligned} \tag{2.8}$$

where k_{scatt} and k_{abs} are the scattering and absorption extinctions, respectively. The total extinction is the sum of scattering and absorption extinctions: $k = k_{\text{scatt}} + k_{\text{abs}}$.

Based on Eq. (2.7), the decrease in radiance over an infinitesimal distance ds at position \mathbf{r} with various species and particles can be expressed as

$$dI(s) = -I(s)k(s) ds, \tag{2.9}$$

where $k(s)$ and $I(s)$ are implicitly dependent on wavelength λ .

The optical depth is a non-negative, unitless quantity that describes the amount of attenuation of light along a path. The optical depth for light travelling from point $\mathbf{r}(s_0)$ to point $\mathbf{r}(s_1)$, with $s_0 \leq s_1$, is given by

$$\tau(s_0, s_1, \hat{\Omega}) = \int_{s_0}^{s_1} k(\mathbf{r}_0 + s\hat{\Omega}) ds. \tag{2.10}$$

Integrating Eq. (2.9) from point $\mathbf{r}(s_0)$ to point $\mathbf{r}(s_1)$ and substituting Eq. (2.10) results in the Beer-Lambert Law,

$$I(s_1) = I(s_0)e^{-\tau(s_0, s_1, \hat{\Omega})}, \tag{2.11}$$

which describes the attenuation of radiance through a medium.

2.2.5 Radiative Transfer Equation

To account for light sources along the path, Eq. (2.9) is re-expressed as

$$\frac{dI(s)}{ds} = -I(s)k(s) + J(s), \tag{2.12}$$

where $J(s)$ is the source term or volume emission rate, in units of photons $\text{s}^{-1} \text{sr}^{-1} \text{cm}^{-3} \text{nm}^{-1}$, and is implicitly dependent on $\hat{\Omega}$ and λ . Light sources include elastic scattering, inelastic scattering, and thermal emissions. The following discussion only considers the elastic scattering as it is the dominant source contribution for UV, visible, and infrared light, which are relevant to the discussion herein. In this case, the volume emission rate at $\mathbf{r}(s)$ towards $\hat{\Omega}$ is defined as

$$J(s, \hat{\Omega}) = k_{\text{scatt}}(s) \int_{4\pi} I(s, \hat{\Omega}') \bar{p}(s, \hat{\Omega}', \hat{\Omega}) d\hat{\Omega}', \quad (2.13)$$

where the integral is over all solid angles and $\bar{p}(s, \hat{\Omega}', \hat{\Omega})$ is the effective phase function. The effective phase function is calculated as a weighted sum of phase functions for all species, where each phase function is the probability of the photons being scattered by the species at $\mathbf{r}(s)$, from direction $\hat{\Omega}'$ to $\hat{\Omega}$, per unit solid angle.

Let the optical depth from point $\mathbf{r}(s)$ to the reference point be denoted by $\tau_s \equiv \tau(s, 0, \hat{\Omega})$. From Eq. (2.10), the differential form of the relationship between τ_s and s is given by

$$d\tau_s = -k(s) ds. \quad (2.14)$$

The negative sign makes sense as an increase in s results in a decrease in the path length, $\Delta s = 0 - s$, and therefore a decrease in the optical depth. Transforming Eq. (2.12) from the path coordinate s to the optical depth τ_s using Eq. (2.14) results in

$$\frac{dI(\tau_s)}{d\tau_s} = I(\tau_s) - \frac{J(\tau_s)}{k(\tau_s)}. \quad (2.15)$$

Substituting this into the identity

$$\frac{d}{d\tau_s} [I(\tau_s) e^{-\tau_s}] = \left[\frac{dI(\tau_s)}{d\tau_s} - I(\tau_s) \right] e^{-\tau_s}, \quad (2.16)$$

and integrating from $\tau_s = \tau_{s'}$ to $\tau_s = \tau_0 = 0$ gives

$$I(0) - I(\tau_{s'}) e^{-\tau_{s'}} = - \int_{\tau_{s'}}^0 \frac{J(\tau_s)}{k(\tau_s)} e^{-\tau_s} d\tau_s. \quad (2.17)$$

Transforming back to the path coordinate s using Eq. (2.14) results in

$$I(0) = \int_{s'}^0 J(s) e^{-\tau(s, 0, \hat{\Omega})} ds + I(s') e^{-\tau(s', 0, \hat{\Omega})}. \quad (2.18)$$

2.2.6 Successive Orders of Scattering

Consider an instrument at the reference point, \mathbf{r}_0 , looking in direction $-\hat{\Omega}$, with the LOS ending at $\mathbf{r}(s_{\text{end}})$. If the instrument is looking towards the Earth, then $\mathbf{r}(s_{\text{end}})$ is the point where the LOS intersects the surface of the Earth. If the instrument is looking through the limb of the atmosphere, then $\mathbf{r}(s_{\text{end}})$ is the point where the LOS intersects the effective top of the atmosphere (ETA), where the ETA is the highest altitude defined in the radiative transfer model. It is assumed that number densities are sufficiently small above the ETA such that the spectral flux density anywhere above the ETA is effectively equal to the solar spectral flux density, $F_{\text{sun}}(\hat{\Omega}_{\text{sun}})$, in the direction of the solar radiation, $\hat{\Omega}_{\text{sun}}$. For this reason, the radiance at the end of the LOS going in direction $\hat{\Omega}$ is denoted by $I^{\text{end}}(\hat{\Omega})$. If the LOS intersects the ETA, $I^{\text{end}}(\hat{\Omega})$ is 0. If the LOS intersects the surface of the Earth, $I^{\text{end}}(\hat{\Omega})$ is defined in terms of the reflection of attenuated solar spectral flux density off the surface of the Earth into the direction $\hat{\Omega}$.

Eq. (2.18) can be solved with the successive orders of scattering method (Hansen & Travis, 1974; van de Hulst, 1948), which involves separating the equation into each order of scattering such that I_i is the radiance that has been scattered i times and J_i is the volume emission rate resulting from I_i . In this formulation, each order of scattering is dependent on the previous order. The base case is the zero-scatter term, or the direct solar radiation term, which is restricted to the direction of the solar radiation, $\hat{\Omega}_{\text{sun}}$. The zero-scatter term is defined as

$$I_0(s, \hat{\Omega}) = F_{\text{sun}}(\hat{\Omega}_{\text{sun}}) e^{-\tau_{\text{sun}}(s)} \delta(\hat{\Omega} - \hat{\Omega}_{\text{sun}}), \quad (2.19)$$

where $\tau_{\text{sun}}(s) \equiv \tau(s_{\text{sun}}, s, \hat{\Omega}_{\text{sun}})$ is the optical depth from the Sun (point $\mathbf{r}(s_{\text{sun}})$) to the point $\mathbf{r}(s)$, $\hat{\Omega}_{\text{sun}}$ is the direction of the solar radiation, $F_{\text{sun}}(\hat{\Omega}_{\text{sun}})$ is the spectral flux density going in direction $\hat{\Omega}_{\text{sun}}$ from the Sun, and $\delta(\hat{\Omega})$ is a three-dimensional delta function. The delta function is defined such that

$$\int_{\Omega} f(\hat{\Omega}') \delta(\hat{\Omega}' - \hat{\Omega}_0) d\Omega' = \begin{cases} f(\hat{\Omega}_0) & \hat{\Omega}_0 \in \Omega \\ 0 & \hat{\Omega}_0 \notin \Omega \end{cases}, \quad (2.20)$$

where the integral is over a solid angle space Ω and $f(\hat{\Omega})$ is an arbitrary function of $\hat{\Omega}$. In

practice, $\tau_{\text{sun}}(s)$ in Eq. (2.19) is calculated as the optical depth from the ETA to the point $\mathbf{r}(s)$ in the direction $\hat{\Omega}_{\text{sun}}$.

For a LOS going from the observer at point \mathbf{r}_0 in the direction $-\hat{\Omega}$ to the point $\mathbf{r}(s_{\text{end}})$, the radiance at \mathbf{r}_0 coming from the direction $-\hat{\Omega}$ for orders of scattering $i \geq 1$ is given by

$$I_i(\mathbf{r}_0, \hat{\Omega}) = \int_{s_{\text{end}}}^0 J_i(s, \hat{\Omega}) e^{-\tau(s, 0, \hat{\Omega})} ds + I_i^{\text{end}}(\hat{\Omega}) e^{-\tau(s_{\text{end}}, 0, \hat{\Omega})}, \quad (2.21a)$$

$$J_i(s, \hat{\Omega}) = \int_{4\pi} I_{i-1}(s, \hat{\Omega}') \bar{p}(s, \hat{\Omega}', \hat{\Omega}) d\Omega', \quad (2.21b)$$

$$I_i^{\text{end}}(\hat{\Omega}) = \begin{cases} \frac{a}{\pi} \int_{2\pi} I_{i-1}(s_{\text{end}}, \hat{\Omega}') \cos \theta' d\Omega' & \text{LOS intersects Earth surface} \\ 0 & \text{LOS intersects ETA} \end{cases}, \quad (2.21c)$$

where θ' is the angle between $\hat{\Omega}'$ and the local normal of the surface of the Earth at the point $\mathbf{r}(s_{\text{end}})$.

For example, in the case that the LOS intersects the surface of the Earth, the single-scattered flux density at $\mathbf{r}(s)$ and the single-scattered spectral radiance at $\mathbf{r}(s_{\text{end}})$ can be calculated using Eqs. (2.19), (2.21b) and (2.21c) as

$$\begin{aligned} J_1(s, \hat{\Omega}) &= F_{\text{sun}}(\hat{\Omega}_{\text{sun}}) e^{-\tau_{\text{sun}}(s)} \bar{p}(s, \hat{\Omega}_{\text{sun}}, \hat{\Omega}) \text{ and} \\ I_1^{\text{end}}(\hat{\Omega}) &= \frac{a}{\pi} F_{\text{sun}}(\hat{\Omega}_{\text{sun}}) e^{-\tau_{\text{sun}}(s_{\text{end}})} \cos(\theta_{\text{sza}}), \end{aligned} \quad (2.22)$$

where θ_{sza} is the local solar zenith angle at the point $\mathbf{r}(s_{\text{end}})$, i.e., the angle between $-\hat{\Omega}_{\text{sun}}$ and the normal of the surface of the Earth at point $\mathbf{r}(s_{\text{end}})$. The zero-scatter term in Eq. (2.19) is not calculated in practice. Instead, the single-scatter terms in Eq. (2.22) are calculated first, followed by the resultant single-scatter radiance term using Eq. (2.21a). The higher-order-scatter terms are then iteratively calculated using Eq. (2.21).

2.2.7 SASKTRAN

SASKTRAN (Bourassa et al., 2008) is a radiative transfer modelling package developed and maintained by the Atmospheric Research Group of the University of Saskatchewan. The three SASKTRAN engines relevant to the present work are the discrete ordinates (DO), high resolution (HR), and high resolution single-scatter approximation (HRSSApprox) engines.

The DO and HR engines are on opposite extremes; the DO engine uses a purely plane-parallel Earth-atmosphere geometry while the HR engine uses a purely spherical Earth-atmosphere geometry (Zawada et al., 2015). Compared to the DO engine, the HR engine compromises computational speed for accuracy. The HRSSApprox engine is the same as the HR engine except that, after calculating the single-scatter contribution to a measurement for all user-defined wavelengths, the multiple-scatter contributions are calculated exactly only for a subset of the wavelengths. The multiple-scatter contribution for the remaining wavelengths are calculated by interpolating the results of the subset of wavelengths. This greatly reduces the computational complexity, and therefore the computation time, without significantly reducing the accuracy of the results as the multiple-scattered light has a significantly smaller contribution to the total light measured by an observer.

2.2.8 Example Simulated Radiances

The effects of the viewing geometry and the SASKTRAN engine on the simulated Sun-normalized radiances are shown in Sections 2.2.8.1 and 2.2.8.2, respectively. The Sun-normalized radiances are defined by dividing the simulated measured radiances by solar radiances, effectively cancelling any features that result purely from the Sun. For all the following examples in Sections 2.2.8.1 and 2.2.8.2, the surface albedo is set to 0.5, the ETA is defined as 80 km, the MSIS-90 model (Hedin, 1991) is used for the pressure, temperature, and number density of the air, the NO₂ vertical density profiles are taken from a climatological dataset by Prather and Jaffe (1990), the ozone vertical density profiles are taken from a climatological dataset by McPeters et al. (1997), and the ozone and NO₂ cross sections used in the radiative transfer model are taken from experimentally determined values (Brion et al., 1998; Brion et al., 1993; Daumont et al., 1992; Malicet et al., 1995; Vandaele et al., 1998).

2.2.8.1 Limb versus Nadir

Fig. 2.4 shows some sample Sun-normalized radiances simulated with the SASKTRAN HR engine for limb- and nadir-viewing geometries. Note that the solar-viewing azimuth angle difference is the difference between the SAA and the VAA. Radiances are shown for a set of

SZAs, with a solar-viewing azimuth angle difference of 0° in Fig. 2.4(a) and 90° in Fig. 2.4(b). The shape of the simulated radiances can be explained by the absorption cross section of ozone, the dominant absorber in the region being observed. A typical ozone absorption cross section is shown in Fig. 2.5. For both viewing geometries, the shape of the measured radiance curves can be seen to mirror the shape of the ozone cross section. This makes sense as a higher absorption cross section results in more photons being absorbed by ozone and therefore less radiance reaching the measuring instrument. For any given viewing and solar geometry, the amount of absorption indicates the amount of ozone. Thus, these absorption features allow for the ozone concentrations to be determined from the instrument measurements.

The simulated measured radiances for both viewing geometries are similar to each other from 300 to 350 nm. However, there is significantly more measured radiance at longer wavelengths for the nadir-viewing geometry due to the increased effect of reflection for the nadir geometry and the lower optical depths of the longer wavelengths. The lower optical depths of the longer wavelengths allows a larger proportion of the photons to reach the ground and reflect up towards the nadir-viewing instrument. Due to the larger influence of reflection on the nadir-viewing measurements, there is more measured radiance for the nadir geometry as the SZA is decreased, that is, as the Sun gets higher.

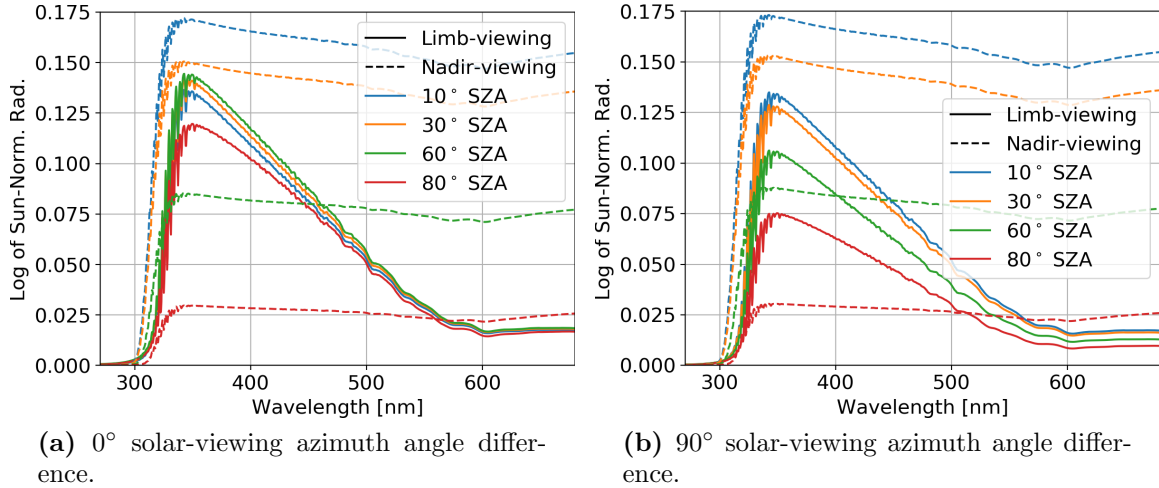


Figure 2.4. Effect of the instrument viewing geometry on the Sun-normalized measured radiances simulated in the SASKTRAN HR engine for wavelengths relevant to the remote sensing instruments discussed herein, for an instrument at an altitude of 650 km, and for a set of solar zenith angles (SZAs). For the nadir geometry, the instrument is pointed towards 44°N - 150°W with a viewing zenith angle of approximately 1° . For the limb geometry, the tangent-point is 20 km above 44°N - 150°W .

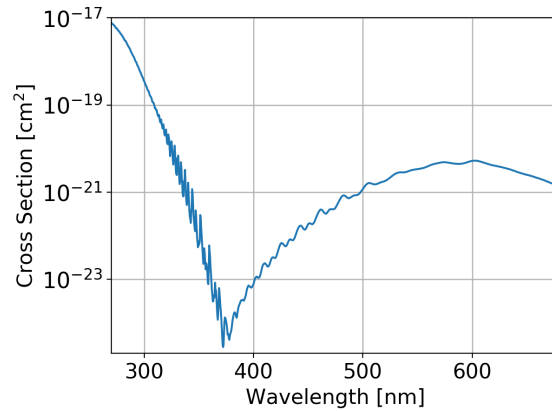


Figure 2.5. Typical ozone absorption cross sections over wavelengths relevant to the remote sensing instruments discussed herein. Cross sections are taken from experimentally determined data (Brion et al., 1998; Brion et al., 1993; Daumont et al., 1992; Malicet et al., 1995) for the temperature at an altitude of 20 km above 0°N - 0°E on 21 March 2008 in the MSIS-90 model (Hedin, 1991).

2.2.8.2 Engine Comparison

Fig. 2.6 shows the effect of the SASKTRAN engine (DO versus HR) on the simulated Sun-normalized radiances for an instrument in geostationary orbit above 0°N - 100°W , pointing towards the Canadian Oil Sands (57°N - 112°), one hour past local sunrise for four different days of the year 2022. Similar to Fig. 2.4, the Sun-normalized radiances of Fig. 2.6 generally mirror the ozone cross section (Fig. 2.5) due to the large relative effect of the ozone absorption. Fig. 2.6 shows that for high VZAs and SZAs, the DO engine tends to underestimate the measured radiances relative to the HR engine. This effect is much smaller for the UV wavelengths below 320 nm, largely due to the significant ozone absorption, and therefore the lower amount of radiance reaching the instrument, in this wavelength range. One of the goals of the present work is to determine if, for cases of high VZAs, differences in the radiative transfer engine of the retrieval algorithm result in significant differences in the retrieval of tropospheric ozone.

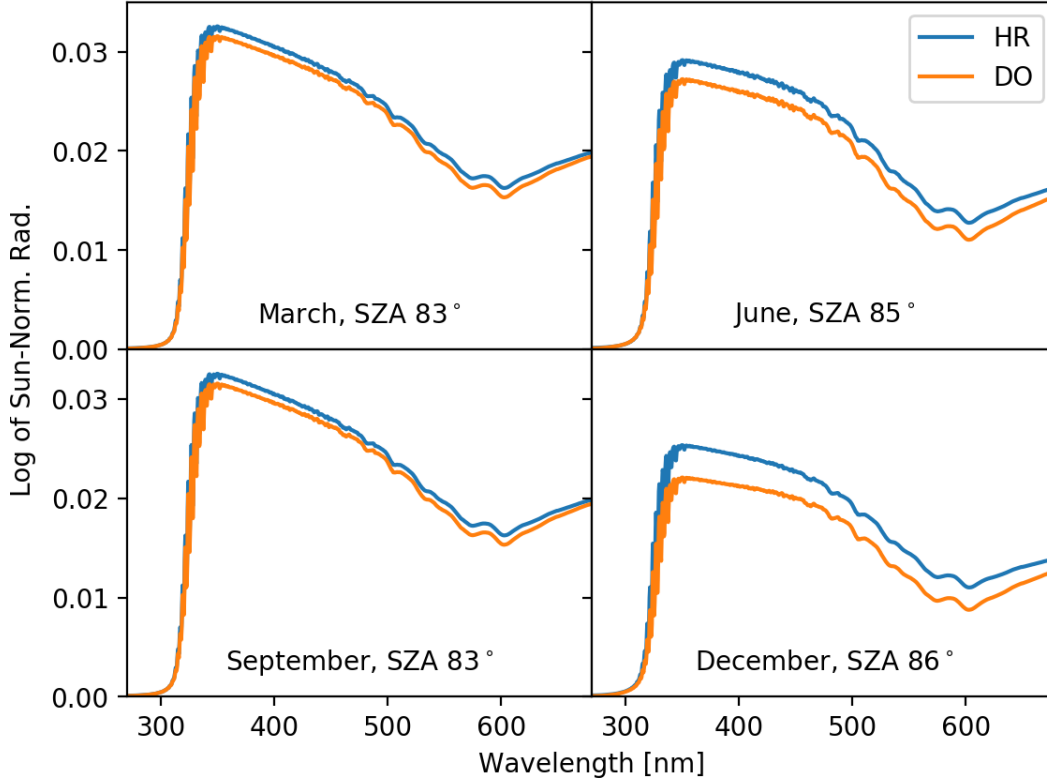


Figure 2.6. Comparison of the effect of using either the HR or DO SASKTRAN engine on the Sun-normalized measured radiances simulated for an instrument in geostationary orbit above 0°N - 100°W , pointing towards the Canadian Oil Sands (57°N - 112°W), one hour past local sunrise on the 21st day of four different months in 2022. The solar zenith angle (SZA) corresponding to each measurement scenario is shown.

2.3 Atmospheric Ozone and Nitrogen Dioxide

2.3.1 Ozone and Nitrogen Oxide Pollution

Ozone (O_3) and the two most important nitrogen oxides (NO_x), nitric oxide (NO) and nitrogen dioxide (NO_2), are toxic chemicals that are constituents of air pollution in the troposphere with both natural and anthropogenic sources (Mayer, 1999). Measurements of these species in the troposphere are thus crucial for creating air quality forecasts. Tropospheric NO_x and ozone concentrations have been shown to have increased since pre-industrial times and so the monitoring of them is important for policy makers (Ehhalt et al., 2001).

Tropospheric NO_x is generated as a by-product of high-temperature combustion (Boningari & Smirniotis, 2016), through nitrogen cycling in soils (Williams et al., 1987), and through chemical reactions in the atmosphere (Greenblatt & Ravishankara, 1990). Sources of NO_2 from high-temperature combustion includes natural causes, such as the interaction of lightning with air, and anthropogenic causes, such as through the burning of fossil fuels and biomasses. These anthropogenic sources are of increased importance as it has been shown that emissions due the burning of fossil fuels and biomasses have increased by a factor of three to six since pre-industrial times (Jaeglé et al., 2005). Sources of tropospheric ozone include stratosphere-troposphere exchange and photochemical reactions, of which NO_x is a common reactant (Lelieveld & Dentener, 2000).

Studies have shown that exposure to either ozone or NO_x by humans is harmful, with recommended safe concentrations exceeded regularly in large cities (Boningari & Smirniotis, 2016; Chaloulakou et al., 2008; Last et al., 1994). Another negative impact of NO_x is the creation of acid rain (Boningari & Smirniotis, 2016). Studies have shown negative effects of ozone on vegetation, which could cause issues for future global food security (Musselman & Massman, 1998; Tai et al., 2014).

2.3.2 Diurnal Variations of Nitrogen Oxides

The atmospheric concentrations of NO and NO_2 are most strongly governed by the chemical reactions



where M is some non-interacting molecule (Chameides, 1978; Jaeglé et al., 1994). As Eq. (2.23a) requires solar radiation, there are natural diurnal (daily) variations in stratospheric NO and NO_2 . Typical diurnal variations for NO and NO_2 near an altitude of 19 km, adapted from Wennberg et al. (1994), are shown in Fig. 2.7. Various models, such as that

by Prather and Jaffe (1990), are used to approximate the diurnal variations of atmospheric species such as NO and NO₂. These models require information such as the background pressure and temperature vertical profiles, the albedo, long-lived tracers (N₂O, H₂O, CH₄), and the NO_y, Cl_y, and Br_y families (Adams et al., 2016).

Due to timescales on the order of minutes to seconds for the reactions in Eqs. (2.23a), (2.23b) and (2.23d), the concentrations of NO and NO₂ reach a steady state in daytime or nighttime. Consequently, the concentration of either NO or NO₂ gives information about the concentration of the other. Only NO₂ is included in the remainder of the discussion herein as it is relevant to the remote sensing instruments used in the present work.

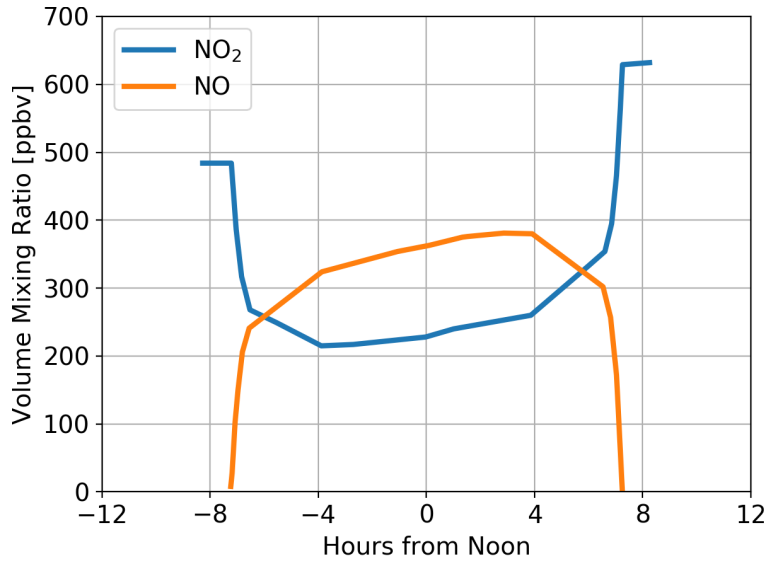


Figure 2.7. Empirically-derived diurnal dependencies of NO and NO₂ volumetric concentrations (in parts per billion) near an altitude of 19 km, adapted from Wennberg et al. (1994). The diurnal dependencies are verified by Wennberg et al. (1994) using chemiluminescence and laser-diode absorption instrument measurements on 12 May 1993.

2.3.3 Remote Sensing of Tropospheric Ozone and Nitrogen Dioxide

The measurement of air pollution in the troposphere using optical instruments on satellites allows for the analysis of long-term trends with coverage over the majority of the globe. Nadir-viewing instruments are used for these measurements as they are able to probe down to the ground, allowing for the measurement of the entire troposphere. Combining instrument measurements with information about the optical properties of the pollutants allows for the concentrations of the pollutants to be estimated.

Both ozone and NO_2 primarily absorb light, with the degree of absorption given by their respective absorption cross sections. Typical absorption cross sections for ozone and NO_2 are shown in Fig. 2.8 over wavelength ranges relevant to the satellite optical instruments discussed herein. Combining cross section data with optical measurements and radiative transfer modelling allows for the concentrations of the species in question to be estimated. Ozone was first measured remotely in 1921 using the ozone spectral information between 290 to 315 nm (Fabry & Buisson, 1921). The Backscatter UltraViolet instrument on Nimbus IV (Heath et al., 1973) was the first to measure ozone from space, and the number of instruments remotely measuring atmospheric ozone has been growing at an increasing rate since then. NO_2 was first measured remotely in 1973 by taking advantage of the prominent spectral features between near 430 and 450 nm (Brewer et al., 1973) and has since been measured by other satellite instruments using these spectral features (e.g., Boersma et al., 2007; Richter and Burrows, 2002; Sioris et al., 2004; Valks et al., 2011).

Standard ozone and NO_2 vertical density profiles in the troposphere and stratosphere for various latitudes and months are shown in Fig. 2.9. As atmospheric remote sensing satellites operate at altitudes above 400 km, the instruments must look through the stratosphere to see the troposphere. Thus, as ozone and NO_2 have peaks in the stratosphere (see Fig. 2.9), a troposphere-stratosphere separation method is necessary to remove the stratospheric component of the measurements to get the tropospheric concentration needed for air pollution monitoring.

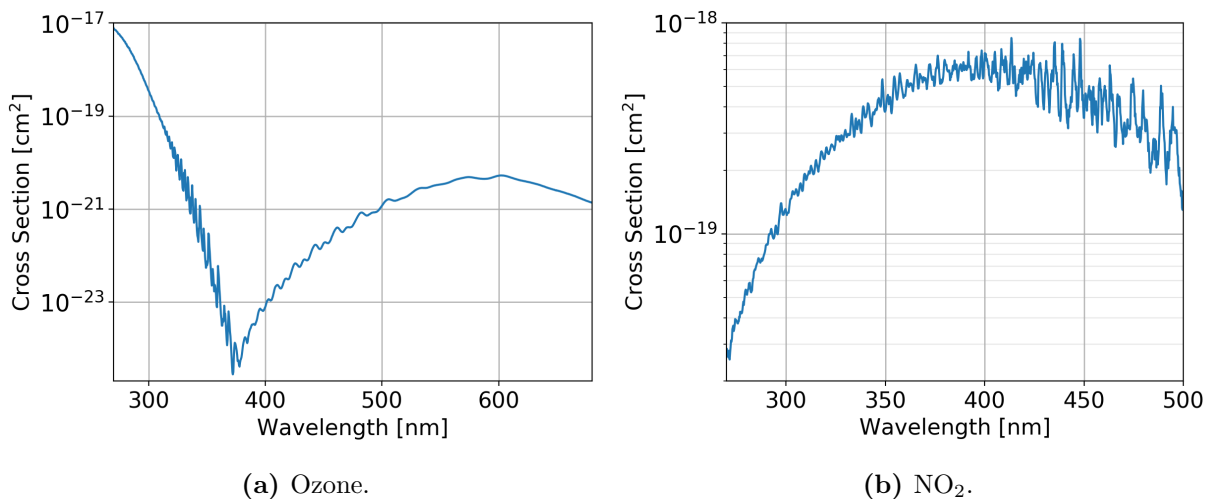


Figure 2.8. Typical ozone and NO₂ absorption cross sections over wavelengths relevant to the remote sensing instruments discussed herein. Cross sections are taken from experimentally determined data (Brion et al., 1998; Brion et al., 1993; Daumont et al., 1992; Malicet et al., 1995; Vandaele et al., 1998) for the temperature at an altitude of 20 km above 0°N-0°E on 21 March 2008 in the MSIS-90 model (Hedin, 1991).

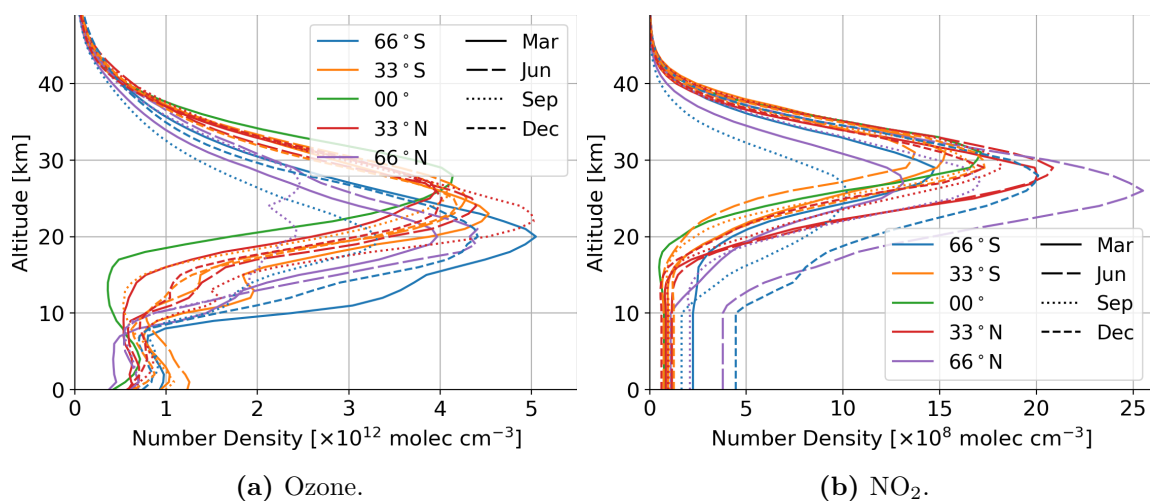


Figure 2.9. Ozone and NO₂ vertical density profiles taken from respective climatological datasets by Prather and Jaffe (1990) and McPeters et al. (1997). Each profile shown is the average of profiles from ten uniformly separated days of the given month. Each NO₂ profile is taken at 13:00 local time.

A commonly used ozone troposphere-stratosphere separation method first described by Singer and Wentworth (1957) involves measuring the back-scattered UV light with a nadir-viewing instrument at a fixed altitude above 40 km, e.g., on a satellite. Consider solar radiation of wavelength λ_0 , with λ_0 being between 270 and 370 nm. Because scattering and absorption processes are random, the λ_0 light measured by a satellite instrument will have resulted from λ_0 light that has penetrated a range of atmospheric depths before being scattered into the instrument sensor. Define $I(z, \lambda_0)$ as the measured radiance resulting from λ_0 light that has penetrated the atmosphere down to altitudes of z or higher before being scattered into the satellite instrument sensor. The radiance measured by the instrument resulting from λ_0 light that has penetrated down to any altitudes from the ground to just below the satellite is therefore $I(0, \lambda_0)$. The effective altitude, z_{eff} , for λ_0 light can be defined such that the ratio $\frac{I(z_{\text{eff}}, \lambda_0)}{I(0, \lambda_0)}$ is equal to some pre-defined threshold.

For example, as the ozone absorption cross section decreases with increasing wavelength from 270 to 370 nm (see Fig. 2.8), longer-wavelength light in this wavelength range is able to penetrate deeper in the atmosphere. This results in the effective altitude decreasing for increasing wavelength in this wavelength range. Given experimentally determined ozone absorption cross sections as functions of wavelength, the sensitivity of measurements to the ozone concentration at different altitudes can be resolved by making measurements over a range of wavelengths. Over a range of 280 to 300 nm for example, the ozone absorption cross section has sufficient variation to result in the effective altitude varying from approximately 13 to 48 km, depending on the specific viewing geometry (Singer & Wentworth, 1957). Thus, measurements around this wavelength range allows for the stratospheric and upper tropospheric ozone vertical density profiles to be estimated.

In contrast to ozone, the NO_2 absorption cross sections do not vary as much with wavelength (see Fig. 2.8), resulting in a low range of effective altitudes. As such, the NO_2 troposphere-stratosphere separation method requires additional assumptions. Common assumptions include the low longitude-dependent variations in stratospheric NO_2 column densities, insignificant tropospheric column densities over the middle of the Pacific Ocean or other unpolluted areas (Bucsela et al., 2013a; Bucsela et al., 2006; Leue et al., 2001; Richter & Burrows,

2002), the use of cloud data to determine stratospheric densities from cloudy measurements (Belmonte Rivas et al., 2015; Choi et al., 2014), and the use of global chemical transport models to fill in missing information (Boersma et al., 2007; Martin et al., 2002). An overview of these methods is given in Hilboll et al. (2013). The information from these additional assumptions is not sufficient to determine NO_2 density profiles at fine altitude resolutions, but does allow for separate tropospheric and stratospheric VCDs to be determined.

2.4 Relevant Instruments and Retrieval Algorithms

2.4.1 OMI

OMI is a nadir-viewing spectrometer onboard the NASA Aura satellite that has been operational since its launch in July 2004 (S. Bates, 2021; Levelt et al., 2006). It is in a sun-synchronous LEO with an ascending node near 13:45 local time. OMI measures over wavelengths from 270 to 500 nm with a spectral resolution less than 1 nm. Fig. 2.10 shows the viewing geometry of OMI. The instrument has a so-called push-broom scanning pattern, where it makes simultaneous measurements over a 2600-km swath that is perpendicular to the orbital ground track. The length of each swath consists of 60 ground pixels, each having an across-track width of 13 km and an along-track width of 12 or 24 km, depending on the mode of operation, near the center of the swath. ozone vertical density profiles are retrieved with measurements in the wavelength range of 270 to 310 nm (Liu et al., 2010), and NO_2 column densities are retrieved using OMI measurements in the wavelength range of 405 to 465 nm (Bucsela et al., 2013b).

The OMI ozone retrieval algorithm (Liu et al., 2010), which uses optimal estimation (see Section 2.5), retrieves not just the ozone profile but also some additional parameters to increase the number of degrees of freedom and improve the retrieval. The additional fit parameters include those for surface albedo, cloud fraction, scaling factors for the Ring effect, radiance/irradiance wavelength shifts, wavelength shifts between radiance and ozone cross sections, and scaling factors for the mean fitting residuals derived from one orbit of retrievals using all the other parameters (Liu et al., 2010).

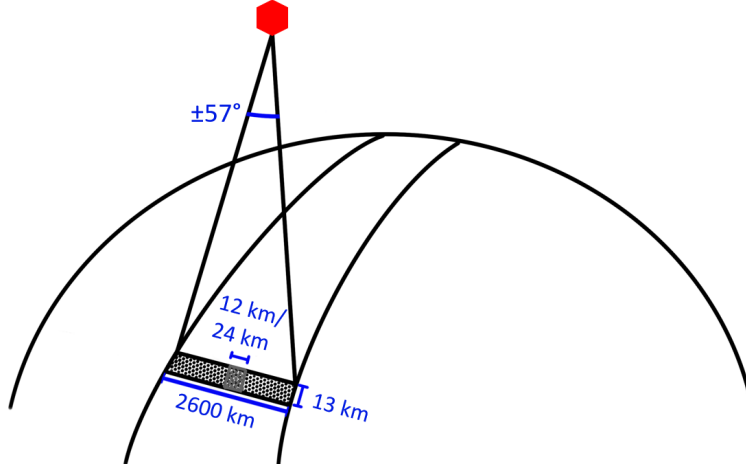


Figure 2.10. OMI viewing geometry, adapted from Bucselá et al. (2016). Relative lengths are exaggerated for illustrative purposes.

The ozone retrieval algorithm uses the VLIDORT modelling for the calculation of the transfer of light originating from the Sun through the atmosphere to the remote sensing instrument (Spurr, 2006). VLIDORT models the attenuation of the input solar radiation and the single scatter contribution with a spherical atmosphere, but models the higher-order scattering with a plane-parallel atmosphere. A spherical atmosphere for the solar attenuation and single scattering minimizes errors resulting from the relatively large viewing zenith angle towards either end of the OMI push-broom field of view.

The OMI NO₂ Standard Product (OMI-SP), processed by NASA, performs troposphere-stratosphere separation as follows (Bucselá et al., 2013b; Bucselá et al., 2016). As the stratosphere contains the vast majority of NO₂ over most of the Earth, modeled NO₂ tropospheric column densities from the Global Modeling Initiative (GMI) are used for the tropospheric densities over regions with low pollution expected, such as the Pacific Ocean. These low-pollution regions are defined as having GMI tropospheric column densities below some pre-determined threshold. In these regions, the stratospheric component is calculated by subtracting the modeled tropospheric contribution from the OMI-measured total column density. In other regions that have sufficient cloud fractions to effectively obscure the troposphere, the stratospheric column densities are extracted from the OMI measurements using a

priori cloud data. Regions are masked if the modeled tropospheric contribution is above the pre-defined threshold or there is a low cloud fraction. The stratospheric column density over a masked region is calculated using an algorithm that interpolates and smooths the stratospheric column densities from nearby unmasked regions. The tropospheric column density over a masked region is then calculated by subtracting the stratospheric column density from the measured total column density over the region.

Assumptions of the OMI-SP troposphere-stratosphere separation algorithm includes the independence between stratospheric and tropospheric column densities, the low latitudinal and longitudinal variations in stratospheric column densities, and the accuracy of the GMI models. OMI-SP NO₂ versions 2 and 4 are the two OMI NO₂ data products discussed herein. The main difference between the two versions is that the version 4 data product has a modified spectral fitting step that greatly reduces a positive bias in the SCDs of the version 2 data product, as well as improved cloud and surface treatments (Krotkov et al., 2017; Lamsal et al., 2021; Marchenko et al., 2015).

2.4.2 TROPOMI

TROPOMI is a nadir-viewing spectrometer of ESA onboard the Sentinel-5 Precursor that has been operational since its launch in October 2017 (van Geffen et al., 2020; Lorente et al., 2021; Veefkind et al., 2012). It is in a sun-synchronous LEO with an ascending node at approximately 13:30 local time. The goal of TROPOMI is to continue the data records of OMI and the SCanning Imaging Absorption spectromETER for Atmospheric CartographY (SCIAMACHY) instrument (Burrows et al., 1995), both of which are heritage to the TROPOMI design. It has an improved spatial resolution of 7.2 km compared to OMI with a spatial resolution as low as 12 km (van Geffen et al., 2020). NO₂ is retrieved using TROPOMI measurements in the UV and visible band (270–500 nm). NO₂ data resulting from the version 1.3.0 processor is used in the present work.

The troposphere-stratosphere separation of NO₂ is done using data assimilation (van Geffen et al., 2019). This involves regularly updating a chemical transport model of the atmosphere so that the simulated stratospheric NO₂ SCDs best match those of the TROPOMI measurements

over areas with insignificant tropospheric NO₂ levels.

Some research has found a negative bias of 20% to 30% in TROPOMI tropospheric VCDs relative to those of OMI for measurements from February to June 2018 (C. Wang et al., 2020) while other research has found a positive bias of approximately 5% in the geometric column densities, which are an approximation of the total column densities, in July 2018 (van Geffen et al., 2020). Nonetheless, the significantly higher resolution of TROPOMI measurements provides a large advantage over the predecessor instrument OMI.

2.4.3 OSIRIS

OSIRIS is a limb-viewing spectrograph onboard the Odin satellite that has been operational since its launch in February 2001 (Broman et al., 2021; Llewellyn et al., 2004). It is in a sun-synchronous LEO with an ascending node near 18:00 local time. OSIRIS measures wavelengths from 280 to 800 nm with a resolution of approximately 1 nm. NO₂ vertical density profiles extending from as low as 5 km to as high as 60 km, depending on the retrieval algorithm, are retrieved using OSIRIS measurements in the wavelength range of 435 to 451 nm (Haley et al., 2004). This wavelength range is used as it is where NO₂ is the dominant absorber.

OSIRIS NO₂ version 3 (Haley & Brohede, 2007), 6 (Sioris et al., 2017), and 7 (Dubé et al., 2021) are the three data products discussed herein. Compared to the previous public-released version 3 data product, version 6 uses a more accurate successive-orders-of-scattering version of SASKTRAN, a Multiplicative Algebraic Reconstruction Technique inversion (Degenstein et al., 2009), and a wider spectral fitting window. This results in a higher signal-to-noise ratio and a deeper penetration of the atmosphere compared to version 3 (Sioris et al., 2017). The version 7 data product is the newest version (Dubé et al., 2021) and is expected to replace the current publicly-released version 6 data product. Compared to version 6, the fitting of the OSIRIS spectral point spread function is done with solar Fraunhofer lines instead of pre-flight calibrated values. Additionally, the cloud and aerosol discrimination is improved, allowing for more profiles to be retrieved down to the lower stratosphere and upper troposphere. The version 7 data product is shown to better agree with the validated version 3 data product

compared to the version 6 data product, as discussed in Section 4.3.1. The version 3, version 6, and version 7 NO₂ profiles are retrieved over altitudes 10–46 km with a 2-km resolution, 10.5–39.5 km with a 1-km resolution, and 5.5–59.5 km with a 1-km resolution, respectively.

2.4.4 GOME

GOME was a nadir-viewing spectrometer onboard the Second European Remote Sensing Satellite (ERS-2) of ESA, and was operational from its launch in April 1995 to 2012 (Burrows et al., 1999; Chehade et al., 2014). It was in a sun-synchronous LEO with a descending node at approximately 10:30 local time.

Ozone vertical density profiles for altitudes from 0 to 80 km, at a resolution of 1 km, are retrieved using GOME measurements in the wavelength range of 290 to 355 nm (Hoogen et al., 1999). The GOME ozone retrieval algorithm, which uses optimal estimation (see Section 2.5), retrieves not just the ozone profile but also some additional parameters to increase the number of degrees of freedom and improve the retrieval. The additional parameters include scaling factors for the surface albedo, the aerosol number density profile, the NO₂ number density profile, and the pressure profile, and a shift parameter for the temperature profile.

The ozone retrieval algorithm uses GOMETRAN (Rozanov et al., 1997) for the modelling of the transfer of light originating from the Sun through the atmosphere to the remote sensing instrument. Similar to VLIDORT used for the OMI retrievals, GOMETRAN attenuates the input solar radiation through a spherical atmosphere. However, all scattering processes, including the single scattering, are modelled with a plane-parallel atmosphere. The error associated with using a plane-parallel atmosphere is considered sufficiently small as the typical maximum GOME viewing angle is smaller than that of OMI.

2.4.5 TEMPO

TEMPO will be among the first instruments to measure atmospheric composition from a geostationary orbit when it is launched in 2022, and the first to do so over North America (Hou et al., 2020; Zoogman et al., 2017). TEMPO will be positioned directly above the

Equator near 100°W , with a field of regard extending from Mexico City to the Canadian oil sands and from the Atlantic to the Pacific. The field of regard, adapted from Zoogman et al. (2017), is shown in Fig. 2.11. The TEMPO spectrometer measures in the UV and visible light wavelength ranges to retrieve ozone, NO_2 , and other species related to tropospheric pollution. As the field of regard covers a significant portion of the population of Canada, TEMPO provides an opportunity to improve Canadian air quality forecasts. Challenges in retrieving tropospheric species such as ozone at the high latitudes of Canada include the large solar angles, the greater abundance and variability of stratospheric absorbers, and the greater variability and uncertainties of surface albedos (Zoogman et al., 2017).

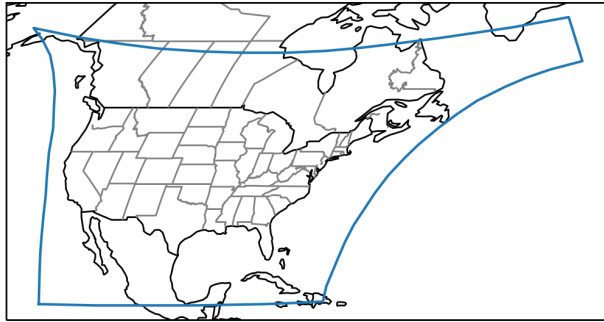


Figure 2.11. The TEMPO field of regard, with boundary data extracted from Zoogman et al. (2017).

The ozone profile retrieval algorithm uses wavelength ranges 290–345 nm (UV) and 540–650 nm (visible). The addition of wavelengths in the visible range improves the retrieval in the lower troposphere, but increases the sensitivity of measurements to surface reflectance due to the low ozone absorption, or low optical depth, in this wavelength range. The retrieval algorithms for LEO instruments GOME and OMI have been adapted and baselined for simulated TEMPO measurements (Hoogen et al., 1999; Liu et al., 2010; Liu et al., 2020). Following the OMI retrieval algorithm, the adapted TEMPO retrieval algorithm performs radiative transfer modelling using VLIDORT, which models the attenuation of the input solar radiation and the single scatter contribution with a spherical atmosphere and spherical Earth, but models the higher-order scattering with a plane-parallel Earth-atmosphere geometry (Spurr, 2006). The potential errors in the retrievals due to ignoring the curvature of the

atmosphere and Earth for the higher-order scattering is expected to be more significant for larger viewing zenith angles, e.g., when TEMPO is looking towards Canada. This presents an opportunity for Canada to implement an alternative radiative transfer model to improve ozone retrievals over the Canadian portion of the TEMPO field of regard.

2.4.6 MLS

The Microwave Limb Sounder (MLS) is a limb-viewing spectrometer onboard the NASA Aura satellite that has been operational since its launch in July 2004 (W. Wang et al., 2021; Waters et al., 2006). Similar to the OMI instrument on Aura, it is in a sun-synchronous LEO with an ascending node at 13:45 local time. MLS measures in the direction ahead of the satellite, within the orbital plane, with tangent altitudes ranging from 10 to 50 km. MLS measures microwave radiation in broad spectral bands centered near 118, 190, 240, and 640 GHz, and 2.5 THz. Ozone profiles extending from the upper troposphere to the mid-mesosphere are retrieved using MLS measurements in any one of the bands centered near 190, 240, or 640 GHz. The band centered near 240 GHz is primarily used for the retrieval of ozone profiles as the spectral region has strong ozone lines and the upper tropospheric absorption is sufficiently small to allow measurements of upper tropospheric ozone.

2.5 Optimal Estimation

Optimal estimation is a commonly used retrieval algorithm based on Bayesian statistics (Rodgers, 2000). The algorithm is designed to retrieve an atmospheric state vector (\mathbf{x}) at some region of the atmosphere, using a measurement vector (\mathbf{y}) measured at said region and an associated measurement covariance matrix (\mathbf{S}_y). The atmospheric state vector generally consists of number densities of the species vertical profile to be retrieved, but can also include other parameters, sometimes called fit parameters, to give more flexibility in the retrieval to determine the desired species profile. The measurement vector typically contains Sun-normalized radiances measured by an instrument, and the measurement covariance matrix is defined by the measurement noise and by the dependence of one measurement vector element to another. However, the measurement vector elements are commonly assumed to

be independent of one another, resulting in a diagonal measurement covariance matrix.

Retrievals are fundamentally under-determined as the measurements do not contain enough information to fully determine the atmospheric state. To this end, optimal estimation regularizes the problem by using an *a priori* (best-estimate) atmospheric state, \mathbf{x}_a , with an associated covariance matrix, \mathbf{S}_a , based on the error in the *a priori* state. A forward model $\mathbf{F}(\mathbf{x})$, defined using a radiative transfer model, is used to calculate a simulated instrument measurement vector given an atmospheric state \mathbf{x} .

2.5.1 Derivation

Optimal estimation uses the maximum *a posteriori* method where the *a posteriori* distribution, defined as

$$P(\mathbf{x}|\mathbf{y}) = \frac{P(\mathbf{y}|\mathbf{x})P(\mathbf{x})}{P(\mathbf{y})}, \quad (2.24)$$

is maximized with respect to \mathbf{x} . The probability distribution of the measurement vector \mathbf{y} given an atmospheric state \mathbf{x} , $P(\mathbf{y}|\mathbf{x})$, is defined by assuming an expected value $\mathbf{F}(\mathbf{x})$ and a covariance matrix \mathbf{S}_y . The *a priori* probability distribution of the atmospheric state \mathbf{x} , $P(\mathbf{x})$, is defined by assuming an expected value \mathbf{x}_a and a covariance matrix \mathbf{S}_a . Mathematically, the covariance matrices are defined by

$$\begin{aligned} \mathbf{S}_y &= \text{E} [\{\mathbf{F}(\mathbf{x}) - \mathbf{y}\} \{\mathbf{F}(\mathbf{x}) - \mathbf{y}\}^\top] \text{ and} \\ \mathbf{S}_a &= \text{E} [(\mathbf{x} - \mathbf{x}_a)(\mathbf{x} - \mathbf{x}_a)^\top], \end{aligned} \quad (2.25)$$

where $\text{E}[\mathbf{z}]$ is the expected value of \mathbf{z} . In practice, these matrices are typically defined by simply using assumed errors and correlations in the measurement elements and in the *a priori* atmospheric state parameters.

To make the least number of assumptions about the distributions, $P(\mathbf{y}|\mathbf{x})$ and $P(\mathbf{x})$ are taken as normal distributions as each is defined only by an expected value and a covariance matrix. Furthermore, normal distributions are commonly successful at approximating real-world events. Given the form of a multivariate normal distribution, the aforementioned

probability distributions are given by

$$\begin{aligned} P(\mathbf{y}|\mathbf{x}) &\propto \exp \left\{ -\frac{1}{2} [\mathbf{y} - \mathbf{F}(\mathbf{x})]^\top \mathbf{S}_y^{-1} [\mathbf{y} - \mathbf{F}(\mathbf{x})] \right\} \text{ and} \\ P(\mathbf{x}) &\propto \exp \left[-\frac{1}{2} (\mathbf{x} - \mathbf{x}_a)^\top \mathbf{S}_a^{-1} (\mathbf{x} - \mathbf{x}_a) \right]. \end{aligned} \quad (2.26)$$

Note from Eq. (2.24) that the denominator, $P(\mathbf{y})$, of the *a posteriori* distribution, $P(\mathbf{x}|\mathbf{y})$, is independent on \mathbf{x} . Thus, maximizing $P(\mathbf{x}|\mathbf{y})$ with respect to \mathbf{x} in the optimal estimation method can be re-expressed as minimizing

$$\begin{aligned} -2 \ln [P(\mathbf{x}|\mathbf{y})] &= -2 \ln [P(\mathbf{y}|\mathbf{x})] + (-2) \ln [P(\mathbf{x})] + c_0 \\ &= [\mathbf{y} - \mathbf{F}(\mathbf{x})]^\top \mathbf{S}_y^{-1} [\mathbf{y} - \mathbf{F}(\mathbf{x})] + (\mathbf{x} - \mathbf{x}_a)^\top \mathbf{S}_a^{-1} (\mathbf{x} - \mathbf{x}_a) + c, \end{aligned} \quad (2.27)$$

where c_0 and c are independent on \mathbf{x} and Eq. (2.26) was used to define $\ln [P(\mathbf{y}|\mathbf{x})]$ and $\ln [P(\mathbf{x})]$. Without c , the right-hand side of Eq. (2.27) is often referred to as the cost function,

$$\chi^2(\mathbf{x}) = [\mathbf{y} - \mathbf{F}(\mathbf{x})]^\top \mathbf{S}_y^{-1} [\mathbf{y} - \mathbf{F}(\mathbf{x})] + (\mathbf{x} - \mathbf{x}_a)^\top \mathbf{S}_a^{-1} (\mathbf{x} - \mathbf{x}_a). \quad (2.28)$$

It is clear that minimizing Eq. (2.27) is equivalent to minimizing the cost function $\chi^2(\mathbf{x})$, and this is accomplished by solving for the zero of the multivariate derivative of Eq. (2.27).

This results in

$$\mathbf{0} = \mathbf{g}(\mathbf{x}) \equiv -\nabla_{\mathbf{x}} \ln [P(\mathbf{x}|\mathbf{y})] = -\mathbf{K}^\top \mathbf{S}_y^{-1} [\mathbf{y} - \mathbf{F}(\mathbf{x})] + \mathbf{S}_a^{-1} (\mathbf{x} - \mathbf{x}_a), \quad (2.29)$$

where $\mathbf{K} = \mathbf{K}(\mathbf{x}) \equiv \nabla_{\mathbf{x}} \mathbf{F}(\mathbf{x})$ is the Jacobian matrix of the forward model. The Jacobian matrix element at row r and column c can be calculated using a perturbation of the state as

$$K_{r,c} = \frac{F_r(\mathbf{x} + \delta x_c \mathbf{e}_c) - F_r(\mathbf{x})}{\delta x_c}, \quad (2.30)$$

where $F_r(\mathbf{x})$ is element r of the forward model vector $\mathbf{F}(\mathbf{x})$, δx_c is the change in the atmospheric state vector at element c , and \mathbf{e}_c is the c^{th} unit atmospheric state vector such that $\mathbf{x} + \delta x_c \mathbf{e}_c$ is the same as \mathbf{x} except that the value at element c is replaced with $x_c + \delta x_c$. The rows of the Jacobian matrix are referred to as weighting functions, and hence the Jacobian matrix is sometimes referred to in literature as the weighting function matrix.

Using Newton's method to solve Eq. (2.29) results in the iterative equation

$$\mathbf{x}_{i+1} = \mathbf{x}_i - [\nabla_{\mathbf{x}} \mathbf{g}(\mathbf{x}_i)]^{-1} \mathbf{g}(\mathbf{x}_i), \quad (2.31)$$

where

$$\nabla_{\mathbf{x}}\mathbf{g}(\mathbf{x}) = \mathbf{K}^\top \mathbf{S}_y^{-1} \mathbf{K} + \mathbf{S}_a^{-1} - [\nabla_{\mathbf{x}} \mathbf{K}^\top] \mathbf{S}_y^{-1} [\mathbf{y} - \mathbf{F}(\mathbf{x})], \quad (2.32)$$

and $\nabla_{\mathbf{x}} \mathbf{K}^\top$ is the second derivative of the forward model. $\nabla_{\mathbf{x}} \mathbf{K}^\top$ can be thought of as a three-dimensional matrix where the element at indices (i, j, k) is given by

$$(\nabla_{\mathbf{x}} \mathbf{K}^\top)_{i,j,k} = \frac{\partial K_{k,j}(\mathbf{x})}{\partial x_i} = \frac{\partial^2 F_k(\mathbf{x})}{\partial x_i \partial x_j}. \quad (2.33)$$

In most retrieval problems, the second derivative of the forward model is negligibly small. Ignoring this term results in the Gauss-Newton method, in which case Eq. (2.31) is approximated as

$$\mathbf{x}_{i+1} = \mathbf{x}_i + (\mathbf{K}_i^\top \mathbf{S}_y^{-1} \mathbf{K}_i + \mathbf{S}_a^{-1})^{-1} [\mathbf{K}_i^\top \mathbf{S}_y^{-1} (\mathbf{y} - \mathbf{F}(\mathbf{x}_i)) - \mathbf{S}_a^{-1} (\mathbf{x}_i - \mathbf{x}_a)], \quad (2.34)$$

where $\mathbf{K}_i \equiv \mathbf{K}(\mathbf{x}_i)$. The initial state, \mathbf{x}_0 , is generally taken as the *a priori* state \mathbf{x}_a and the state once the algorithm stops or converges is denoted by $\hat{\mathbf{x}}$.

2.5.2 Averaging Kernel Matrix

An important descriptor of the behaviour of the retrieval is the averaging kernel matrix, \mathbf{A} . For example, if the atmospheric state vector (\mathbf{x}) describes an ozone profile, then each row of \mathbf{A} , called an averaging kernel, describes how sensitive a given altitude of the retrieved ozone profile ($\hat{\mathbf{x}}$) is to each altitude of the actual ozone profile (\mathbf{x}_{true}). The element of \mathbf{A} at row r and column c is given by

$$A_{r,c} = \frac{\partial \hat{x}_r}{\partial x_{\text{true},c}}, \quad (2.35)$$

where \hat{x}_r is element r of the retrieved state vector $\hat{\mathbf{x}}$ and $x_{\text{true},c}$ is element c of the true state vector \mathbf{x}_{true} . Instead of using perturbations, \mathbf{A} can instead be calculated algebraically as

$$\mathbf{A} = (\mathbf{K}^\top \mathbf{S}_y^{-1} \mathbf{K} + \mathbf{S}_a^{-1})^{-1} \mathbf{K}^\top \mathbf{S}_y^{-1} \mathbf{K}, \quad (2.36)$$

where the Jacobian \mathbf{K} is taken at the final iteration, after sufficient convergence. The averaging kernel matrix also quantifies the bias in the retrieval due to using an *a priori* atmospheric state. Instead of retrieving \mathbf{x}_{true} , the algorithm retrieves

$$\mathbf{x}_a + \mathbf{A} (\mathbf{x}_{\text{true}} - \mathbf{x}_a). \quad (2.37)$$

Thus, the retrieved profile approaches \mathbf{x}_{true} as \mathbf{A} approaches an identity matrix, that is, as the sensitivity for a given altitude of the retrieved profile peaks increasingly closer to said altitude. From Eq. (2.36), this occurs as the magnitude of the determinant of $\mathbf{S}_{\mathbf{a}}$ increases or as the magnitude of the determinant of $\mathbf{S}_{\mathbf{y}}$ decreases. As all covariance matrices are positive semi-definite and therefore have non-negative determinants, this can be accomplished by scaling $\mathbf{S}_{\mathbf{a}}$ by a factor greater than 1 or by scaling $\mathbf{S}_{\mathbf{y}}$ by a factor less than 1. In either case, this is equivalent to assuming an increased error in the *a priori* state relative to that of the measurement, causing the retrieved state to be affected less by the *a priori* state and more by the measurement vector. However, as the measurement vector does not contain enough information to fully determine the profile, scaling up $\mathbf{S}_{\mathbf{a}}$ or scaling down $\mathbf{S}_{\mathbf{y}}$ too much can worsen the results or cause strange behaviour due to over-fitting. As such, the relative scaling can be varied with trial-and-error to determine a value that gives reasonable results.

2.5.3 Levenberg-Marquardt Method and Convergence Criteria

Similar to the Newton method, the Gauss-Newton method discussed above can be shown to converge quadratically. The method works better when the state is near the solution, but can be slow due to repeated overshooting when far from the solution. A common way to fix this is with the Levenberg-Marquardt (LM) Method. For this method, Eq. (2.34) is replaced with

$$\mathbf{x}_{i+1} = \mathbf{x}_i + (\mathbf{K}_i^T \mathbf{S}_{\mathbf{y}}^{-1} \mathbf{K}_i + \mathbf{S}_{\mathbf{a}}^{-1} + \delta \mathbf{D})^{-1} [\mathbf{K}_i^T \mathbf{S}_{\mathbf{y}}^{-1} (\mathbf{y} - \mathbf{F}(\mathbf{x}_i)) - \mathbf{S}_{\mathbf{a}}^{-1} (\mathbf{x}_i - \mathbf{x}_{\mathbf{a}})], \quad (2.38)$$

where \mathbf{D} is a diagonal matrix with the same shape as $\mathbf{S}_{\mathbf{a}}$, and δ is referred to as the LM damping factor. The matrix \mathbf{D} can be an identity matrix, but it is often chosen to be $D = \text{diag}(\mathbf{K}_i^T \mathbf{S}_{\mathbf{y}}^{-1} \mathbf{K}_i)$, where $\text{diag}(\mathbf{C})$ is the same as \mathbf{C} except that the off-diagonal terms are set to zero. Note that Eq. (2.38) simplifies to the Gauss-Newton method for $\delta = 0$. As δ approaches infinity, it simplifies to the gradient descent method,

$$\begin{aligned} \mathbf{x}_{i+1} &= \mathbf{x}_i + \delta^{-1} [\mathbf{K}_i^T \mathbf{S}_{\mathbf{y}}^{-1} (\mathbf{y} - \mathbf{F}(\mathbf{x}_i)) - \mathbf{S}_{\mathbf{a}}^{-1} (\mathbf{x}_i - \mathbf{x}_{\mathbf{a}})] \\ &= \mathbf{x}_i - \frac{1}{2\delta} \nabla_{\mathbf{x}} \chi^2(\mathbf{x}). \end{aligned} \quad (2.39)$$

The initial value for δ is chosen arbitrarily, and then it is allowed to vary each iteration depending on the change in the cost function χ^2 . If χ^2 is higher at the next iteration, the

state is not updated and δ is increased, moving closer to the gradient descent method. If χ^2 is lower at the next iteration, the state is updated and δ is decreased, moving closer to the Gauss-Newton method. Generally, δ is increased or decreased each iteration by a constant factor that can be chosen by experimenting with different values.

For a convergence criteria, it is common to use the percent difference in the cost function χ^2 between the current iteration and the next. In other words, convergence is assumed if $\chi^2(\mathbf{x}_i)$ is sufficiently close to $\chi^2(\mathbf{x}_{i+1})$, where $\chi^2(\mathbf{x})$ is calculated using Eq. (2.28). However, if using the LM method and δ is large, then from Eq. (2.39) it is clear that $\|\mathbf{x}_{i+1} - \mathbf{x}_i\|$ would be small, resulting in a small change in χ^2 between iterations. To prevent a premature convergence due to a potentially large δ , $\chi^2(\mathbf{x}_{i+1})$ is instead calculated as $\chi^2(\mathbf{x}_{\text{GN},i+1})$, where $\mathbf{x}_{\text{GN},i+1}$ is the next-iteration state calculated with the Gauss-Newton method (or LM method with $\delta = 0$), that is, with Eq. (2.34). If $\chi^2(\mathbf{x}_i)$ is sufficiently close to $\chi^2(\mathbf{x}_{\text{GN},i+1})$, the state is considered to have converged and the algorithm is stopped. Otherwise, the algorithm continues and the next atmospheric state is calculated again, this time with the LM method (Eq. (2.38)) to get \mathbf{x}_{i+1} . The criteria defining “sufficiently close” can be chosen arbitrarily or by trial and error.

Note that updating the atmospheric state with Eq. (2.38) and calculating the cost function with Eq. (2.28) requires running the forward model to calculate $\mathbf{F}(\mathbf{x}_i)$ once for each atmospheric state \mathbf{x}_i . However, calculating the cost function (Eq. (2.28)) for the Gauss-Newton-calculated atmospheric state, $\mathbf{x}_{\text{GN},i+1}$, to check the convergence criteria requires running the forward model an additional time each iteration. To avoid the additional, computationally expensive forward model run each iteration, the forward model is linearized about \mathbf{x}_i such that the forward model vector for the state $\mathbf{x}_{\text{GN},i+1}$ is approximated as

$$\mathbf{F}(\mathbf{x}_{\text{GN},i+1}) \approx \mathbf{F}(\mathbf{x}_i) + \mathbf{K}_i \cdot (\mathbf{x}_{\text{GN},i+1} - \mathbf{x}_i) \quad (2.40)$$

in the calculation of $\chi^2(\mathbf{x}_{\text{GN},i+1})$ when checking the convergence criteria.

2.6 Non-Coincident Limb-Nadir Matching

Limb-nadir matching is a troposphere-stratosphere separation method to derive tropospheric column densities using both nadir and limb measurements. It involves combining limb mea-

measurements, which provide stratospheric column densities, with the nadir measurements, which provide the total column densities extending over both the troposphere and stratosphere. Assuming the limb and nadir measurements are sufficiently close in location and local solar time, the limb-measurement-derived stratospheric column densities can be subtracted from the nadir-measurement-derived total column densities to estimate the corresponding tropospheric column densities. Compared to conventional methods, the limb-nadir matching method has the advantage of using highly-validated limb-viewing instrument measurements instead of relying on global chemical transport models or additional assumptions about the distribution of atmospheric species. The limb-nadir matching method has been successfully done with the SCIAMACHY instrument, which makes both limb and nadir measurements nearly simultaneously, with the two measurements geographically close to each other (Beirle et al., 2010; Hilboll et al., 2013). The drawback to this method is that very few instruments make both limb and nadir measurements.

A recent paper attempts to solve this drawback by demonstrating the feasibility of performing the limb-nadir matching to derive tropospheric NO₂ column densities using non-coincident measurements from limb- and nadir-viewing instruments on separate satellites (Adams et al., 2016). Specifically, the paper describes the results of using the method with nadir-viewing OMI and limb-viewing OSIRIS NO₂ measurements. This so-called non-coincident limb-nadir matching method involves i) using a photochemical box model to shift the limb-measurement-derived stratospheric column densities in local solar time in order to match the local times of the nadir-measurement-derived total column densities, and ii) interpolating and smoothing the limb-measurement-derived stratospheric column densities from a period of time in geographic coordinates to match the coordinates of the nadir-measurement-derived total column densities. The non-coincident limb-nadir matching method is more practical than the coincident method due to the fact that there are sufficiently many limb- and nadir-viewing instruments in operation to result in many large overlapping periods of operation between limb-nadir instrument pairs. Future assessments of this method, particularly with different instruments and datasets, would provide a better understanding of the value in the method.

For this method, Adams et al. (2016) uses the version 2 OMI-SP and the version 3 OSIRIS NO₂ data products. SCD-dependent factors determined by Marchenko et al. (2015) are used to correct the well-known OMI NO₂ version 2 SCD positive bias. For the OSIRIS data, only the descending node measurements are used. This is to avoid the systematic bias between the descending and ascending nodes due to NO₂ diurnal variations resulting from different local solar times between the two nodes. Furthermore, only OSIRIS measurements with SZAs less than 88° are used in order to minimize the so-called diurnal effect or photochemical enhancement (Hendrick et al., 2006; McLinden et al., 2006) which is not currently accounted for in the OSIRIS NO₂ retrieval algorithm. This effect is strongest when the Sun is close to the horizon (i.e., SZA near 90°) and is due to the large range in local SZAs along the instrument LOS and the large diurnal variation of species such as NO₂. The non-coincident limb-nadir matching algorithm by Adams et al. (2016) is described in the following five steps.

First, OSIRIS vertical density profiles are extrapolated to each local solar hour (0-23) of each day so that they can eventually be interpolated to the local times of OMI measurements for corresponding days. As NO₂ is photochemically active and has strong diurnal variations (Mayer, 1999), especially during dusk and dawn when OSIRIS measurements are taken, a photochemical box model by Prather and Jaffe (1990), referred to in the present work as PRATMO, is used to extrapolate OSIRIS profile number densities over local solar time. This is done using the equation

$$n_{\text{OSIRIS}}(z, t_{\text{new}}, \Theta, d) = n_{\text{OSIRIS}}(z, t_{\text{OSIRIS}}, \Theta, d) \cdot \frac{n_{\text{model}}(z, t_{\text{new}}, \Theta, d)}{n_{\text{model}}(z, t_{\text{OSIRIS}}, \Theta, d)}, \quad (2.41)$$

where z is the altitude along the vertical profile, t_{OSIRIS} is the local solar time of the OSIRIS measurement, t_{new} is the local solar time to which the profiles are being extrapolated, Θ is the latitude, and d is the date of the measurement. This method has been successfully used to validate NO₂ profiles (Brohede et al., 2007) and merge data products (Brohede et al., 2008).

Second, OSIRIS NO₂ stratospheric VCDs are calculated for each local solar hour of each day by numerically integrating the profiles over altitude from the tropopause to the effective top of the stratosphere (ETS). The ETS is defined as the highest altitude of the version 6 OSIRIS

NO₂ data product: 39.5 km. It is assumed that the contribution to the VCDs from number densities above this altitude is negligibly small.

If a profile extends to or below the tropopause, it is interpolated to and cut off at the tropopause before integration. If a profile does not extend down to the tropopause, the VCD is extrapolated to the tropopause using PRATMO with the equation

$$V_{\text{strat}} = V_{\text{part}}^{\text{OSIRIS}} \cdot \left(\frac{V_{\text{strat}}^{\text{model}}}{V_{\text{part}}^{\text{model}}} \right), \quad (2.42)$$

where V_{strat} is the resulting extrapolated stratospheric VCD, $V_{\text{part}}^{\text{OSIRIS}}$ and $V_{\text{part}}^{\text{model}}$ are the OSIRIS and PRATMO VCDs resulting from integration over available OSIRIS altitudes, and $V_{\text{strat}}^{\text{model}}$ is the PRATMO VCD extending from the tropopause to the ETS.

Third, for each day of OMI VCD data, OSIRIS stratospheric VCDs from this day, the previous day, and the following day, are interpolated over latitude and longitude to create one 1°-by-1° gridded map per local solar hour. This three-day averaging window of OSIRIS data is chosen by Adams et al. (2016) as a favorable balance between spatial coverage and resolution of features. For each 1°-by-1° grid cell of each local solar hour of each day, weights are calculated for all OSIRIS VCDs of the corresponding local solar hour and three-day window. For the grid cell at latitude Θ and longitude Φ , the weight of the i^{th} OSIRIS VCD is given by

$$w_i(\Theta, \Phi) = \exp \left(- \left[\frac{(\Theta - \Theta_i)^2}{2\sigma_\Theta} + \frac{(\Phi - \Phi_i)^2}{2\sigma_\Phi} \right] \right), \quad (2.43)$$

where Θ_i and Φ_i are the OSIRIS VCD measurement tangent point latitude and longitude, respectively, and σ_Θ and σ_Φ are the standard deviations in the Gaussian weighting for latitude and longitude, respectively. Based on the OSIRIS measurement spatial coverage, σ_Θ and σ_Φ are taken as 6° and 10°, respectively. If the sum of all weights for a given grid cell of a given hour and day is less than 1, the grid cell is left empty. Otherwise, the weights in Eq. (2.43) are normalized such that $\sum_i w_i(\Theta, \Phi) = 1$, and the grid cell value is calculated as the mean of the OSIRIS VCDs, weighted by the normalized weights. This process is repeated to produce one stratospheric VCD map for each local solar hour of each day.

Fourth, the OSIRIS gridded stratospheric VCD maps for each local solar hour and day are interpolated to the local time and coordinates of each OMI measurement with which to be

matched. Note that each OMI measurement is used to calculate one tropospheric VCD and one stratospheric VCD in the OMI level 2 data.

Finally, for each OMI measurement, the corresponding OMI-minus-OSIRIS (OmO) tropospheric NO₂ VCD, $V_{\text{trop}}^{\text{OmO}}$, is calculated as

$$V_{\text{trop}}^{\text{OmO}} = V_{\text{trop}}^{\text{OMI}} + (V_{\text{strat}}^{\text{OMI}} - V_{\text{strat}}^{\text{OSIRIS}}) \cdot A_{\text{strat}}^{\text{OMI}}/A_{\text{trop}}^{\text{OMI}}, \quad (2.44)$$

where $V_{\text{trop}}^{\text{OMI}}$ and $V_{\text{strat}}^{\text{OMI}}$ are the tropospheric and stratospheric VCDs corresponding to the OMI measurement, $V_{\text{strat}}^{\text{OSIRIS}}$ is the matched OSIRIS stratospheric VCD, and $A_{\text{trop}}^{\text{OMI}}$ and $A_{\text{strat}}^{\text{OMI}}$ are the tropospheric and stratospheric AMFs corresponding to the OMI measurement.

3 Analysis of Canadian Ozone Retrievals for Simulated TEMPO Measurements

3.1 Introduction

The goal of the present chapter is to investigate the difference in ozone retrieval error, for simulated TEMPO measurements over Canada, due to the use of a radiative transfer model with a spherical geometry for all orders of scattering compared to the use of the planned VLIDORT model with a plane-parallel geometry for multiple-scattered light. The intention of this goal is to quantify potential benefits of implementing a radiative transfer model with a spherical geometry for all orders of scattering to retrieve ozone profiles over Canada with future TEMPO measurements compared to implementing the planned VLIDORT model. This goal is addressed by comparing the error in retrieved ozone profiles over Canada resulting from the use of the SASKTRAN DO engine, with a plane-parallel geometry for all orders of scattering, to the error resulting from the use of the SASKTRAN HR engine, with a spherical geometry for all orders of scattering. To this end, GOME- and OMI-based algorithms are first developed and compared to published results to validate the algorithms. The algorithms are then adapted for simulated TEMPO measurements and a statistical analysis is performed to determine expected errors associated with using a plane-parallel geometry instead of a spherical geometry.

The methodology of developing and validating the retrieval algorithms, and of performing the statistical analysis for the TEMPO-based retrieval algorithm, is detailed in Section 3.2. The corresponding results and discussion is found in Section 3.3. Finally, the work is concluded and future investigations towards the analysis of the best radiative transfer model

implementation for future TEMPO ozone retrievals over Canada is outlined in Section 3.4.

3.2 Methodology

The radiative transfer model, including the atmospheric model and the instrument optical spectrometer model, of the present work is implemented with the SASKTRAN software (Bourassa et al., 2008). The three SASKTRAN engines used for the present work are the discrete ordinates (DO), high resolution (HR), and high resolution single-scatter approximation (HRSSApprox) engines, all discussed in Section 2.2.7. The DO engine uses a purely plane-parallel Earth-atmosphere geometry while the HR engine uses a purely spherical Earth-atmosphere geometry (Zawada et al., 2015). The HRSSApprox engine is adapted from the HR engine to reduce the computational speed without significantly compromising the accuracy. Comparisons of results between the DO and HR engines are used in the present work to quantify the error in assuming a plane-parallel geometry versus a spherical geometry. The DO engine differs from VLIDORT, the planned radiative transfer model of the retrieval algorithm of the future TEMPO ozone retrievals, in that the DO engine uses a plane-parallel Earth-atmosphere geometry for all orders of scattering while VLIDORT uses a spherical Earth-atmosphere geometry up until the single-scatter radiance contribution and a plane-parallel geometry for all higher orders of scattering (Spurr, 2006). Nonetheless, the DO engine provides the closest comparison to VLIDORT that is available for the present work.

3.2.1 Atmospheric Model

The atmospheric model is set up in SASKTRAN with the atmosphere defined to consist of 80 1-km wide spherical shells, with edges at altitudes from 0 to 80 km, similar to the GOME retrievals (Hoogen et al., 1999). Number densities above an altitude of 80 km are sufficiently low that they have an insignificant effect on the radiative transfer. The model incorporates the SASKTRAN dry-air Rayleigh scattering model, which has been validated with the results of D. R. Bates (1984). The MSIS-90 model (Hedin, 1991) is used for the pressure, temperature, and number density of the air. The NO₂ vertical density profiles are

taken from a climatological dataset by Prather and Jaffe (1990). The ozone and NO₂ cross sections used in the model are taken from experimentally-determined values (Brion et al., 1998; Brion et al., 1993; Daumont et al., 1992; Malicet et al., 1995; Vandaele et al., 1998). The NO₂ and ozone cross sections are convolved down to the wavelength resolution of each instrument using the published full-width half maximum of the respective instrument.

An assumption in the atmospheric model is that the ozone vertical density profile that is varied in the retrieval algorithm is defined to be independent on latitude and longitude. This is a reasonable assumption as only the atmospheric region local to the intersection between the instrument LOS and the ground should have a significant effect on the measurement. Furthermore, even at the highest VZA of the present analyses (TEMPO measuring towards the Canadian Oil Sands), the difference in latitude between the LOS intersection with the ground and the LOS intersection with the effective top of the atmosphere (altitude of 80 km) is found to be at most 1.5° (see Appendix A). It is expected that the ozone profile does not vary significantly over such a small latitude difference, and so the aforementioned assumption about the ozone profile in the atmospheric model is reasonable.

3.2.2 Measurements and Instrument Models

The measurement vectors for the retrieval algorithm of the present work are simulated in SASKTRAN and do not account for instrument noise. The lack of instrument noise allows for easy analysis of the effect of each individual factor on the retrievals as there is less difference between the measurements and the forward model of the retrieval. The measurements are simulated by defining true values for the atmosphere, the Sun geometry, the position and orientation of the instrument, and the model of the instrument spectrometer, all using the SASKTRAN framework. This is unlike a real retrieval where the true values cannot be known exactly due to uncertainties.

In an ideal world with infinite computer resources, the instrument models for both the forward model of the retrieval and the simulated measurements would be perfect models of the instrument. Due to limited computer resources however, some assumptions must be made in the models. For simplicity, the instrument models for both the forward model and the

simulated measurements are assumed to have rectangular pixels. Because the cross sections are convolved down to the same wavelength resolution of each instrument, a delta function is used for the line shape. The simulated measurements are always calculated with the SASK-TRAN HR engine as it has the most realistic geometry, whereas the forward model of the retrieval can be defined to use any of the DO, HR, or HRSSApprox engine.

3.2.3 Retrieval Parameters

The initial atmospheric state of each retrieval is taken as the *a priori* (best estimate) atmospheric state, and the Levenberg-Marquardt (LM) Method (see Section 2.5.3) is used to iteratively update the state. The state at iteration i , \mathbf{x}_i , is considered to have converged if the cost function (Eq. (2.28)) at this state, \mathbf{x}_i , is within 0.001% of $\chi^2(\mathbf{x}_{\text{GN},i+1})$, where $\mathbf{x}_{\text{GN},i+1}$ is the state at the next iteration calculated using the Gauss-Newton method (Eq. (2.34)), and $\chi^2(\mathbf{x}_{\text{GN},i+1})$ is calculated with the forward model linearized about the state \mathbf{x}_i (Eq. (2.40)) to reduce the number of runs of the computationally expensive forward model by a factor of two. Nonetheless, a maximum of ten iterations is specified for the retrieval algorithm. The value of ten is chosen as a compromise between ensuring all retrieval cases converge sufficiently and limiting the time required to run the retrievals.

The standard deviation in each *a priori* atmospheric state parameter is defined as the corresponding *a priori* atmospheric state parameter multiplied by a common standard deviation factor. Based on other retrieval algorithms (Hoogen et al., 1999; Liu et al., 2005), the *a priori* atmospheric state covariance matrix is defined using a correlation length r_c and the standard deviations, $\sigma_{a,k}$, of the *a priori* atmospheric state. Similar to Hoogen et al. (1999), a correlation length of 5 km is used. For the case of an atmospheric state with only ozone profile number densities, the *a priori* covariance matrix element at row i and column j is calculated as

$$(\mathbf{S}_a)_{ij} = \sigma_{a,i}\sigma_{a,j} \exp(-|z_i - z_j|/r_c), \quad (3.1)$$

where $\sigma_{a,k}$ is the standard deviation of the *a priori* profile number density at altitude z_k . In the case of an atmospheric state vector with fit parameters in addition to the profile number densities, the *a priori* covariance matrix is defined by: i) using Eq. (3.1) to calculate a smaller

a priori covariance matrix that only has the profile density elements, ii) inverting the resulting matrix, iii) padding on zeros at the rows and columns corresponding to the atmospheric state vector indices of the fit parameters, and iv) setting the diagonal elements of the zero-padded rows and columns as the inverse of the standard deviation of the corresponding fit parameter. This limits the effect of the *a priori* values of the additional parameters on the retrieval. In other words, the *a priori* values of the additional parameters will have minimal effect on changes in the atmospheric state throughout the algorithm. Moreover, the additional parameters will have maximum freedom to change at each iteration of the algorithm.

Following the retrieval algorithms of GOME (Hoogen et al., 1999) and OMI (Liu et al., 2005), the measurement covariance matrix (\mathbf{S}_y) for each retrieval of the present work is assumed to be a diagonal matrix. In other words, it is assumed that measurements over different wavelengths are not correlated. Moreover, for each measurement covariance matrix, the diagonal elements are given the same value as each other as it is assumed that there is no significant difference in error between radiance measurements at different wavelengths. As the simulated measurements do not have measurement noise, all measurement covariance matrices are arbitrarily taken as identity matrices. As the cost function (Eq. (2.28)),

$$\chi^2(\mathbf{x}) = [\mathbf{y} - \mathbf{F}(\mathbf{x})]^\top \mathbf{S}_y^{-1} [\mathbf{y} - \mathbf{F}(\mathbf{x})] + (\mathbf{x} - \mathbf{x}_a)^\top \mathbf{S}_a^{-1} (\mathbf{x} - \mathbf{x}_a), \quad (3.2)$$

is to be minimized in the optimal estimation method (see Section 2.5), the choice of the value 1 for all diagonal elements of \mathbf{S}_y does not affect the retrieval negatively; the important agent of the retrieval behaviour is the ratio between the *a priori* and measurement covariance matrix determinants. This ratio specifies the relative importance of the *a priori* atmospheric state compared to the measurement. For the present work, the relative importance of the *a priori* atmospheric state compared to the measurement is defined by scaling the *a priori* state covariance matrix by a factor. Due to the use of an *a priori* standard deviation factor and of Eq. (3.1) for the *a priori* covariance matrix, this is mathematically equivalent to scaling the *a priori* standard deviation factor. Thus, for the remainder of the discussion herein, the scaling of the *a priori* covariance matrix is defined by the *a priori* standard deviation factor.

3.2.4 GOME-Based Retrievals

In terms of fit parameters, the GOME ozone profile retrieval algorithm incorporates a shift parameter for the temperature profile and scaling factors for the aerosol number density profile, the NO₂ number density profile, the pressure profile, and the surface albedo (Hoogen et al., 1999). The GOME-based retrievals of the present work include only scaling factors for the surface albedo and the pressure profile as fit parameters. The scaling factors are taken to be relative to the true state. In other words, the true state has scaling factors of 1.0. For convenience in the SASKTRAN framework, the pressure profile is defined by setting the air number density profile. Scaling the air number density profile results in scaling both the pressure and the temperature profile, but scaling the temperature profile is not expected to significantly affect the results. The main purpose of including scaling factors for the albedo and air number density profile in the retrievals is to more easily compare to the published GOME retrieval results. In reality, compared to when the GOME retrieval was first developed, the ability to get reasonable *a priori* estimates of these quantities has greatly improved.

Similar to Hoogen et al. (1999), radiances for wavelengths between 290 and 355 nm are used for the GOME-based ozone retrieval of the present work. The spectral information for the GOME instrument model is taken from the 1B (290–314 nm) and 2B (314–355 nm) bands of GOME level 1 data, with spectral resolutions of 0.2 and 0.17 nm, respectively (Burrows et al., 1999). Data for the instrument position and look direction are also extracted from the GOME level 1 data.

The true ozone profiles used for the simulated GOME measurements are taken from retrieved OSIRIS ozone profiles and the *a priori* ozone profiles are taken from a climatological dataset by McPeters et al. (1997), both at the same time and geographic location of the GOME level 1 measurement data used to define the geometry of the simulated measurements. The true air profiles are taken from the MSIS-90 climatological model (Hedin, 1991) and the *a priori* air number density profiles are calculated by multiplying the corresponding true air profile by an arbitrary scaling factor close to 1.0, as a realistic *a priori* estimate for the air profile

is typically relatively close to the true value. Various values for the true surface albedo are tested, each being relatively close to the corresponding true values (i.e., scaling factors close to 1.0), given present day abilities to estimate the surface albedo.

3.2.4.1 Validation

A validation of the GOME-based retrieval algorithm is done by performing the retrieval for a scenario from Hoogen et al. (1999), and comparing the results to those of Hoogen et al. (1999). The chosen scenario is a typical northern midlatitude winter scenario with a SZA of 70° and a surface albedo of 0.8. To specify a SZA of 70° in SASKTRAN while also ensuring a realistic GOME retrieval scenario, GOME level 1 data, which includes the SZA for each measurement, is used. First, GOME level 1 data for a measurement in the winter of 1999 between 40°N and 50°N with a SZA close to 70° is chosen. Next, the modified Julian date (MJD), instrument position, and instrument look direction are taken from the GOME level 1 data for this measurement. Finally, the position and direction of the instrument, and the time of the measurement, are used in SASKTRAN to calculate the relative location of the Sun. The calculated Sun position is found to give a SZA at the geographic measurement location that is within 1° of the SZA in the GOME level 1 data. For example, for a sample GOME measurement on 1 January 1999, the SZA at the center of the ground pixel is 70.0° . The Sun and local zenith directions at the measurement location, calculated with SASKTRAN using the GOME level 1 measurement MJD, instrument position, and instrument direction, are found to correspond to a SZA of 69.9° .

3.2.5 OMI-Based Retrievals

The OMI ozone profile retrieval algorithm includes the following fit parameters: surface albedo, cloud fraction, scaling factors for the Ring effect, radiance/irradiance wavelength shifts, wavelength shifts between radiance and ozone cross sections, and scaling factors for the mean fitting residuals derived from one orbit of retrievals using all the other parameters (Liu et al., 2010). For simplicity, the OMI-based retrieval algorithm developed in the present work is chosen to not include any fit parameters. This allows for an easier analysis of the effect of other parameters as there is less difference between the simulated OMI measurements

and the forward model of the retrieval.

Following Liu et al. (2010), radiances for wavelengths between 270 and 310 nm are used for the OMI-based ozone retrieval of the present work. The GOME spectral information is modified for OMI based on the OMI spectral resolution of 0.5 nm (Levelt et al., 2006). Given the true GOME spectral sampling interval and resolution of approximately 0.1 nm and 0.2 nm, respectively, and the OMI spectral resolution of 0.5 nm (Levelt et al., 2006), the OMI spectral sampling interval is taken to be 0.2 nm.

The *a priori* ozone profiles of the algorithm are taken from the climatological dataset by McPeters et al. (1997), while the true ozone profiles used to simulate the OMI measurements are taken as ozone profiles retrieved from Microwave Limb Sounder (MLS) measurements. As the MLS ozone profiles do not reach down to the ground, they are extrapolated using ozone profiles from the climatological dataset by McPeters et al. (1997). This is done for each MLS profile by i) taking an ozone profile from the climatological dataset by McPeters et al. (1997) that is at the same time and coordinates as the given MLS profile, ii) scaling this climatological profile so that the number density of both the climatological profile and the MLS profile are the same at the lowest MLS profile altitude, and iii) appending the climatological profile to the MLS profile below the lowest MLS profile altitude.

3.2.5.1 Validation

A validation of the OMI-based retrieval algorithm is done by comparing retrieved ozone profiles to the true ozone profiles used to simulate the measurements, for the full sunlit portion of a simulated Aura satellite orbit. The spatial-temporal data for the Aura satellite orbit is derived from retrieved MLS ozone profile data. Because both the MLS and OMI instruments are on the Aura satellite, the geographic and time information from MLS measurements can be used to determine corresponding information for OMI. As the MLS instrument looks within the Aura satellite orbital plane in the direction of the satellite propagation, MLS measurement data is used to retrieve profiles that are at geographic locations on the Aura ground track in front of the Aura satellite. This means that at any moment when MLS is making a measurement to be used to retrieve an ozone profile, there is some finite amount

of time before Aura passes over the geographic location of said ozone profile. As OMI measures nearly straight down, realistic spatial-temporal data for OMI measurements can be determined by taking the geographic coordinates of a retrieved MLS profile, and adding some time offset to the corresponding MLS measurement time to get the time that OMI measures over the given geographic coordinates. This time offset is found to be approximately 6.9 minutes (See Appendix B).

To get the spatial-temporal OMI measurement data for the sunlit portion of an orbit, retrieved MLS ozone profile data for a single day is first taken, and the SZA at the time and geographic location of each profile is calculated. OMI and MLS measurements are made when there is sunlight on the measurement geographic location, which corresponds to times when the SZA at the measurement geographic location is less than 90° . Filtering the data to keep measurements with SZAs less than 90° results in the data being split into separate time periods, each being the sunlit portion of one Aura orbit. The sunlit portion from an orbit on 31 March 2012 is arbitrarily chosen for the OMI-based retrieval algorithm validation.

3.2.6 TEMPO-Based Retrievals

For simplicity, the TEMPO-based retrieval algorithm of the present work is based on that of GOME, which is one of the two heritage retrieval algorithms of TEMPO. The planned TEMPO retrieval algorithm uses VLIDORT for the radiative transfer modelling, which models the attenuation of the input solar radiation and the single-scatter contribution to the modeled instrument measurement with a spherical geometry while the higher-order scattering is modelled in a plane-parallel geometry (Spurr, 2006). A comparison of results using the SASKTRAN DO engine to the results using the SASKTRAN HR engine over Canada are used to help quantify the error in assuming a plane-parallel geometry for the forward model.

Following Zoogman et al. (2017), radiances over wavelength ranges 290 to 345 nm and 540 to 650 nm are used for the TEMPO-based ozone retrieval of the present work. For the TEMPO instrument model, the spectral resolution and spectral sampling interval for all wavelengths are taken as 0.57 nm and 0.2 nm, respectively, based on published TEMPO design work (Zoogman et al., 2017).

Similar to the OMI-based retrievals, the TEMPO-based retrievals vary only the ozone profile number densities and do not include additional fit parameters. The true ozone profiles used in the simulation of TEMPO measurements are taken from MLS retrieved ozone profiles and the *a priori* ozone profiles are taken as the mean of MLS profiles that are in the same month, and are within 2.5° latitude and longitude of the MLS retrieved ozone profile. This method of getting *a priori* profiles is more realistic as *a priori* profiles used in retrievals are typically taken from climatological datasets that are created by averaging a large set of retrieved profiles. The MLS profiles are extrapolated to the ground using ozone profiles from the climatological dataset by McPeters et al. (1997) in the same manner as that described for the OMI-based retrievals (see Section 3.2.5).

3.2.6.1 Statistical Analysis

A statistical analysis comparing the performance of the plane-parallel and spherical radiative transfer model engines with the TEMPO-based retrieval algorithm is done to investigate the effect of assuming a plane-parallel geometry on realistic TEMPO retrieval scenarios. The comparison is done for 48 cases: four months (March, June, September, and December), three albedos (0, 0.5, and 1), two geographic measurement locations (Los Angeles and the Canadian Oil Sands), and two local solar times (one hour past sunrise and 13:00). For each month and geographic measurement location, a set of ten true profiles are used to simulate ten TEMPO measurements. Each set of ten profiles are chosen randomly from the set of MLS retrieved profiles in the same month, and within 2.5° latitude and longitude of the geographic measurement location.

The purpose of using the two geographic measurement locations and the two local solar times is to show how the error in ignoring the curvature of the Earth and atmosphere depends on either the instrument VZA or the SZA, respectively. The two local solar times and two geographic measurement locations are each chosen to provide significant ranges of VZAs and SZAs. The reason for this being to accentuate any SZA- or VZA-dependencies in the results. Furthermore, the 13:00 local time is chosen as it is close to the local time of measurements from OMI (13:45), the instrument with a retrieval algorithm on which the TEMPO retrieval

algorithm is strongly based. The choice of the Canadian Oil Sands for one of the locations is to explore the retrieval results over a region in Canada requiring a large TEMPO VZA, and especially for a region with significant pollution emissions. The four different months and three different surface albedos allow the analysis to account for a wide range of possible conditions for TEMPO retrievals. For example, the four months encompass the two yearly equinoxes and the two yearly solstices, which correspond to both the extreme and median annual solar geometries. The three surface albedos cover the median case and the two extreme cases.

3.2.6.2 HRSSApprox Engine

As the SASKTRAN HR engine is significantly more computationally intensive than the DO engine due to the more complex geometry, the simpler spherical-geometry HRSSApprox engine is used for the TEMPO statistical analysis. The HRSSApprox engine is used for the forward model in the retrievals, but the HR engine is still used for the simulated TEMPO measurements to prevent loss of the fidelity of the simulated measurements. To achieve a maximal decrease in computation time in addition to a minimal decrease in accuracy, the wavelength subset for the HRSSApprox engine multiple-scatter contribution is chosen by including more wavelengths where the ozone absorption cross section varies the most with respect to wavelength. Fig. 3.1 shows the wavelengths used to calculate the multiple-scatter contribution exactly in the HRSSApprox engine, overlaid on a typical ozone absorption cross section. The chosen wavelength subset is taken as wavelengths from 290 to 305 nm in steps of 0.6 nm, 305 to 345 nm in steps of 0.3 nm, and 540 to 650 nm in steps of 2.4 nm. This results in a fourth as many wavelengths in the subset compared to the full set of wavelengths used for the simulated measurements, which use a spectral sampling interval of 0.2 nm for the entire wavelength range.

To ensure the accuracy is not compromised with the chosen multiple-scatter wavelength subset, results with the HRSSApprox engine for a sample of cases are compared to results with the HR engine for the same set of cases. Sun-normalized radiances for the two engines, and their percent difference, for an example case is shown in Fig. 3.2, with the radiances simulated

using a TEMPO instrument model. The Sun-normalized radiances are defined by dividing the simulated measured radiances by solar radiances, effectively cancelling any features that result purely from the Sun. In the SASKTRAN framework, the TEMPO instrument is positioned at an altitude of 35 786 km above the coordinates 0°N-100°, measuring towards the Canadian Oil Sands (57°N-112°W), with the background atmosphere and Sun set for one hour past local sunrise on 21 March 2022, and with the ozone profile set using MLS retrieval results on 21 March 2017 at 56.1°N-112.8°W. The percent difference for this case (Fig. 3.2(b)) is at most approximately 1% in magnitude, demonstrating the insignificant decrease in accuracy when using the HRSSApprox engine with the aforementioned wavelength subset compared to using the HR engine.

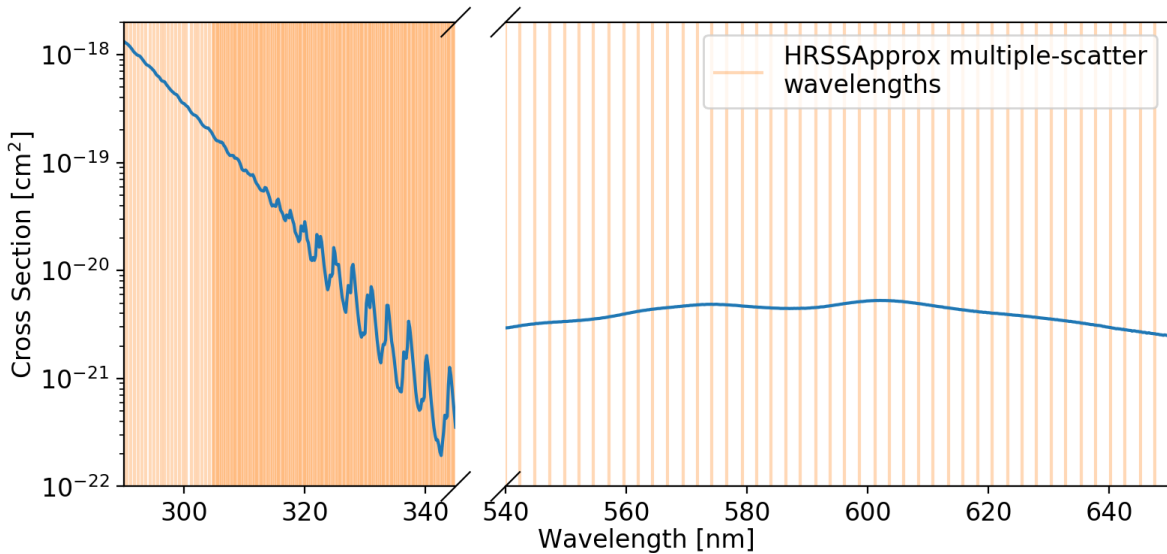
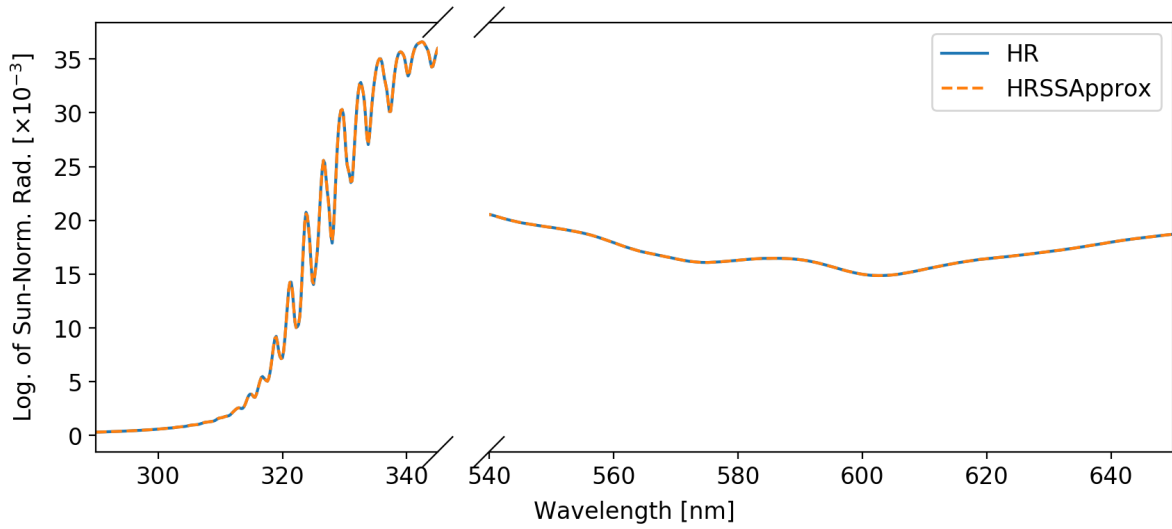
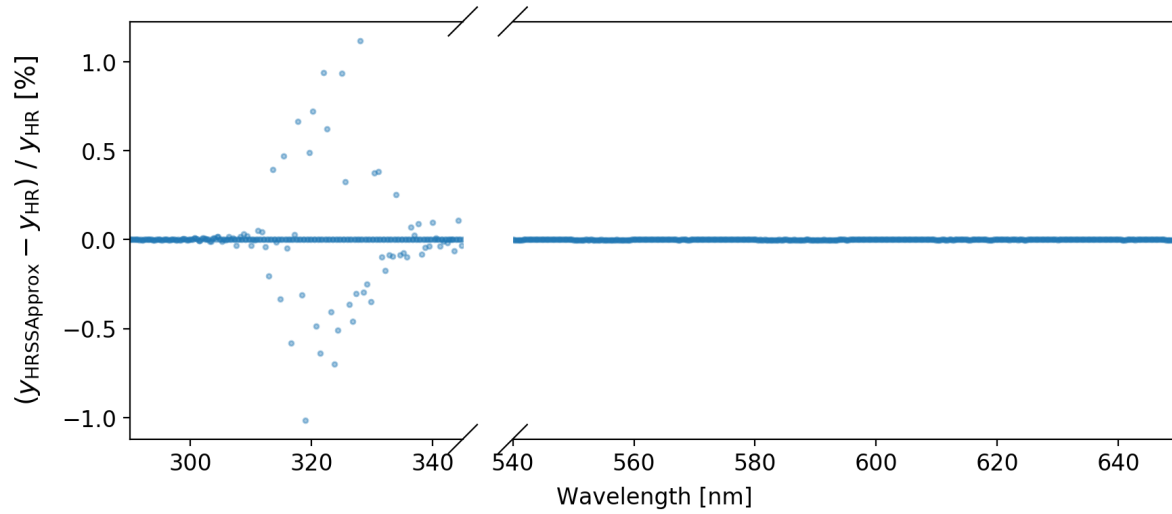


Figure 3.1. Subset of TEMPO wavelengths (vertical orange lines) used to calculate the multiple-scatter contribution exactly in the HRSSApprox engine, overlaid on the ozone cross section taken from experimentally-determined data (Brion et al., 1998; Brion et al., 1993; Daumont et al., 1992; Malicet et al., 1995) for the temperature at an altitude of 20 km above 0°N-0°E on 21 March 2008 in the MSIS-90 model (Hedin, 1991).



(a) Actual.



(b) Percent difference.

Figure 3.2. Comparison of Sun-normalized radiances between the HRSSApprox and HR engines, simulated for the TEMPO instrument positioned at an altitude of 35 786 km above 0°N-100°W, pointing towards 57°N-112°W. The background and Sun are set for one hour past local sunrise on 21 March 2022, and the ozone profile is set using MLS retrieval results on 21 March 2017 at 56.1°N-112.8°W.

3.2.6.3 Example Retrieval

The ozone profiles at each iteration of the retrieval algorithm for an example TEMPO case are shown in Fig. 3.3. The corresponding simulated measured radiances from the forward model of the retrieval are shown in Figs. 3.4 and 3.5. The example case is for TEMPO measuring towards 57°N-112°W (the Canadian Oil Sands) on 21 March 2022, with the true ozone profile taken from an MLS-retrieved profile on 22 March 2017 and with a surface albedo of 0.5. These results demonstrate how the ozone profile and forward model radiances vary as the retrieval algorithm progresses from the initial iteration (*a priori* atmospheric state) to the final iteration (retrieved atmospheric state). In Fig. 3.3, the true ozone profile (\mathbf{x}_{true}) is denoted by the dotted blue line while the true ozone profile adjusted by the averaging kernel matrix ($\mathbf{x}_{\mathbf{a}} + A[\mathbf{x}_{\text{true}} - \mathbf{x}_{\mathbf{a}}]$) is denoted by a dashed green line.

As expected, the ozone profile in Fig. 3.3 approaches the averaging-kernel-adjusted true profile ($\mathbf{x}_{\mathbf{a}} + A[\mathbf{x}_{\text{true}} - \mathbf{x}_{\mathbf{a}}]$). Note that for certain altitudes (e.g., between 12 and 16 km), the number densities of the averaging-kernel-adjusted true ozone profile are in between those of the true and *a priori* ozone profiles, but for other altitude ranges (e.g., between 19 and 22 km) the number densities of the averaging-kernel-adjusted true profile are either smaller than, or larger than, those of both the true and *a priori* profiles. This can be explained by the fact that the measurements do not have enough information to fully determine the atmospheric state. For example, the forward model radiances in Figs. 3.4 and 3.5 clearly approach those for the true atmospheric state. This implies that good agreement between the measured radiances and the forward model radiances at the final iteration can be achieved with the retrieval algorithm, but good agreement between the retrieved and true ozone profiles cannot always be achieved because of the limit in the information contained in the measured radiances.

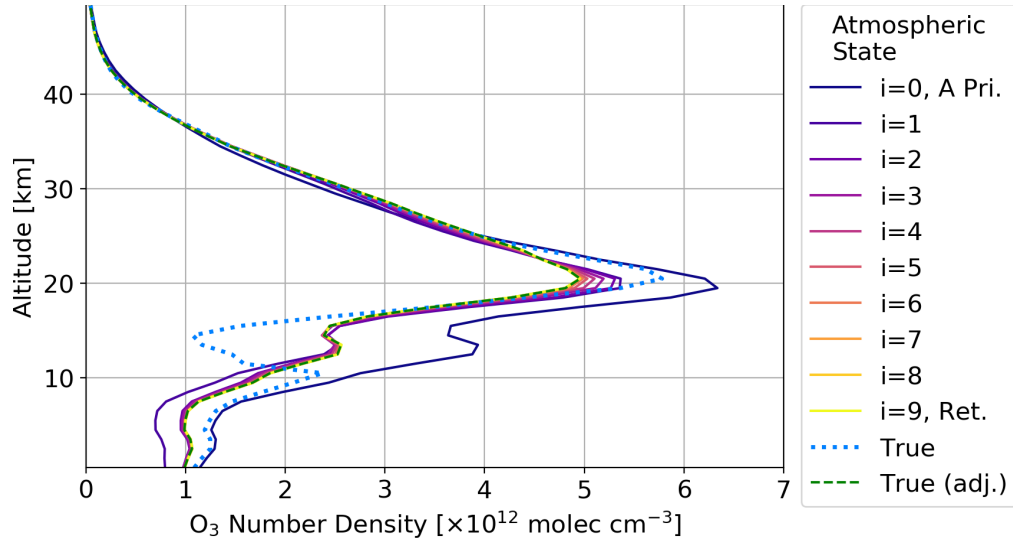


Figure 3.3. Ozone profiles for an example retrieval with a simulated TEMPO measurement over the Canadian Oil Sands (57°N - 112°W) on 21 March 2022, with the true ozone profile taken from an MLS-retrieved profile on 22 March 2017. The surface albedo is 0.5. The dotted blue line denotes the true ozone profile (\mathbf{x}_{true}) used for the simulated TEMPO measurement and the dashed green line denotes the true ozone profile adjusted by the averaging kernel matrix ($\mathbf{x}_{\mathbf{a}} + A[\mathbf{x}_{\text{true}} - \mathbf{x}_{\mathbf{a}}]$).

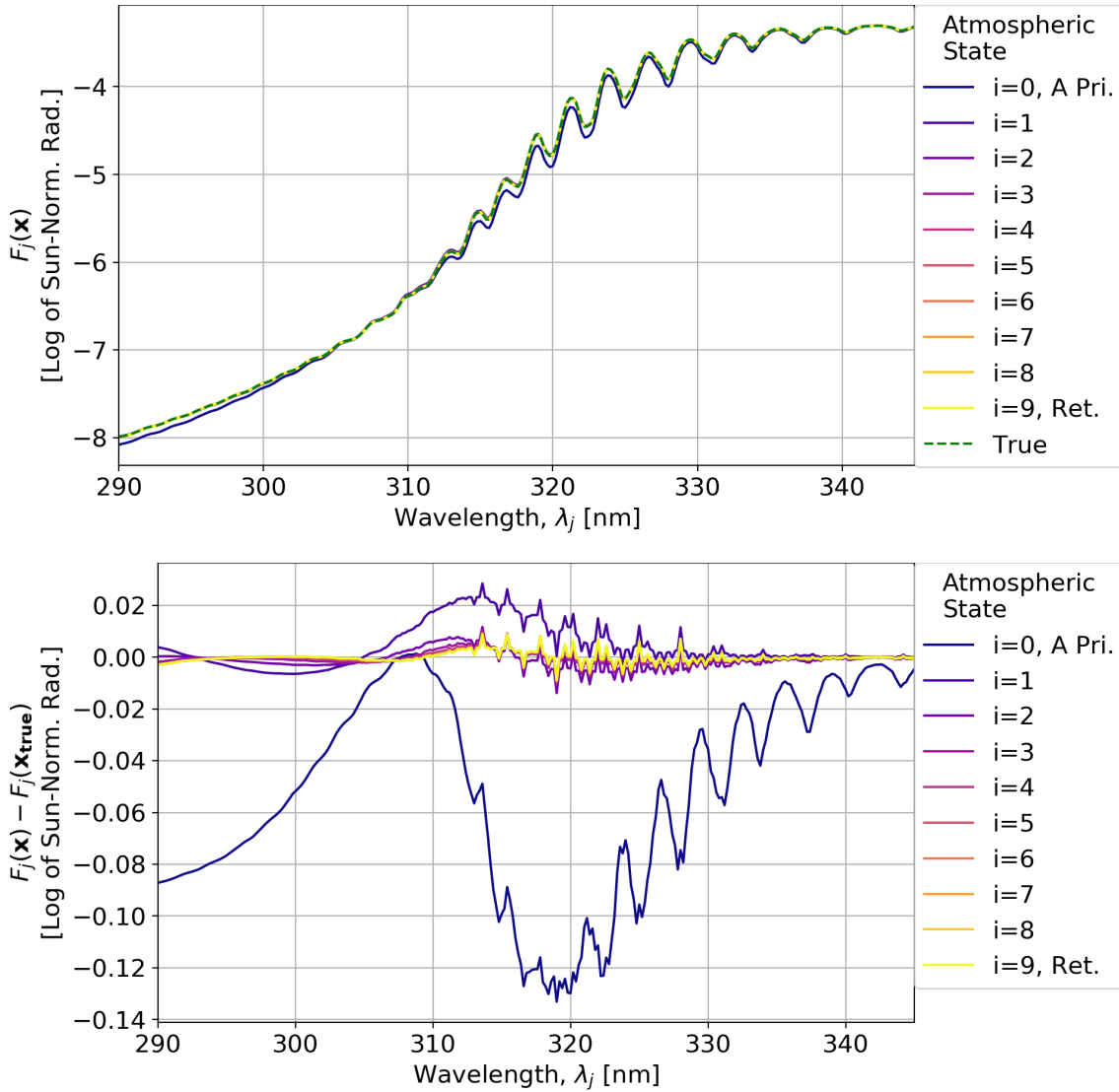


Figure 3.4. Forward model UV radiance measurements for the same example TEMPO retrieval scenario as that used for the results of Fig. 3.3. The top plot shows the log of the Sun-normalized radiances and the bottom plot shows the difference in the log of the Sun-normalized radiances relative to that for the true atmospheric state.

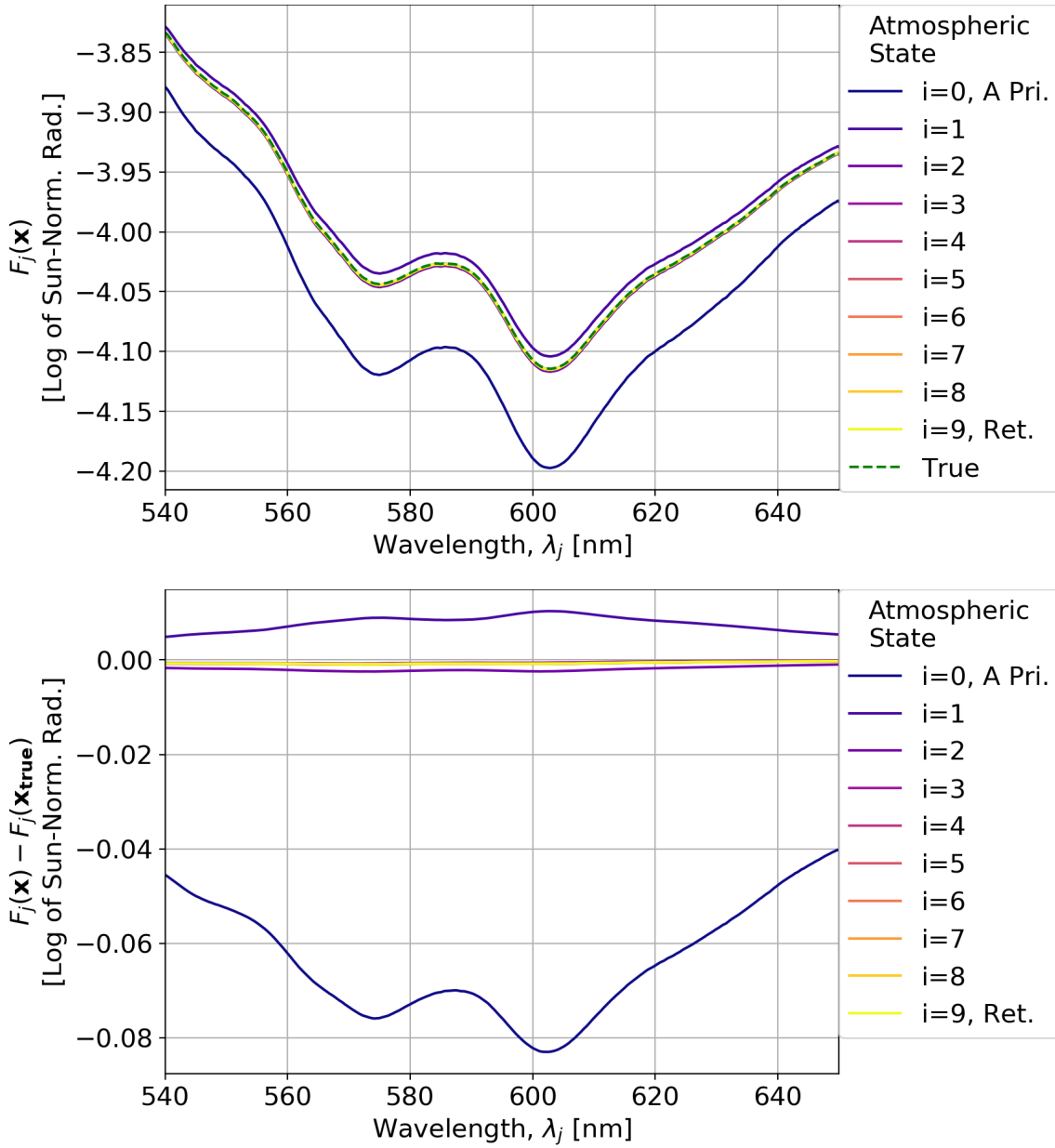


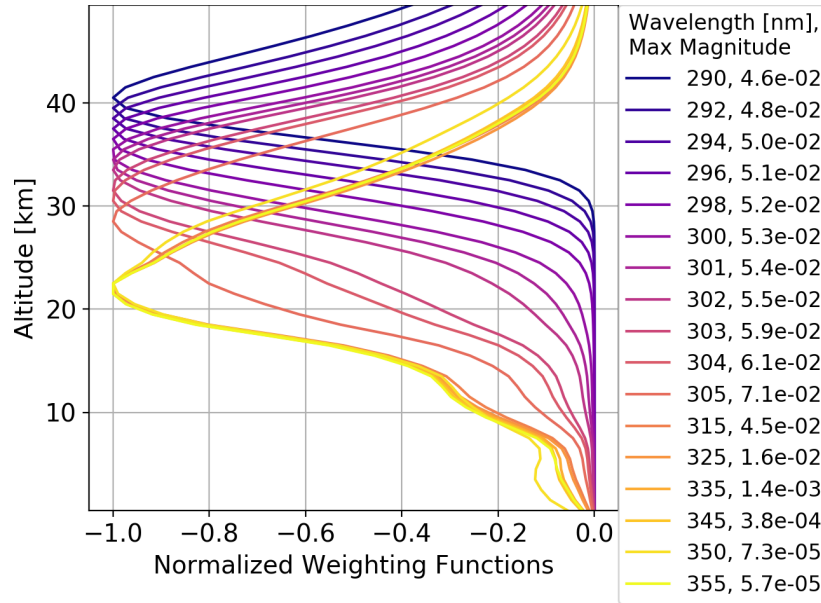
Figure 3.5. Forward model visible light radiance measurements for the same example TEMPO retrieval scenario as that used for the results of Fig. 3.3. The top plot shows the log of the Sun-normalized radiances and the bottom plot shows the difference in the log of the Sun-normalized radiances relative to that for the true atmospheric state.

3.3 Results and Discussion

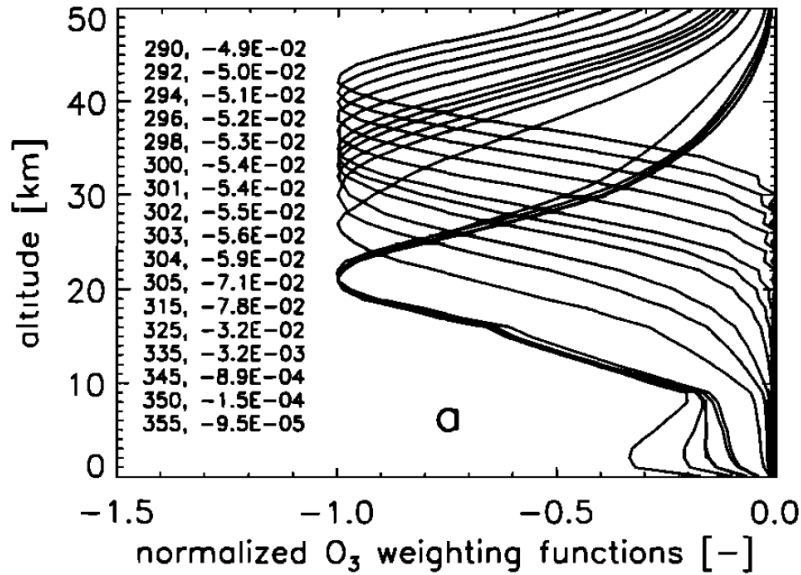
3.3.1 GOME-Based Retrievals

Fig. 3.6 compares the weighting functions (described in Section 2.5.1) resulting from the GOME-based retrieval algorithm of the present work to those of Hoogen et al. (1999) for a typical northern midlatitude winter scenario with a SZA of 70° and a surface albedo of 0.8. Each weighting function describes the dependence of the retrieved ozone profile on a given wavelength of measured radiance. The peak of a weighting function therefore corresponds to the altitude of the retrieved ozone profile that is most sensitive to the wavelength of measured radiance for which the weighting function is defined.

It can be seen from Fig. 3.6 that the altitude of the weighting function peak decreases with increasing wavelength. This can be understood by noting that the ozone cross section in Fig. 2.8 decreases with increasing wavelength from 290 to 355 nm. This means that light with a longer wavelength in this range is able to penetrate deeper in the atmosphere and therefore allow the retrieval to determine the ozone concentration lower in the atmosphere. The spread of the weighting functions from the present work (Fig. 3.6(a)) closely match that of Hoogen et al. (1999) (Fig. 3.6(b)). Compared to the results of Hoogen et al. (1999), the magnitudes of the weighting functions in the present work differ by at most 6% between 290 and 305 nm and are at most 57% lower between 315 and 355 nm. As the weighting functions are calculated by the radiative transfer model, these results imply a good match in the radiative transfer model, as well as in the atmospheric state and the model input settings.



(a) Results of the present work for 1 Jan. 1999 at 55°N. The *a priori* air density profile factor and albedo are 0.95 and 0.5, respectively.



(b) Plot reproduced from Fig. 1(a) of Hoogen et al. (1999); a typical northern midlatitude winter scenario.

Figure 3.6. Comparison of the GOME-based ozone retrieval algorithm weighting functions from the present work to those of Hoogen et al. (1999), for a typical northern midlatitude winter scenario, solar zenith angle of 70°, and surface albedo 0.8.

Fig. 3.7 and Fig. 3.8 show the effect of varying the standard deviation of the *a priori* atmospheric state on the GOME-based retrievals for the same scenario as in Fig. 3.6. Fig. 3.7 shows the effect on the averaging kernels and Fig. 3.8 shows the effect on the retrieved ozone profiles. Note that the standard deviation of the *a priori* atmospheric state affects the retrieval through the *a priori* covariance matrix (\mathbf{S}_a), defined in Eq. (3.1). Each averaging kernel describes how sensitive the retrieved ozone profile is to the true ozone profile density at an altitude denoted by “nominal” in the legend of Fig. 3.7. The term “nominal” is used as the averaging kernel peak is expected to be near this altitude. The actual altitude of the peak of each averaging kernel is denoted by “true” in the legend of Fig. 3.7. For example, the yellow averaging kernel line in Fig. 3.7(c) shows that the true profile number density at 45.5 km has the strongest effect on the retrieved profile at 42.5 km, the peak of the averaging kernel. The dotted blue lines in Fig. 3.8 show the true ozone profile, \mathbf{x}_{true} , while the dashed green line shows the true ozone profile adjusted by the averaging kernel matrix, $\mathbf{x}_a + \mathbf{A}(\mathbf{x}_{\text{true}} - \mathbf{x}_a)$.

In Fig. 3.7, the altitude of the peak of each averaging kernel approaches the respective nominal value as the standard deviation factor increases. This can be explained by noting that the averaging kernel matrix is defined in Eq. (2.36) as

$$\mathbf{A} = (\mathbf{K}^\top \mathbf{S}_y^{-1} \mathbf{K} + \mathbf{S}_a^{-1})^{-1} \mathbf{K}^\top \mathbf{S}_y^{-1} \mathbf{K}. \quad (3.3)$$

From Eq. (3.3), scaling the *a priori* covariance matrix (Eq. (3.1)), equivalent to scaling the *a priori* standard deviation factor, causes the averaging kernel matrix to approach an identity matrix, and hence the altitude of the peak of each averaging kernel to approach the respective nominal value. The averaging kernels can also be seen to closely match those in Fig. 3 of Hoogen et al. (1999), implying a good replication of the retrieval algorithm. In Fig. 3.8, the number density at the peak of the retrieved ozone profile increases and approaches that of the true profile up until the *a priori* standard deviation factor is approximately ten, at which point the number density of the retrieved profile peak lowers again and the retrieved profile gets further from the true profile in the altitude range 10–20 km. This can be understood to be the point where the limit has been reached in the amount of information extracted from the simulated measurement to determine the profile in this altitude range. This region (10

to 20 km in altitude) is the most difficult to retrieve as it is near or below the ozone peak, resulting in significantly less UV light being able to penetrate down to these altitudes and then get scattered and reflected up to the instrument to be measured.

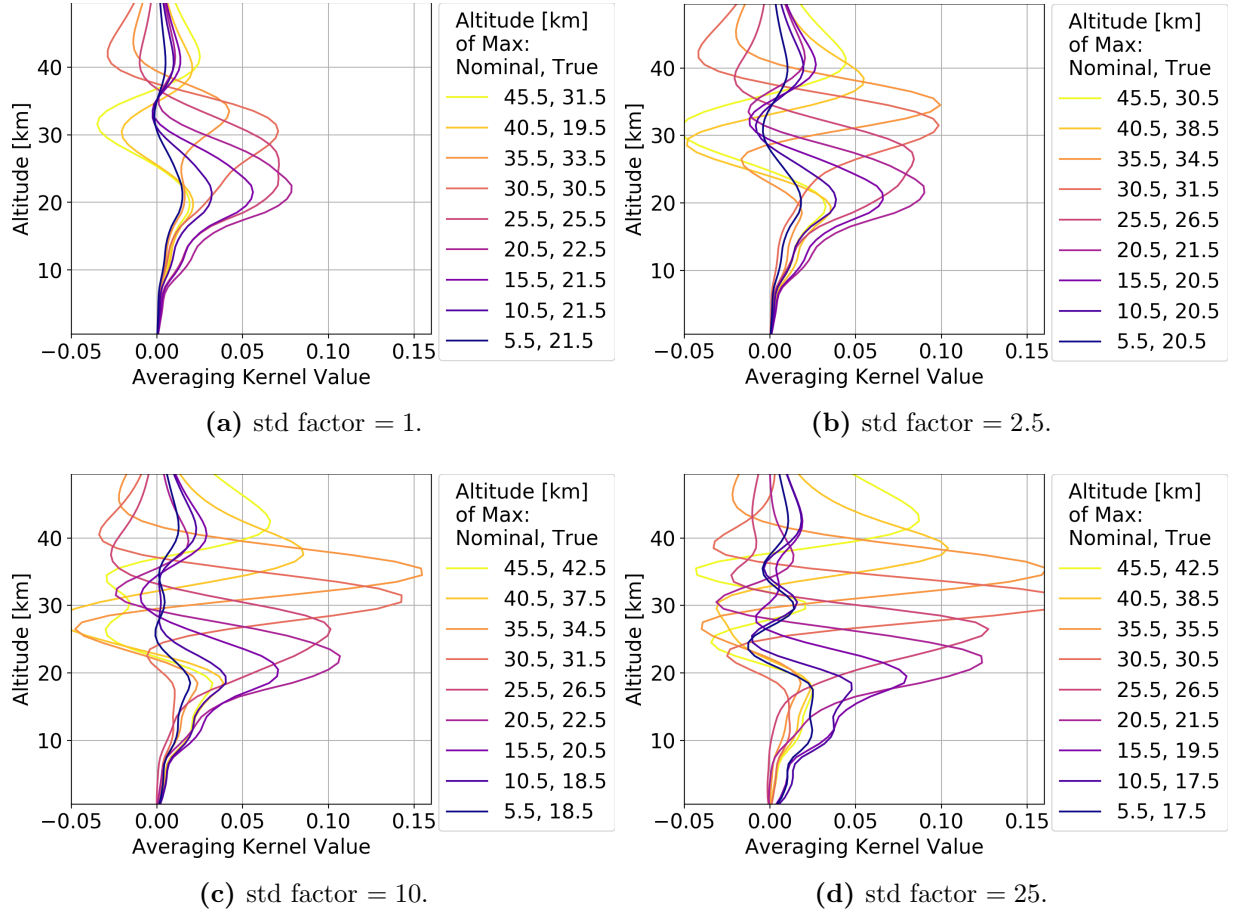


Figure 3.7. Effect of varying the *a priori* standard deviation (std) factor (ratio of the standard deviation to the mean for the *a priori* number density) on the GOME-based ozone retrieval averaging kernels for the same scenario as Fig. 3.6. The nominal altitude is the altitude of the true ozone profile on which the retrieved profile is dependent. The true altitude is the altitude of the peak of the averaging kernel.

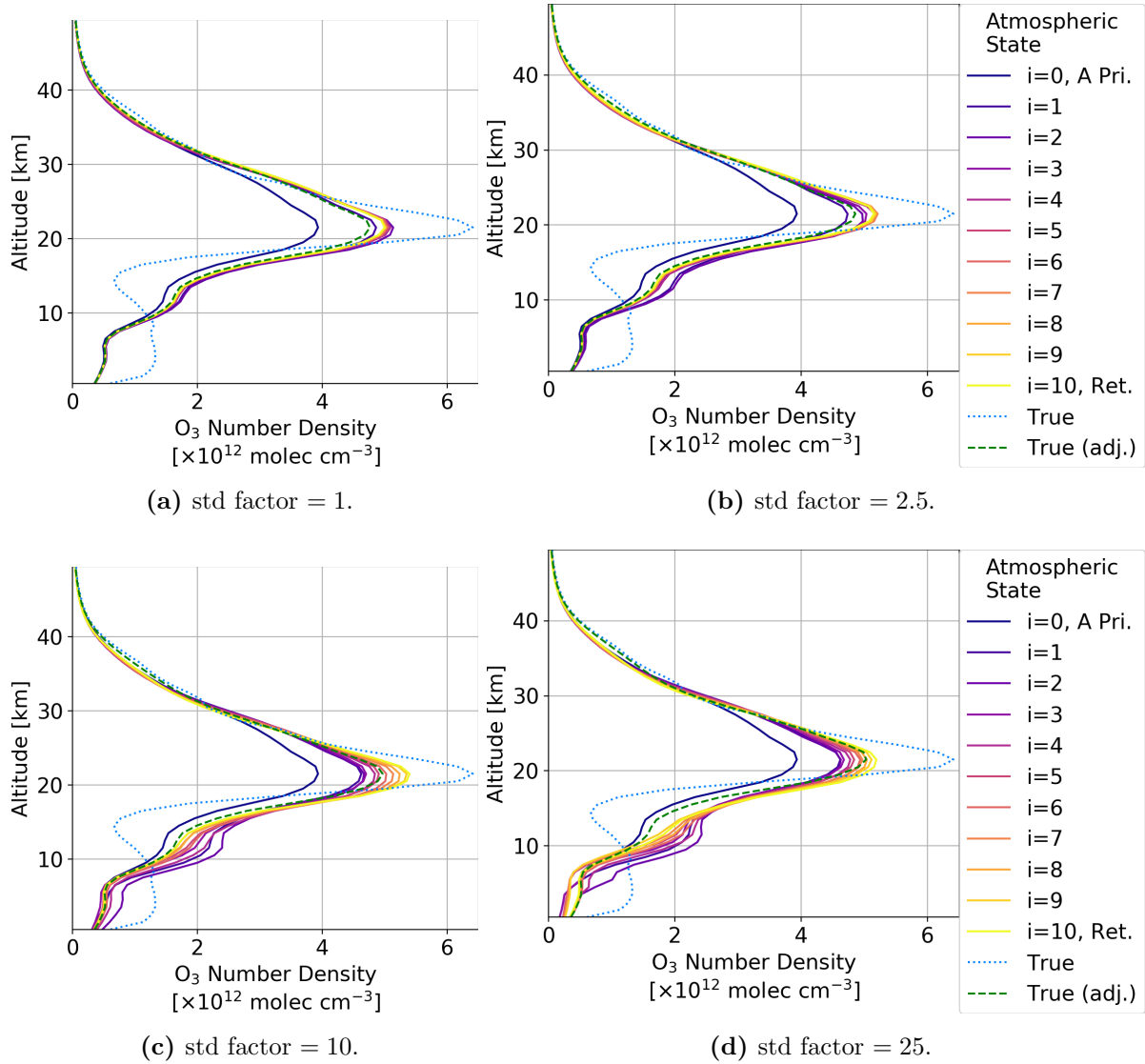


Figure 3.8. Effect of varying the *a priori* standard deviation (std) factor (ratio of the standard deviation to the mean for the *a priori* number density) on the GOME-based ozone retrieval, for the same cases as Fig. 3.7. The dotted blue line is the true ozone profile (\mathbf{x}_{true}) used for the simulated instrument measurement and the dashed green line is the true ozone profile adjusted by the averaging kernel matrix ($\mathbf{x}_{\mathbf{a}} + A[\mathbf{x}_{\text{true}} - \mathbf{x}_{\mathbf{a}}]$).

3.3.2 OMI-Based Retrievals

For the OMI-based retrieval algorithm of the present work, Fig. 3.9 shows the percent error of retrieved ozone profiles relative to the true profiles for a full terminator-to-terminator path

of the Aura satellite, simulated for 31 March 2012, where a terminator is the line separating the dark and sunlit portions of the Earth. As expected, the average absolute difference between the retrieved and true profiles (top row of plots in Fig. 3.9) is lower for the larger *a priori* standard deviation factor. Comparing the retrieved profiles to the true profiles adjusted by the averaging kernel matrix ($\mathbf{x}_a + A[\mathbf{x}_{\text{true}} - \mathbf{x}_a]$) in the bottom row of plots in Fig. 3.9, the lower *a priori* standard deviation factor shows a lower average deviation below 20 km and above 50 km. This implies that it is more difficult for the profile in the retrieval to approach the averaging-kernel-adjusted true profile as the *a priori* standard deviation increases. Furthermore, from the number of sign changes in the relative difference between the retrieved and the averaging-kernel-adjusted true profiles (bottom row of Fig. 3.9), the retrieval is somewhat more sporadic for a higher *a priori* standard deviation.

Overall, the magnitude of the relative difference between the retrieved and true profiles is below roughly 25% for an *a priori* standard deviation factor of 10. The results of the OMI-based retrievals in the present section and of the GOME-based retrievals in Section 3.3.1 are sufficiently satisfactory to warrant the application of similar methods to a TEMPO-based algorithm in the following section.

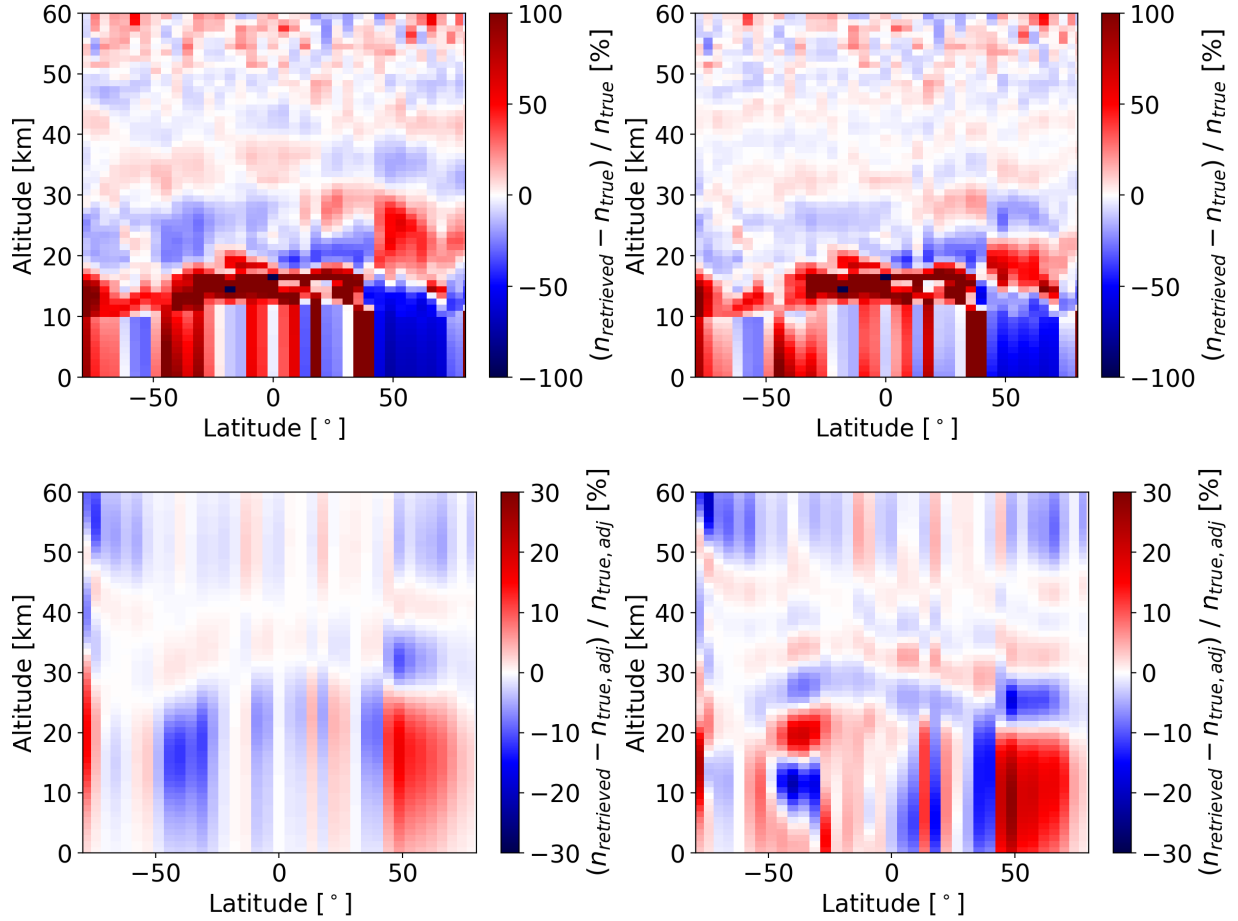
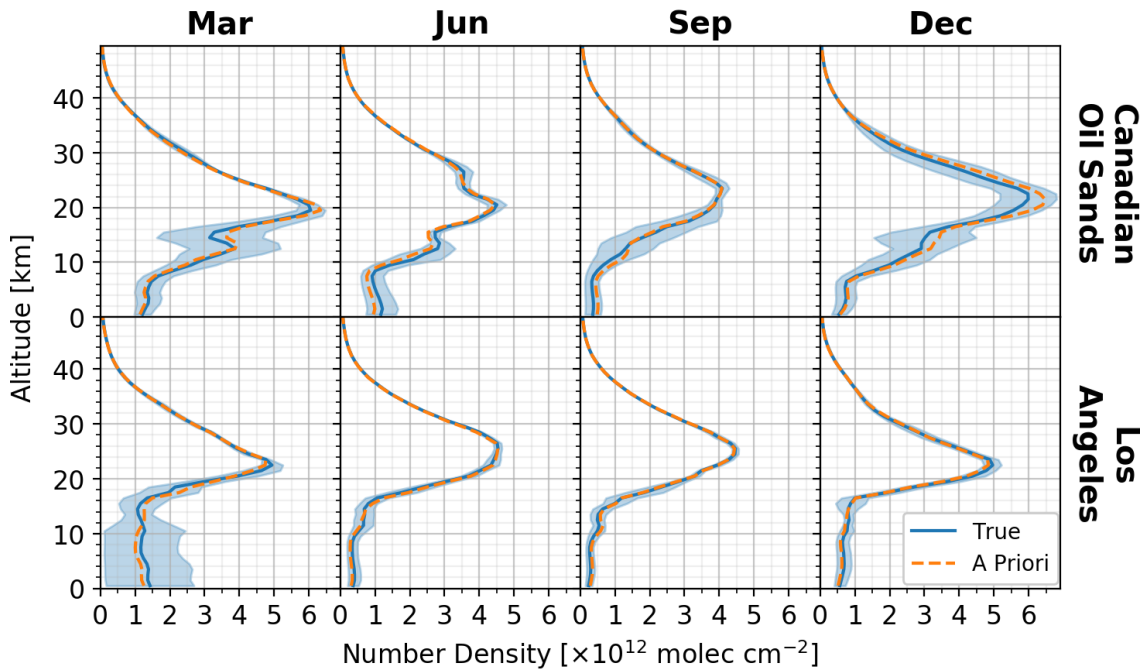


Figure 3.9. Percent error of OMI-based retrieval number densities ($(n_{retrieved} - n_{true})/n_{true}$) for a path from one terminator (at 78°S) to the other (at 81°N) of an Aura satellite orbit on 31 March 2012. The top row of plots compares to the true profiles (\mathbf{x}_{true}) and the bottom row of plots compares to the true profiles adjusted by the averaging kernel matrix ($\mathbf{x}_a + A[\mathbf{x}_{true} - \mathbf{x}_a]$). The *a priori* profile standard deviation is 1.5 times the *a priori* profile in the first column of plots and 10 times the *a priori* profile in the second column of plots.

3.3.3 TEMPO-Based Retrievals

Fig. 3.10 shows the *a priori* ozone profiles and the mean and standard deviation (shaded region) of the set of ten true ozone profiles, used for each month and geographic location of the TEMPO-based retrieval statistical analysis. Figs. 3.11 and 3.12 show the mean and

standard deviation of the retrieved profiles for each case, while Figs. 3.13 and 3.14 show the mean and standard deviation of the difference between the retrieved and the true profile for each case. Figs. 3.11 and 3.13 correspond to 13:00 local solar time and Figs. 3.12 and 3.14 correspond to one hour past local sunrise. In each case, the *a priori* standard deviation factor is taken as 4.0. That is, the standard deviation of the *a priori* ozone number density profile is taken as 4.0 times the *a priori* ozone number density profile. This in turn affects the *a priori* covariance matrix of the retrieval according to Eq. (3.1). The value of 4.0 is chosen based on trial-and-error on a subset of cases to ensure reasonable behaviour of the retrievals, similar to the analysis of the effect of the *a priori* standard deviation factor on the averaging kernels and retrieved profiles in Figs. 3.7 and 3.8 for the GOME-based retrievals.



(a) Los Angeles, 34°N-118°W.

Figure 3.10. TEMPO-based retrievals: *a priori* ozone profiles and the mean and standard deviation (shaded region) of the true ozone profiles for the statistical analysis.

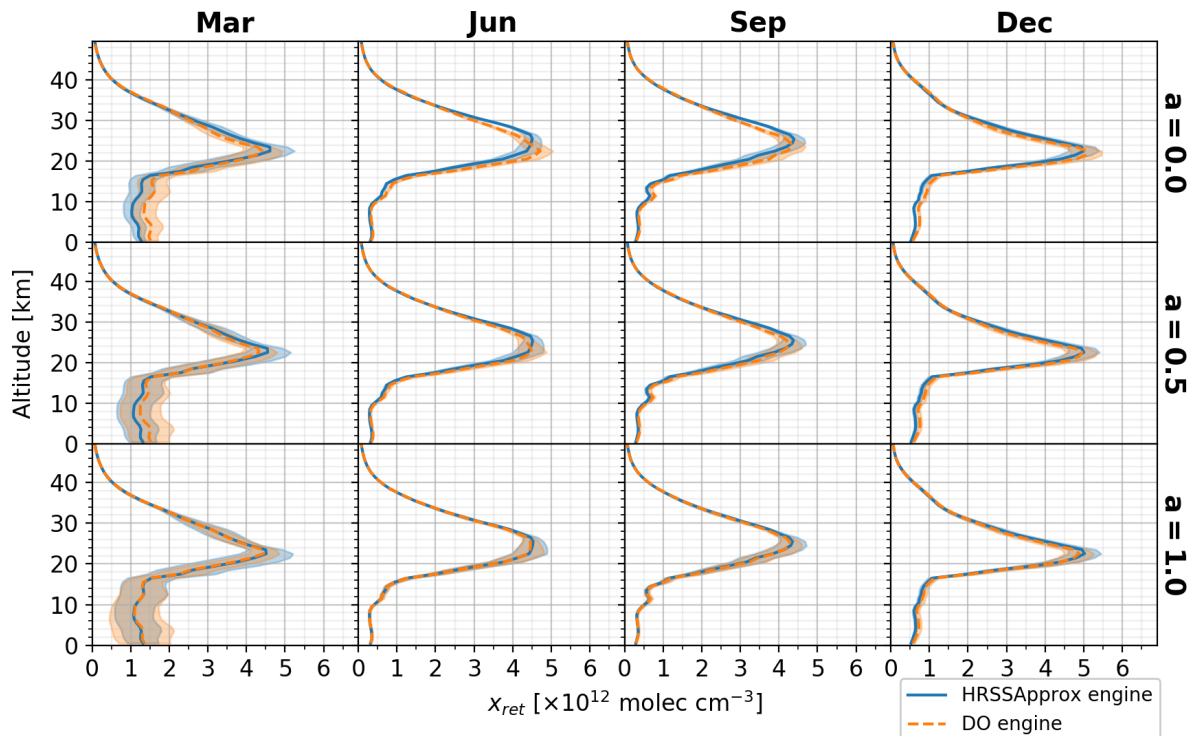
Comparing corresponding plots between Fig. 3.11 and Fig. 3.12 indicates that the lower Sun position, or higher SZA, tends to raise the altitude of the DO-engine retrieved profile peak and decrease the magnitude of the profile peak, with the largest effect being over the Canadian Oil Sands in June and December. This effect can alternatively be viewed as the retrieved profiles performing as well or better above the ozone peak but worse near or below the peak.

The fact that this effect is not seen in the results for the HRSSApprox engine indicates that the HRSSApprox engine may be preferred over the DO engine for high SZAs in June and December when measuring over the Canadian Oil Sands. For example, the retrieved profiles for the DO engine over the Canadian Oil Sands in December have at most approximately four times more absolute retrieval error when measured one hour past local sunrise (Fig. 3.14(b)) compared to being measured at 13:00 local time (Fig. 3.13(b)). The effect, even for the DO engine, is not significant when measuring with a lower VZA (i.e., over Los Angeles).

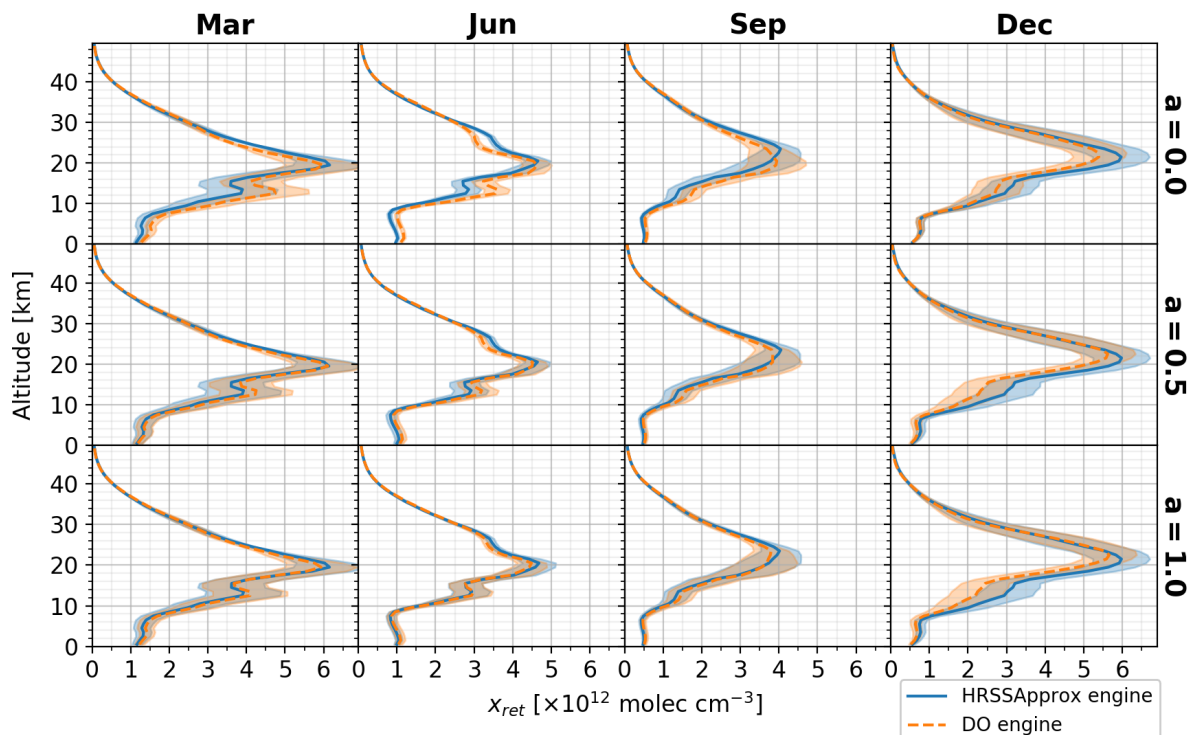
For the retrieved profile results in both Fig. 3.11 and Fig. 3.12, there is more error for the DO engine compared with the HRSSApprox engine when the instrument is looking over the Canadian Oil Sands (higher VZA) than there is when looking over Los Angeles. For example, the absolute difference in retrieval error between the DO and HRSSApprox engines is at most approximately six times larger for the Canadian Oil Sands (Fig. 3.14(b)) compared to that for Los Angeles (Fig. 3.14(a)) one hour past local sunrise, or at most approximately two times larger for the Canadian Oil Sands (Fig. 3.13(b)) compared to that for Los Angeles (Fig. 3.13(a)) at 13:00 local time.

The two aforementioned dependencies of the retrievals (on SZA and VZA) can be explained by the fact that larger SZAs and VZAs result in larger differences between the two engines in terms of the paths of modeled photons through the atmosphere from the Sun to the instrument. In other words, accounting for the curvature of the Earth and the atmosphere is more important for highly oblique SZAs and VZAs. In contrast to GOME and OMI measurements, highly oblique SZAs and VZAs are regularly present for TEMPO measurements. For example, these occur for TEMPO when measuring over Canada or measuring near local sunrise or sunset.

The insignificant errors for measurements of Los Angeles at either local solar time demonstrates that the radiative transfer model for the future TEMPO ozone retrievals may have been chosen because, despite geometry assumptions, it has an insignificant effect on the retrievals over the majority of the field of regard. This highlights the possible benefits for Canada in using a more realistic geometry for TEMPO ozone retrievals over Canada.

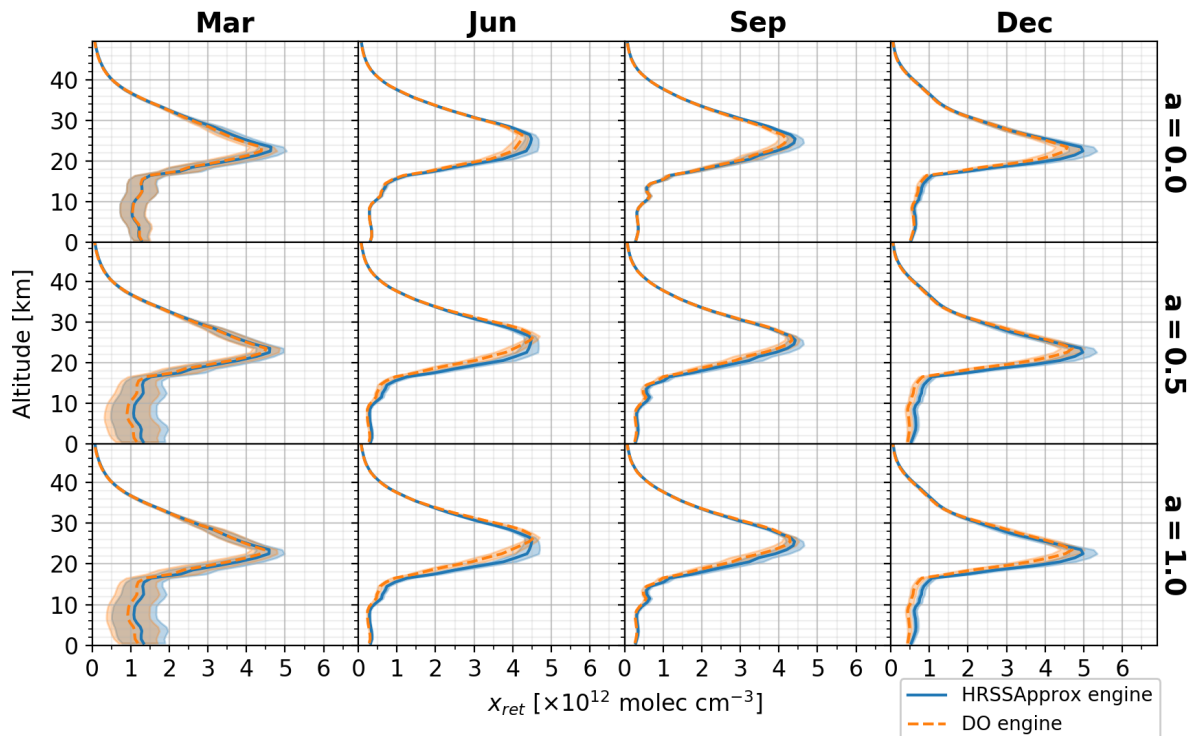


(a) Los Angeles, 34°N-118°W.

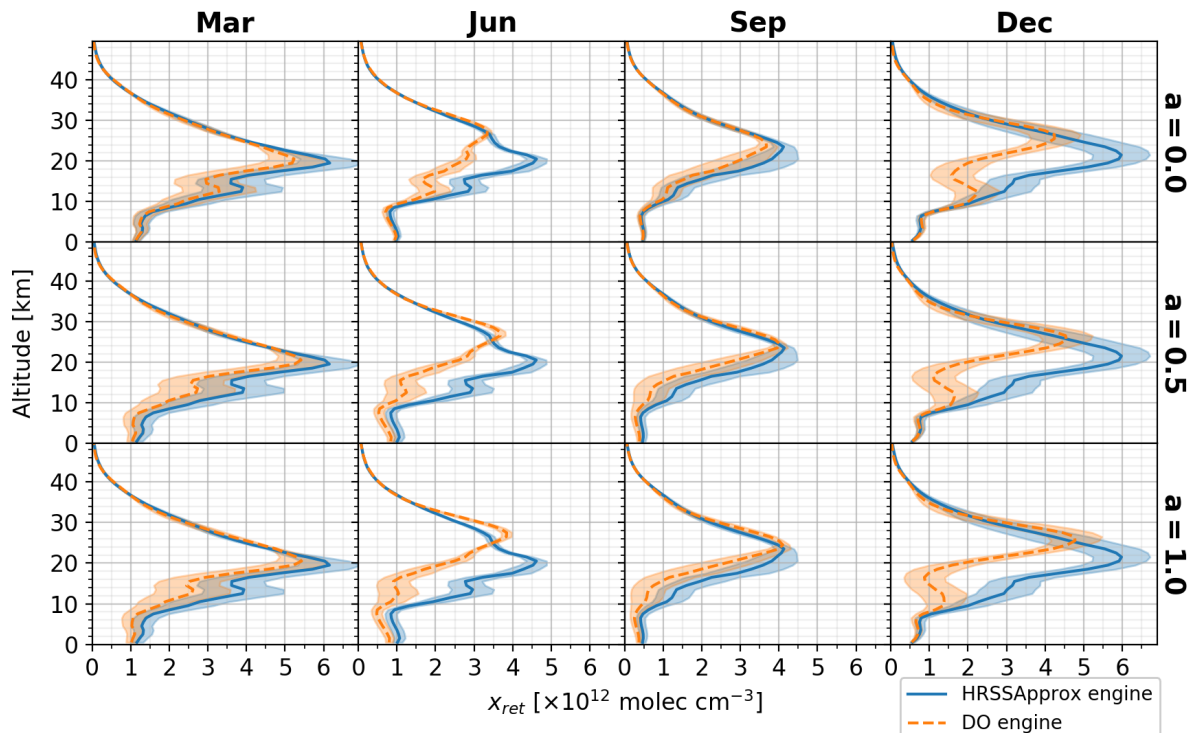


(b) Canadian Oil Sands, 57°N-112°W.

Figure 3.11. TEMPO-based retrievals: Mean and standard deviation (shaded region) of the retrieved ozone profile at 13:00 local time.

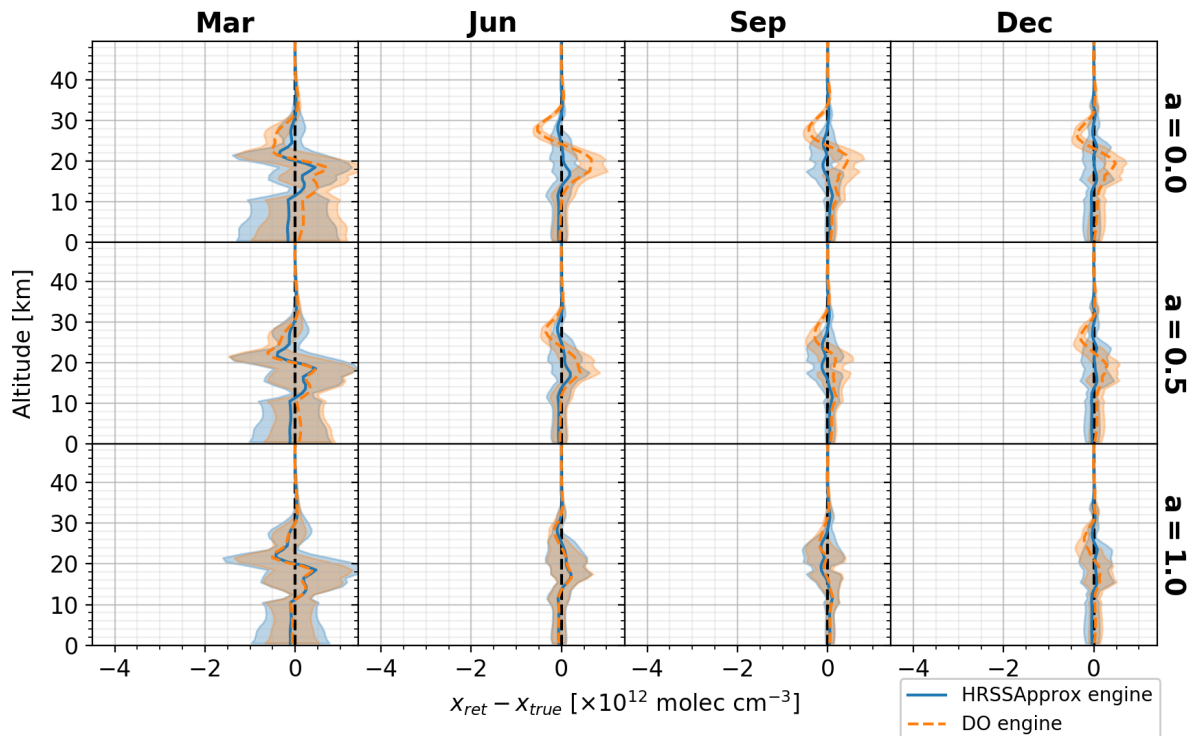


(a) Los Angeles, 34°N-118°W.

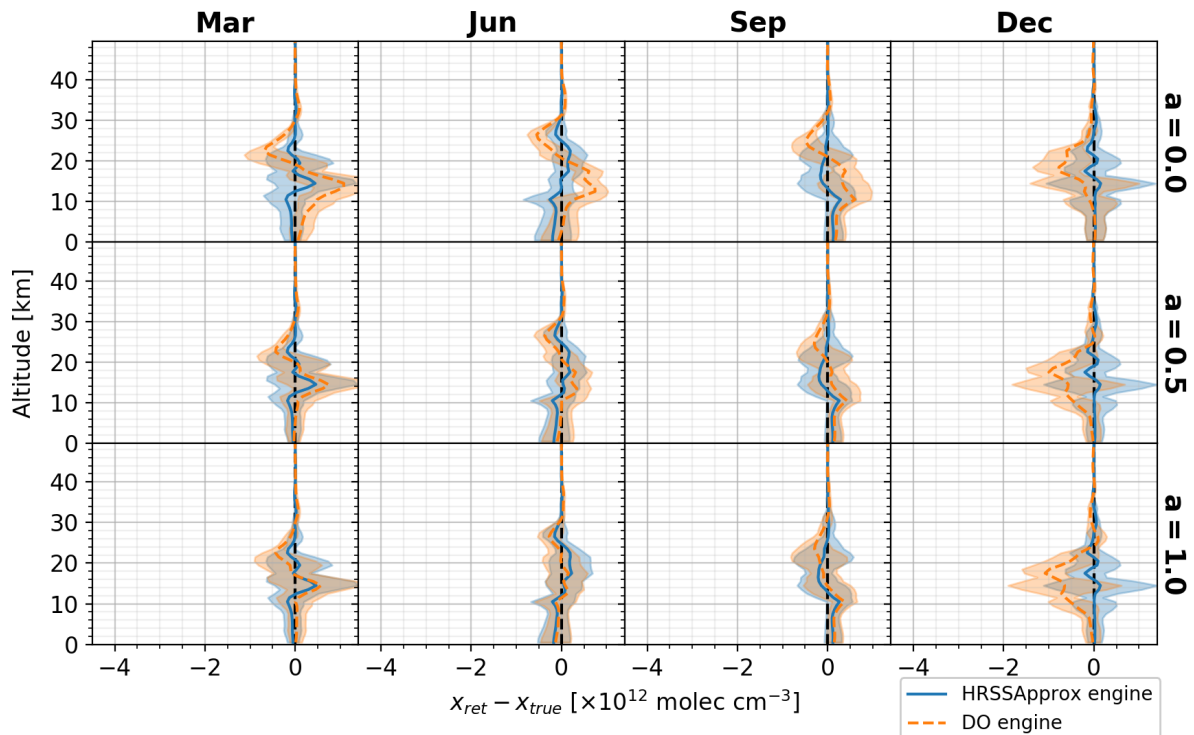


(b) Canadian Oil Sands, 57°N-112°W.

Figure 3.12. TEMPO-based retrievals: Mean and standard deviation (shaded region) of the retrieved ozone profile at one hour past local sunrise.

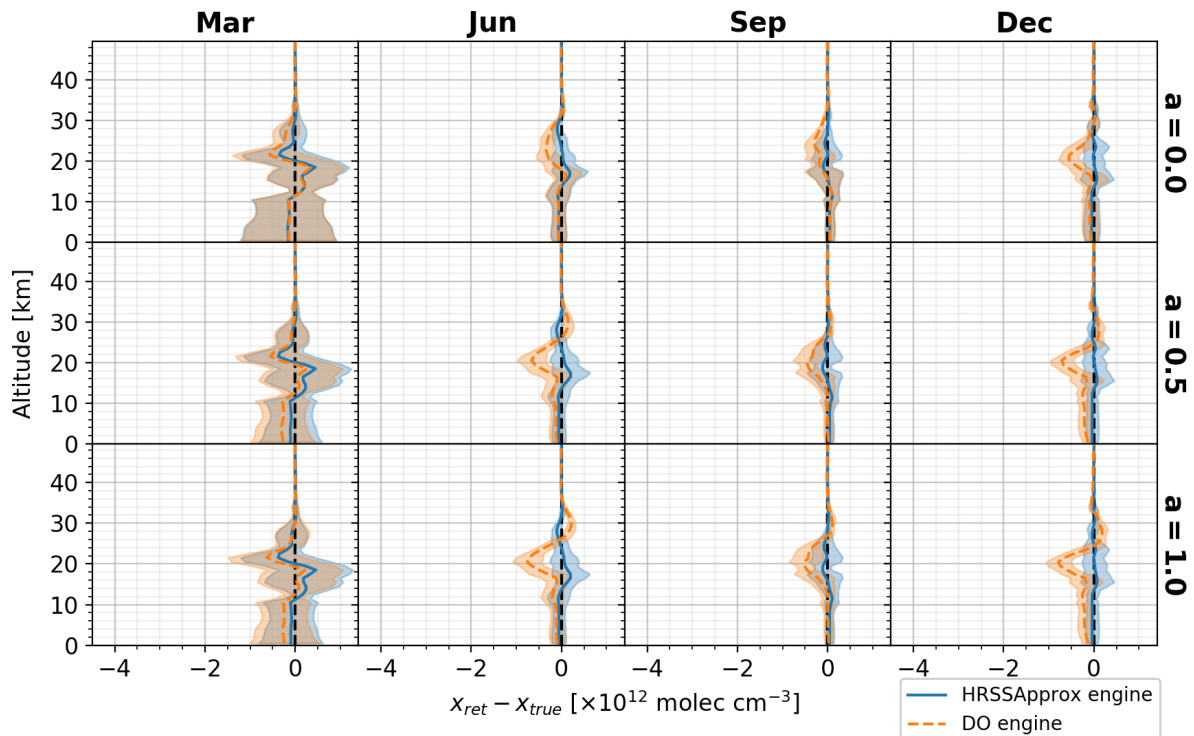


(a) Los Angeles, 34°N-118°W.

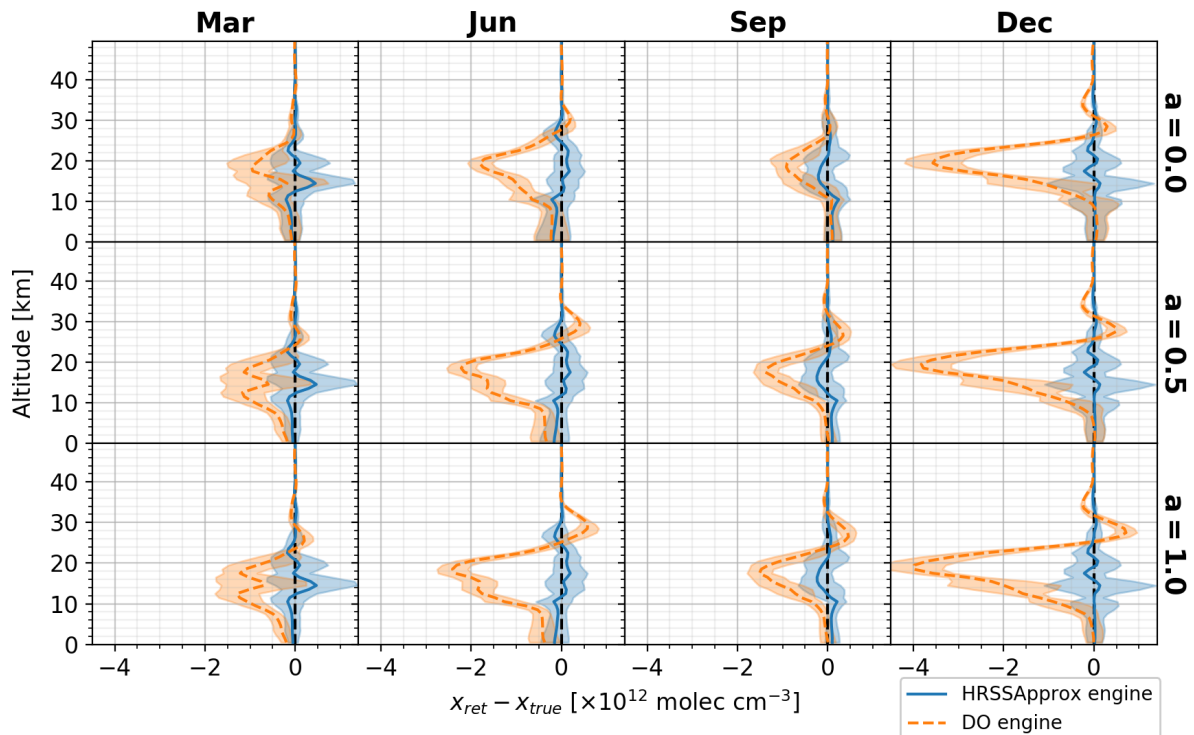


(b) Canadian Oil Sands, 57°N-112°W.

Figure 3.13. TEMPO-based retrievals: Mean and standard deviation (shaded region) of the error in the retrieved ozone profile at 13:00 local time.



(a) Los Angeles, 34°N-118°W.



(b) Canadian Oil Sands, 57°N-112°W.

Figure 3.14. TEMPO-based retrievals: Mean and standard deviation (shaded region) of the error in the retrieved ozone profile at one hour past local sunrise.

3.4 Conclusion

A TEMPO-based tropospheric ozone retrieval algorithm, based on validated GOME- and OMI-based retrieval algorithms (Sections 3.3.1 and 3.3.2), is used to investigate the potential reductions in ozone retrieval error due to the use of a radiative transfer model with a more realistic Earth-atmosphere geometry for tropospheric ozone retrievals over Canada using simulated TEMPO measurements. Overall, there is more error in the retrieved profiles at altitudes at or below the ozone peak. This can be explained by the fact that only a relatively small fraction of solar radiation can reach down below the ozone peak and be reflected and refracted up to the instrument to give information about the profile. It is shown that, when measuring tropospheric ozone over the Canadian Oil Sands one hour past local sunrise (Fig. 3.14(b)), the retrieval error near the ozone profile peak for the DO engine can reach approximately 80% in December, 50% in June, and 25% in September or March, while the corresponding error for the HRSSApprox engine is an order of magnitude smaller. For a local time of 13:00, the Canadian Oil Sands retrieval error (Fig. 3.13(b)) near the ozone profile peak for the DO engine can reach as much as approximately 15%, while the HRSSApprox engine retrieval error is roughly the same as the HRSSApprox engine retrieval error over the Canadian Oil Sands one hour past local sunrise (Fig. 3.14(b)).

In general, there is larger retrieval error over the Canadian Oil Sands compared to over Los Angeles, especially near sunrise. Compared to its predecessors GOME and OMI, the TEMPO instrument regularly encounters these conditions of high SZAs and VZAs, and in particular when retrieving profiles over Canada. For these reasons, it is recommended to use a radiative transfer engine that assumes a curved atmosphere-Earth geometry, such as the SASKTRAN HR engine, to take advantage of TEMPO measurements for the purpose of monitoring tropospheric ozone pollution over Canada.

Nonetheless, future work is required to determine the effects of measurement noise on the retrievals and to analyze the relative importance of atmosphere-Earth geometry assumptions on different orders of light scattering. This would allow for a more realistic analysis of the difference in retrieval error between the planned VLIDORT-based retrieval algorithm and a

retrieval algorithm with a radiative transfer model model like the SASKTRAN HR engine, and therefore a better understanding of the most suitable choice of a radiative transfer model for future Canadian tropospheric ozone retrievals with TEMPO measurements. If possible, results with a radiative transfer model like the SASKTRAN HR engine could be compared to results with the actual VLIDORT software for the most thorough assessment.

4 Assessment of Non-Coincident Limb-Nadir Matching for Measuring Tropospheric Nitrogen Dioxide

4.1 Introduction

The goal of the work in the present chapter is to further assess the relatively novel method by Adams et al. (2016), described in Section 2.6, of estimating tropospheric NO₂ column densities by matching the stratospheric NO₂ column densities measured by a limb-viewing instrument to the combined troposphere-stratosphere NO₂ column densities measured by a nadir-viewing instrument and then subtracting the stratospheric column densities from the combined troposphere-stratosphere column densities. The advantage of this method of estimating tropospheric concentrations from the nadir-viewing instrument measurements is that, unlike conventional methods that rely on modelling and on assumptions about the atmosphere, this method takes advantage of highly-validated limb-viewing remote sensing instrument measurements. Thus, if this method is proven to be effective then it is arguably more accurate than conventional methods.

The objective of assessing the non-coincident limb-nadir matching method of estimating tropospheric NO₂ densities is pursued by reanalyzing the OSIRIS-OMI results of Adams et al. (2016) with newer OSIRIS, OMI, and photochemical box model datasets, and by analyzing OSIRIS-TROPOMI results. The methodology for this is detailed in Section 4.2. The process of undertaking this goal has led to the OSIRIS NO₂ profile retrieval algorithm being updated, resulting in a better match with the heritage, validated OSIRIS version 3 NO₂ profile data. The results leading to the development of the updated OSIRIS NO₂ retrieval algorithm, results of the OSIRIS-OMI limb-nadir matching reanalysis, and results

of the OSIRIS-TROPOMI limb-nadir matching analysis are covered in Section 4.3, with their meaning and significance explored in Section 4.4. Finally, Section 4.5 concludes the work and outlines the future research that would help further the goal of assessing the non-coincident limb-nadir matching technique.

4.2 Methodology

A non-coincident limb-nadir matching algorithm based on that by Adams et al. (2016) is developed for the present work in Python. The code is written to accommodate OMI-SP version 4 or TROPOMI version 1.3 NO₂ VCD data and OSIRIS version 3, 6, or 7 NO₂ vertical density profile data. Although the OMI-SP NO₂ version 2 data is no longer publicly available, the code also accommodates the use of a sample of the bias-corrected version 2 data for 3-5 March 2008 that was used by Adams et al. (2016) and is provided by Dr. Adams for the present analysis. This allows for the analysis of differences due to the data versions. Both the reanalysis with newer NO₂ data products and the analysis with OSIRIS-TROPOMI limb-nadir matching serve to better understand the potential value in the non-coincident limb-nadir matching method for estimating tropospheric NO₂ pollution densities. Furthermore, the coverage overlap between the three instruments, OSIRIS, OMI, and TROPOMI, as well as the difference in ascending node local times of only approximately 15 minutes between OMI and TROPOMI, allows for the OSIRIS-OMI and OSIRIS-TROPOMI matching results to be compared to each other.

Similar to the work by Adams et al. (2016), only OSIRIS data from the descending node is used. This is to avoid a systematic bias between the ascending and descending nodes due to NO₂ diurnal variations resulting from the two nodes being measured at different local solar times. Furthermore, OSIRIS data is only used for SZAs less than 88° to minimize the diurnal effect, also known as photochemical enhancement (Hendrick et al., 2006; McLinden et al., 2006). The tropopause altitudes used to define the bottom of the stratospheric profiles are calculated using the lapse rates from the National Centres for Environmental Prediction reanalysis data (Kalnay et al., 1996).

Data resulting from the photochemical box model (Prather & Jaffe, 1990) used by Adams et al. (2016) is used in the present work to extrapolate the OSIRIS NO₂ density profiles in time and altitude. The photochemical box model dataset used by Adams et al. (2016) and the one used in the present work, which differ in the model input parameters, are referred to in the discussion herein as PRATMO⁺ and PRATMO⁺⁺, respectively. The input parameters used in the photochemical box model to produce PRATMO⁺ are no longer available. The overall dependence of the results on the photochemical box model is reduced by only calculating the OSIRIS gridded NO₂ VCD maps, and therefore the final OMI-minus-OSIRIS (OmO) and TROPOMI-minus-OSIRIS (TROPOmO) tropospheric VCDs, between 70°S and 70°N. The reason for this is that the average tropopause height decreases closer to the poles, resulting in a higher fraction of OSIRIS profiles requiring altitude extrapolation down to the tropopause and therefore an overall larger dependence on the photochemical box model.

A sample of OmO NO₂ data for 3-5 March 2008, provided by the first author of Adams et al. (2016), is used to verify the algorithm of the present work and to analyze differences due to different photochemical box model input parameters and different OMI-SP data versions. Following the work by Adams et al. (2016) and the SCIAMACHY limb-nadir matching by Hilboll et al. (2013), the resulting tropospheric NO₂ VCDs in the present work are validated by analyzing their values over the Pacific Ocean where little to no tropospheric pollution is expected. Other regions are not used in the validation as they are more dependent on anthropogenic emissions, resulting in more variation and uncertainties.

4.3 Results

4.3.1 OSIRIS NO₂ Data Version Comparison

In the process of producing gridded stratospheric NO₂ VCD maps with the publicly released version 6 OSIRIS NO₂ data, a bias between the version 6 data product and version 3 data product used by Adams et al. (2016) was discovered. Fig. 4.1 shows the absolute and percent differences between the version 6 and version 3 stratospheric NO₂ profiles over the year 2008. The average over the year is taken for each profile altitude and each 5° latitude bin between

70°S and 70°N. Fig. 4.1(a) shows a nearly-constant systematic bias of approximately 1×10^8 molecules/cm³ between the two data products that is not latitude-dependent. Fig. 4.1(b) shows that the version 6 stratospheric profiles are on average roughly 20% lower than the version 3 profiles, with the percent difference reaching upwards of 67% near the top and bottom of the profiles. Note that the profiles are only shown up to 40 km as the number densities are significantly lower above 40 km, resulting in little contribution to the final VCDs.

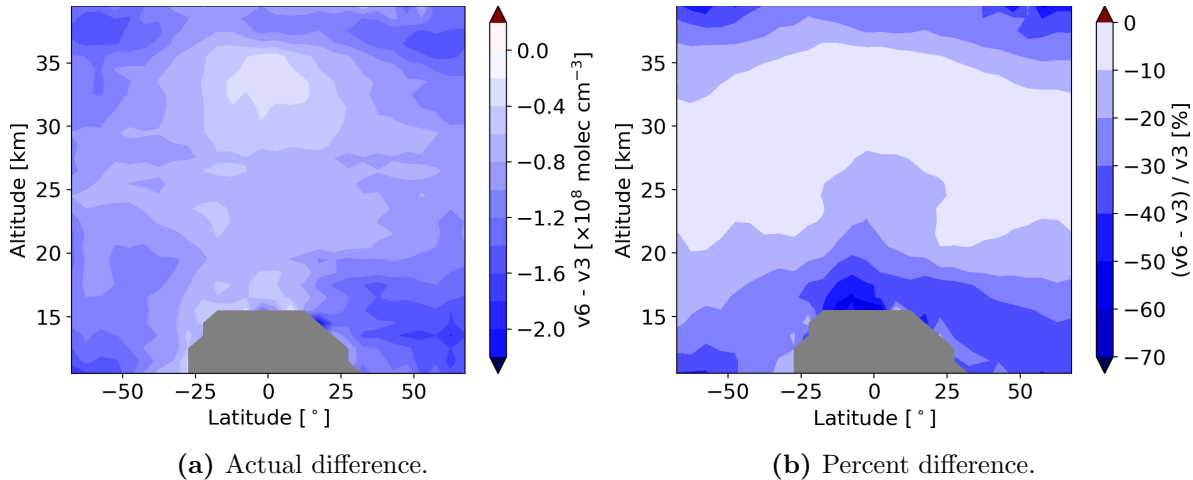


Figure 4.1. Mean difference between version 6 and version 3 OSIRIS stratospheric NO₂ density profiles in 2008 for 5° latitude bins between 70°S and 70°N. Grey indicates regions that are below the tropopause year-round.

Due to the higher amount of validation for the version 3 data product (Adams et al., 2012; Brohede et al., 2008; Haley & Brohede, 2007), it is assumed that the bias between version 3 and version 6 is primarily due to a systematic bias in the version 6 data product. Consequently, work was done by the Atmospheric Research Group at the University of Saskatchewan to determine improvements in the retrieval algorithm and to see if this could reduce the bias. This work resulted in a version 7 data product retrieval algorithm, which differs from that of the version 6 data product mainly in the OSIRIS spectral point spread function fitting and the cloud-aerosol discrimination. Specifically, the spectral point spread function fitting is done with solar Fraunhofer lines instead of pre-flight calibrated values and an improvement in the detection of cloudy scenes allows for more profiles to be retrieved

down to the lower stratosphere and upper troposphere. Fig. 4.2 shows a comparison between version 7 and version 3 profiles, along with the version 7 retrieved profile error (Fig. 4.2(c)), in 2008 for 5° latitude bins between 70°S and 70°N.

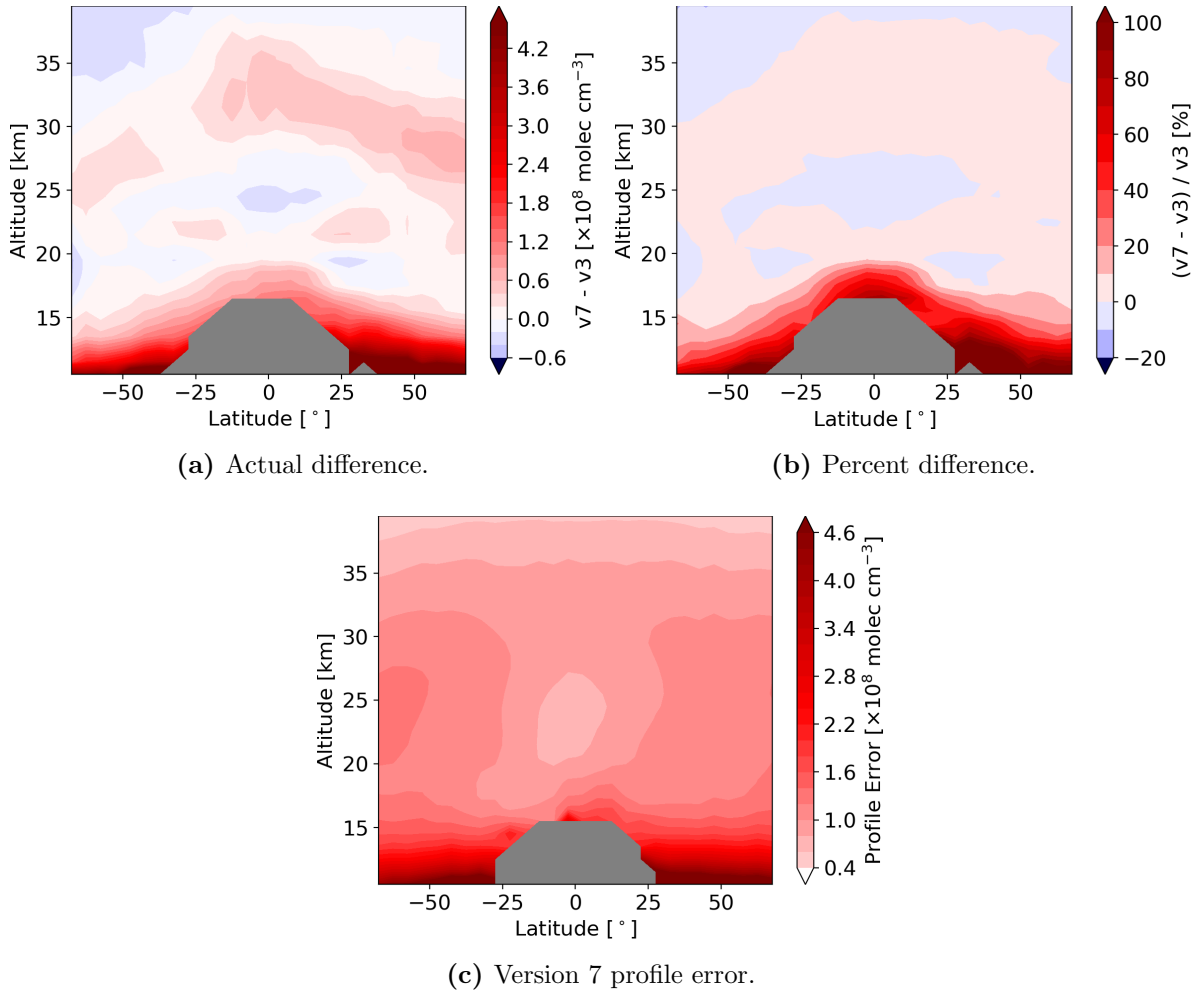


Figure 4.2. Mean difference between version 7 and version 3 OSIRIS stratospheric NO₂ density profiles, and mean version 7 retrieved profile error, in 2008 for 5° latitude bins between 70°S and 70°N. The colour mapping in (a) and (c) is the same as in Fig. 4.1(a) and the colour mapping of (b) is the same as in Fig. 4.1(b). Grey indicates regions that are below the tropopause year-round.

Figs. 4.2(a) and 4.2(b) indicate that the version 7 NO₂ profiles have virtually no bias above the mean tropopause altitude compared to the version 3 profiles. From Fig. 4.2(b), ver-

sion 7 profiles are on average approximately 10% higher than the version 3 profiles in the stratosphere. Between 19 and 40 km, the average percent difference is 1%. The version 7 and version 3 OSIRIS NO₂ profiles appear to agree with each other as their mean difference (Fig. 4.2(a)) is smaller than or equal to the mean version 7 NO₂ retrieval error (Fig. 4.2(c)).

4.3.2 OSIRIS Gridded Stratospheric NO₂ VCD Maps

In the non-coincident limb-nadir matching method, OSIRIS NO₂ profiles are scaled in local solar time using Eq. (2.41), integrated over altitudes to get stratospheric VCDs, and summed with the weights in Eq. (2.43) to get stratospheric gridded maps. For the present work, this is done for OSIRIS version 6 and 7 NO₂ profiles. Fig. 4.3 compares the OSIRIS gridded NO₂ stratospheric VCD maps of the present work, for both version 6 (Fig. 4.3(a)) and 7 (Fig. 4.3(b)) OSIRIS profiles, to those of Adams et al. (2016) that use version 3 OSIRIS profiles (Fig. 4.3(c)). In each case, maps are shown for 4 March 2008 and 21 June 2008, and for 07:00 and 13:00 local time. The version 6 and 7 maps of the present work use PRATMO⁺⁺ while the version 3 maps of Adams et al. (2016) use PRATMO⁺. Note that the version 6 OSIRIS data has a more strict filtering of measurements in the retrieval, resulting in the lower coverage that can be seen in Fig. 4.3(a).

Comparing each of the four OSIRIS version 6 maps of Fig. 4.3(a) to each corresponding version 3 map in Fig. 4.3(c) demonstrates a nearly constant bias of roughly -0.5×10^{15} molecules/cm² in the version 6 maps compared to the version 3 maps, without a clear latitude dependence. For example, the region in the tropics (23°S-23°N) of each map in Fig. 4.3(a) can be seen to be lower than the region in the tropics of each corresponding map in Fig. 4.3(c).

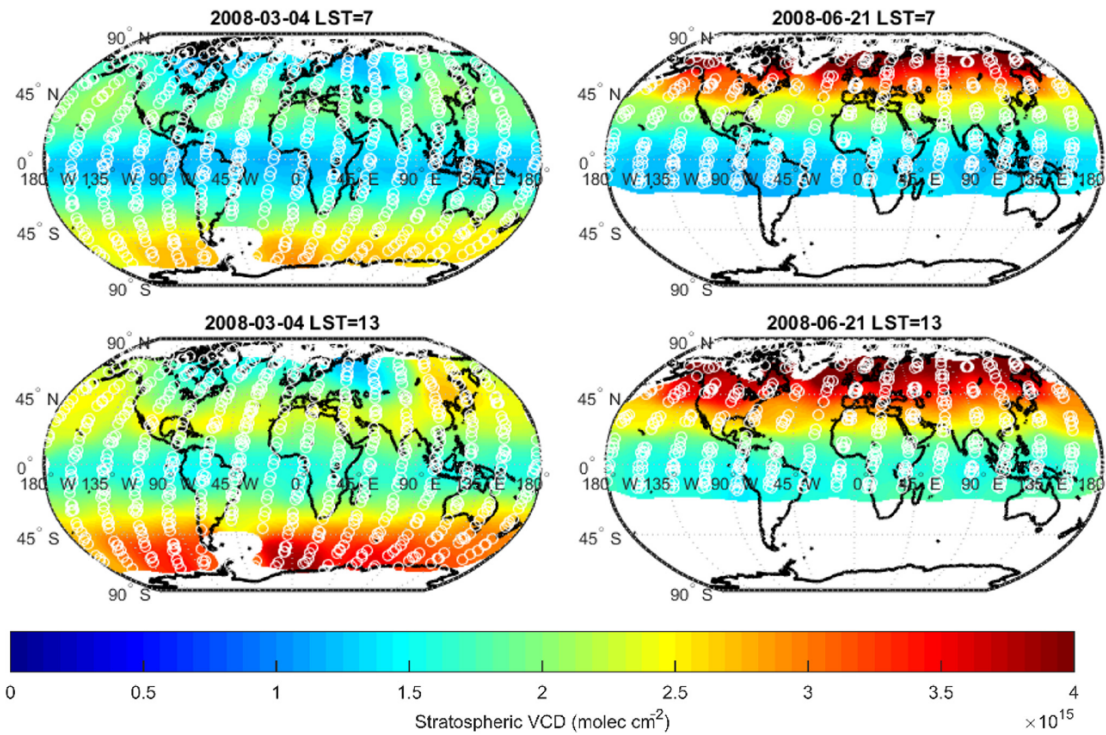
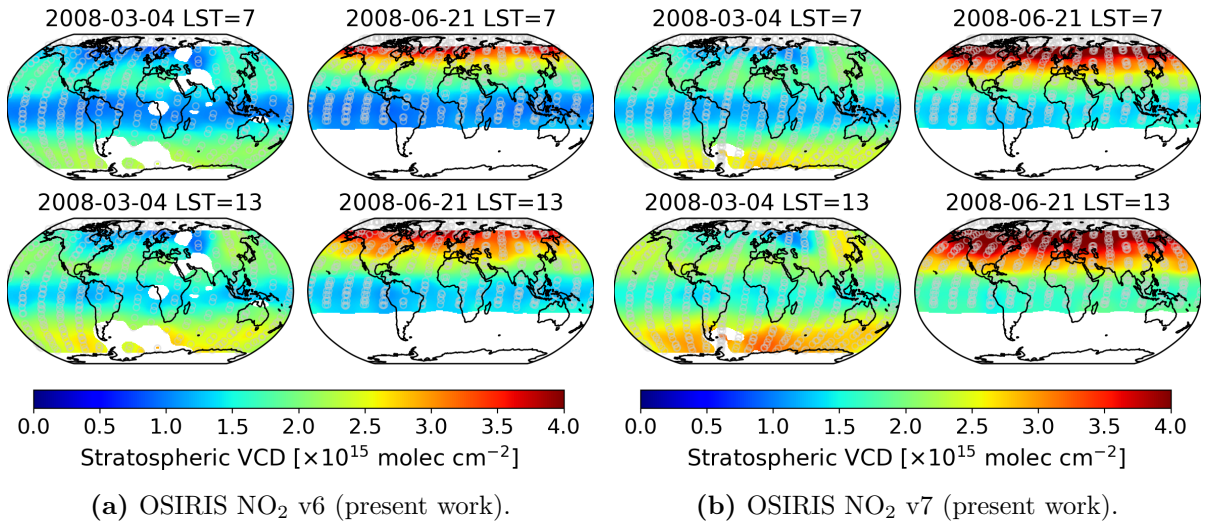


Figure 4.3. Comparison of 2008 gridded OSIRIS stratospheric NO₂ VCD maps between (a) version 6 (present work), (b) version 7 (present work), and (c) version 3 (Adams et al., 2016) OSIRIS profile data. In each case, maps are shown for 4 March and 21 June 2008 (columns of maps for each subfigure) at local solar time 07:00 and 13:00 (rows of maps for each subfigure). The white or grey circles in each map show the tangent-point coordinates of OSIRIS measurements used to construct the map.

Comparing each of the four OSIRIS version 7 maps of Fig. 4.3(b) to each corresponding version 3 map in Fig. 4.3(c) shows that the 4 March 2008 maps are up to 0.5×10^{15} molecules/cm² lower for version 7 compared to version 3 (e.g., see the regions below 45°S) and the 21 June 2008 maps are up to 0.5×10^{15} molecules/cm² higher for version 7 compared to version 3 (e.g., see the regions around and above 45°N), with the largest discrepancies in the northern and southern midlatitudes. Nonetheless, there is an overall lower average discrepancy between version 7 and version 3 maps compared to that between version 6 and version 3 maps.

Figs. 4.4 and 4.5 show the difference and percent difference, respectively, in OSIRIS gridded stratospheric NO₂ VCD maps on 4 March 2008 due to either the algorithm version, the OSIRIS NO₂ version, or the photochemical box model input parameters. This makes use of the sample data provided by the first author of Adams et al. (2016). The grey circles show the tangent-point latitude and longitude for each OSIRIS measurement used in producing the map. Grey indicates regions where there are insufficient nearby OSIRIS measurements to define these grid points of the map. See Section 2.6 for details about the definition of each grid point value.

The top rows of Figs. 4.4 and 4.5 compare maps using the algorithm of the present work to maps using the algorithm of Adams et al. (2016), with OSIRIS NO₂ version 3 and the PRATMO⁺ sample data provided by Adams et al. (2016) used in both cases. This validates the algorithm of the present work. The middle rows of Figs. 4.4 and 4.5 compare maps using OSIRIS NO₂ version 7 (present work) to maps using OSIRIS NO₂ version 3 (Adams et al., 2016), with PRATMO⁺⁺ and the present algorithm used in both cases. This increases the confidence in the OSIRIS NO₂ version 7 data in reference to the highly-validated version 3 data. The bottom rows of Figs. 4.4 and 4.5 compare maps using PRATMO⁺⁺ (present work) to maps using PRATMO⁺ (Adams et al., 2016), with OSIRIS NO₂ version 7 and the present algorithm used in both cases. The bottom row of Fig. 4.5 shows that the use of PRATMO⁺⁺ can cause the maps to be upwards of 30% lower than those resulting from the use of PRATMO⁺.

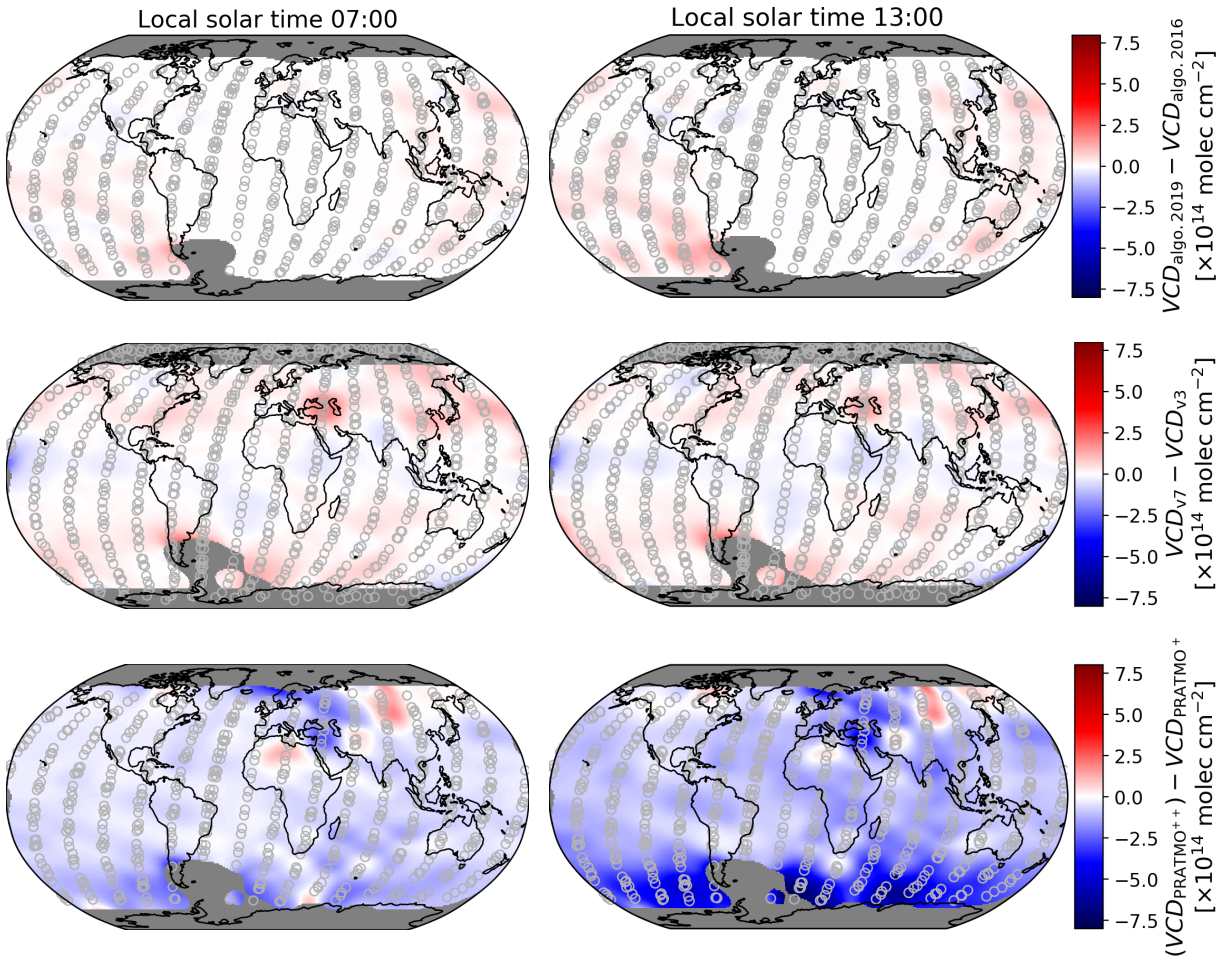


Figure 4.4. Difference in OSIRIS gridded stratospheric NO_2 VCD maps on 4 March 2008 at 07:00 (first column) and 13:00 (second column) local time due to the algorithm version (top row), OSIRIS NO_2 version (middle row), and PRATMO photochemical box model dataset (bottom row). The algorithms from the present work and from Adams et al. (2016) are denoted by “algo. 2019” and “algo. 2016”, respectively. The grey circles show the tangent-point latitude and longitude for each OSIRIS measurement used in producing the map. Grey indicates regions where there are insufficient nearby OSIRIS measurements to define these grid points of the map.

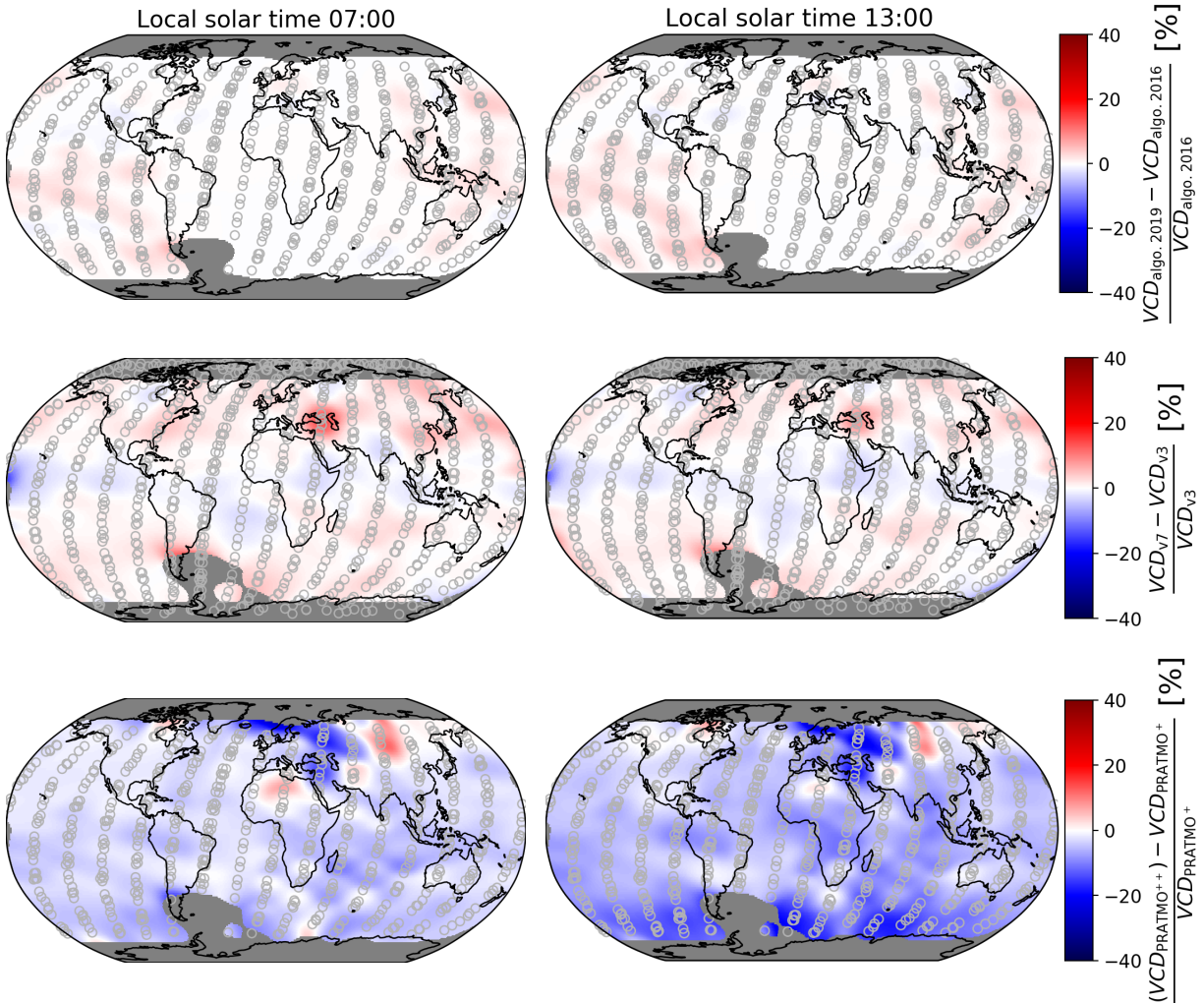


Figure 4.5. Percent difference in OSIRIS gridded stratospheric NO_2 VCD maps on 4 March 2008 at 07:00 (first column) and 13:00 (second column) local time due to the algorithm version (top row), OSIRIS NO_2 version (middle row), and PRATMO photochemical box model dataset (bottom row). The algorithms from the present work and from Adams et al. (2016) are denoted by “algo. 2019” and “algo. 2016”, respectively. The grey circles show the tangent-point latitude and longitude for each OSIRIS measurement used in producing the map. Grey indicates regions where there are insufficient nearby OSIRIS measurements to define these grid points of the map.

4.3.3 OSIRIS-OMI Limb-Nadir Matching Reanalysis

Fig. 4.6 compares mean stratospheric VCDs, in the year 2008 for 10° latitude bins from 60°S to 60°N , resulting from OSIRIS version 3 and 7 data, and from OMI version 2 and 4 data. The OMI-SP version 2 data is adapted from Adams et al. (2016) where a known SCD bias is corrected using the correction factors of Marchenko et al. (2015). Overall, the OSIRIS version 7 VCDs are only slightly higher than the version 3 VCDs, with the difference being at most less than 0.1×10^{15} molecules/cm². Compared to the bias-corrected version 2 OMI-SP stratospheric VCDs, the OMI-SP version 4 stratospheric VCDs used in the present work are larger by approximately 0.1×10^{15} to 0.2×10^{15} molecules/cm² between latitude bins centered at 45°S and 45°N , with the difference increasing as the bin center approaches 0° .

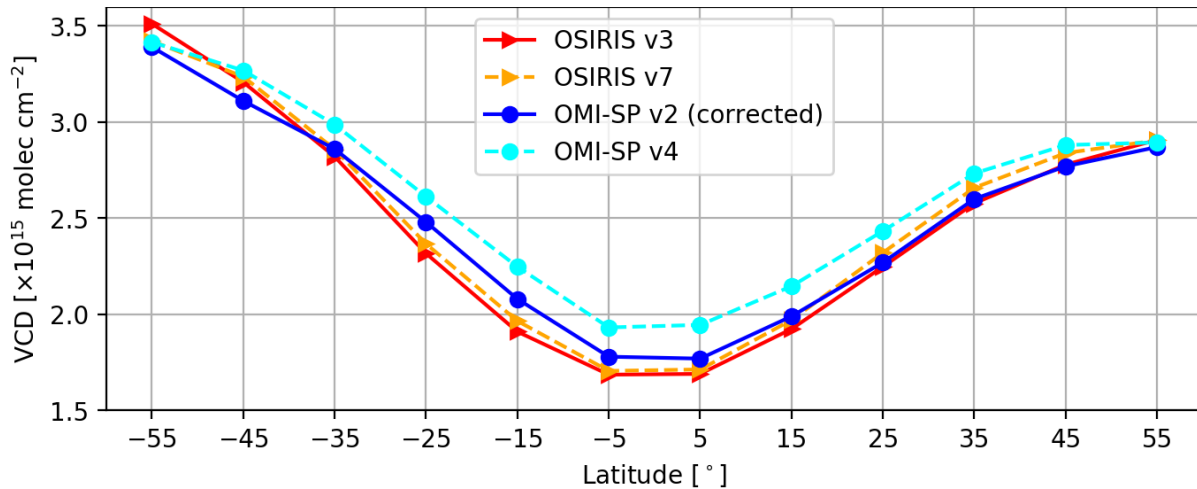


Figure 4.6. 2008 mean stratospheric NO₂ vertical column densities (VCDs) in 10° latitude bins for measurements where OMI tropospheric VCDs are less than 0.5×10^{15} molecules/cm². The OMI-SP version 2 data is adapted from Adams et al. (2016), where correction factors of Marchenko et al. (2015) are used to account for the positive bias in the version 2 slant column densities.

Fig. 4.7 shows the monthly mean difference between OSIRIS version 7 and OMI-SP version 4 stratospheric VCDs from January 2005 to February 2020 in 10° latitude bins from 70°S to 70°N . The breaks in the time series are due to limited OSIRIS measurement coverage in either hemisphere in their respective winter. The OSIRIS stratospheric VCDs are smaller on

average than those of OMI for latitude bin centers from approximately 45°S to 45°N. The average difference reaches upwards of 0.2×10^{15} molecules/cm³ near the equator. This is consistent with the 2008 mean stratospheric VCD results in Fig. 4.6.

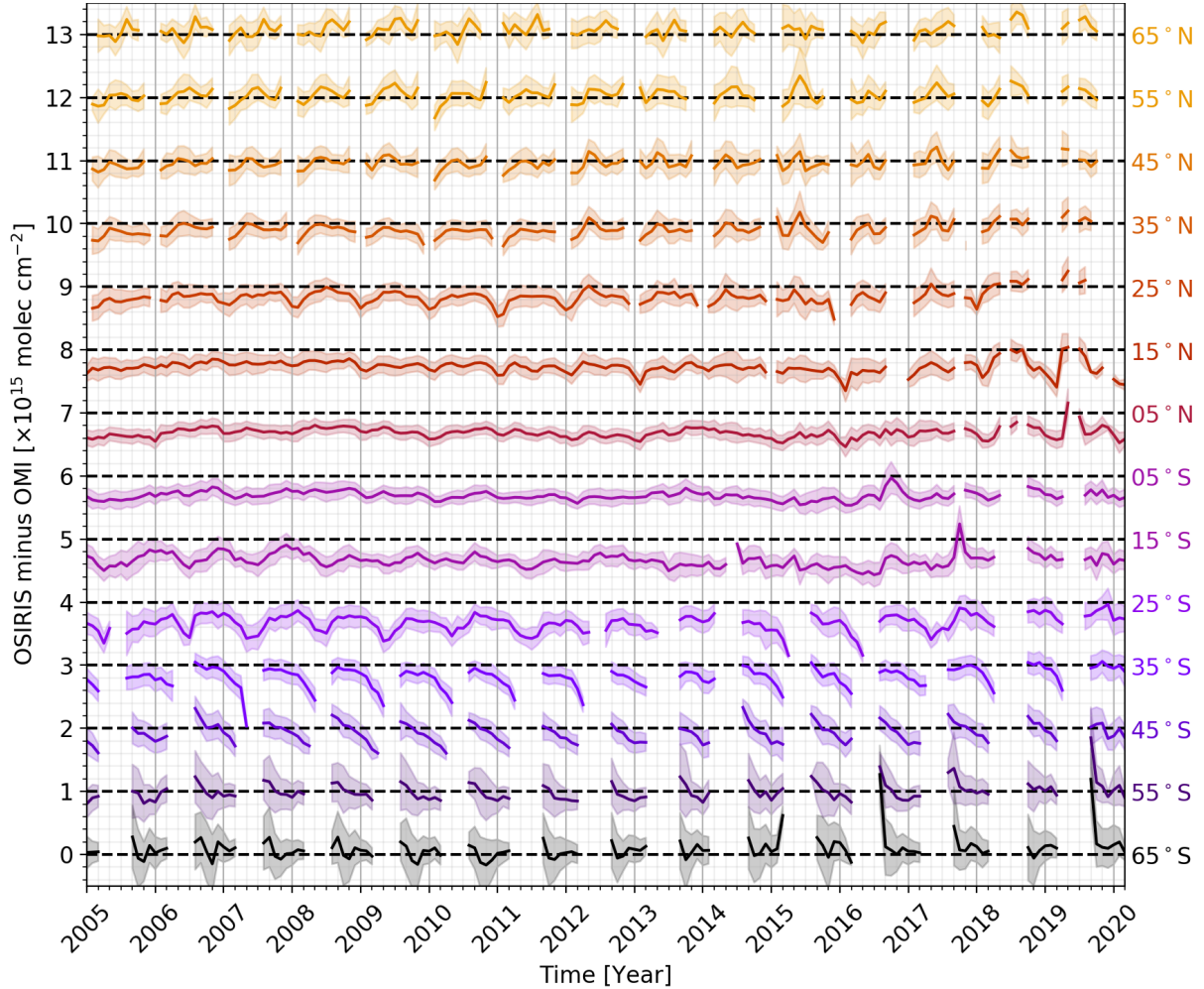


Figure 4.7. Monthly mean and standard deviation (shaded areas) of OSIRIS version 7 minus OMI-SP version 4 stratospheric NO₂ VCDs for 10° latitude bins. Starting at the 65°S-centered bin, each plot line of the following latitude bin is offset by 1×10^{15} molecules/cm² from the previous plot line. The offsets are shown as dashed black lines.

Fig. 4.8 shows the 2008 mean OmO and OmO-minus-OMI tropospheric VCD maps for OSIRIS version 7 and OMI-SP version 4 NO₂ data. Note from Eq. (2.44) that the difference between the OmO and OMI tropospheric VCD maps is given by

$$V_{\text{trop}}^{\text{OmO}} - V_{\text{trop}}^{\text{OMI}} = (V_{\text{strat}}^{\text{OMI}} - V_{\text{strat}}^{\text{OSIRIS}}) \cdot A_{\text{strat}}^{\text{OMI}} / A_{\text{trop}}^{\text{OMI}}, \quad (4.1)$$

and is therefore only dependent on the stratospheric OMI and OSIRIS VCDs, and the stratospheric and tropospheric OMI AMFs. Given Eq. (4.1), the 2008 mean OmO-OMI tropospheric VCD difference in Fig. 4.8(c) is consistent with the monthly mean OSIRIS-OMI stratospheric VCD difference in Fig. 4.7. From Fig. 4.8(c), the OmO map is up to approximately 0.5×10^{15} molecules/cm² larger than that in Fig. 11 of Adams et al. (2016) between about 50°S and 60°N.

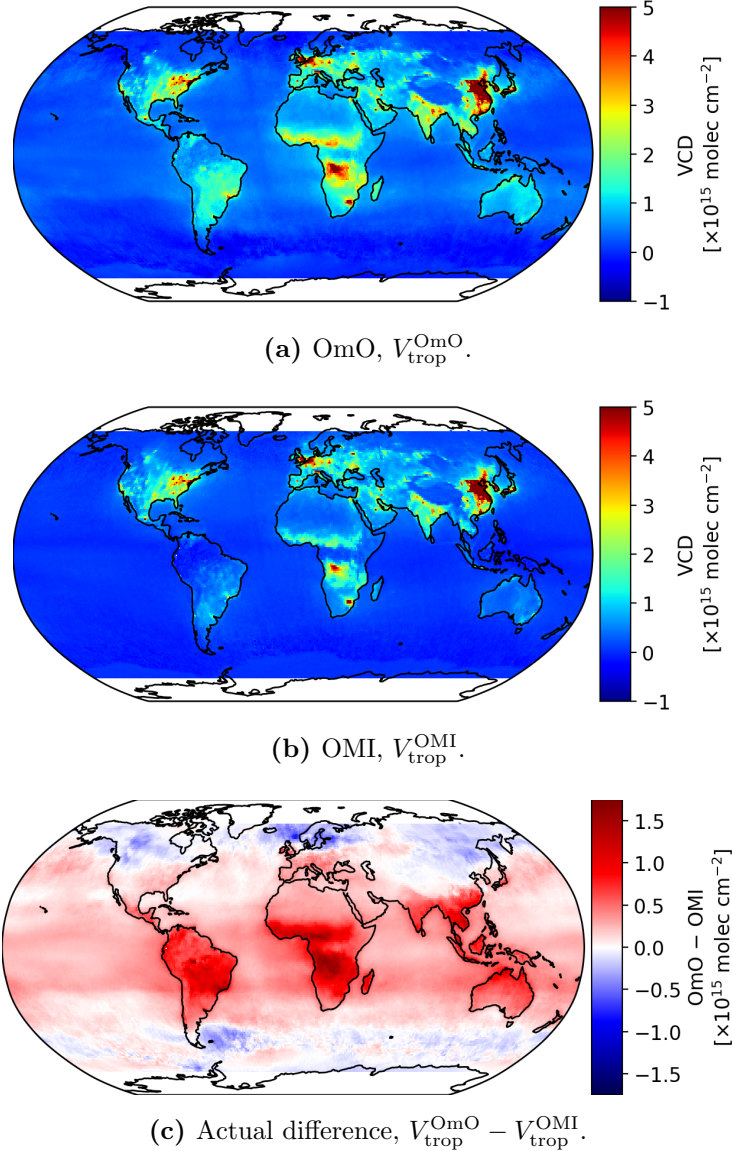


Figure 4.8. Mean 2008 OmO, OMI, and OmO-minus-OMI tropospheric VCD maps for a $1^\circ \times 1^\circ$ latitude-longitude grid. OSIRIS version 7 and OMI-SP version 4 NO₂ datasets are used.

4.3.4 OMI-minus-OSIRIS Product Validation

Following the work of Adams et al. (2016) and the simulations of Hilboll et al. (2013), it is assumed that tropospheric VCDs over the Pacific Ocean are less than 3×10^{14} molecules/cm² in the tropics (23°S to 23°N) due to low emissions, with VCDs in the northern midlatitudes (23°N to 66°N) reaching upwards of 7×10^{14} molecules/cm². Fig. 4.9 shows the mean of OmO tropospheric NO₂ VCDs over the Pacific from 2005 to 2019 for each of the twelve months and each 2° latitude bin between 70°S and 70°N. OSIRIS version 7 and OMI-SP version 4 data is used. White in the color map corresponds to the expected 3×10^{14} molecules/cm² maximum in the tropics. Grey regions indicate a lack of measurements due to the limited OSIRIS coverage in each hemisphere during their respective winter.

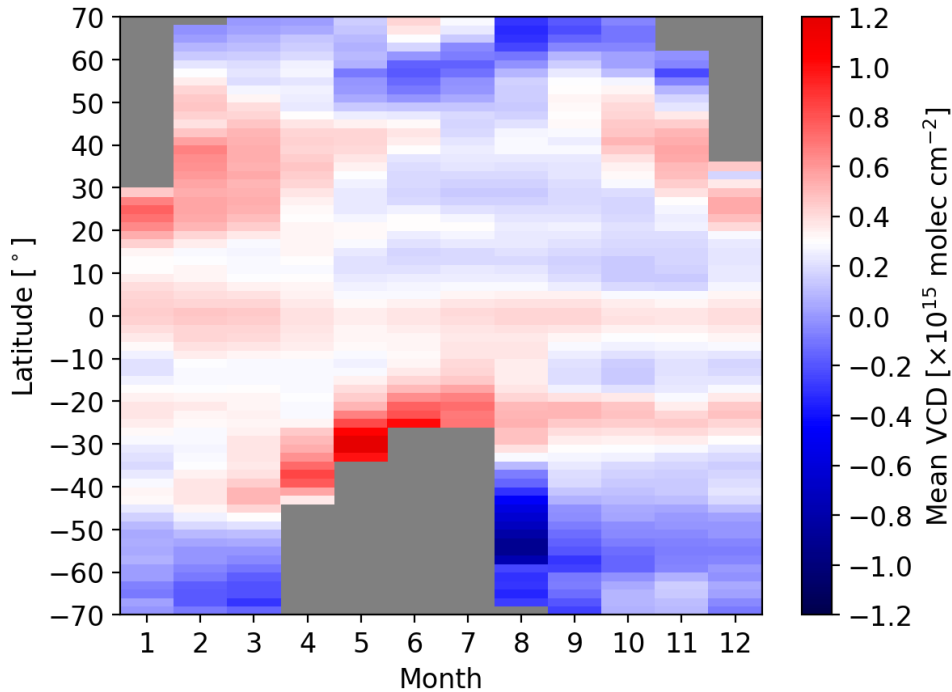


Figure 4.9. Mean OMI-minus-OSIRIS (OmO) tropospheric NO₂ VCDs for 2° latitude bins from 2005 to 2019. White corresponds to $+3 \times 10^{14}$ molecules/cm². OSIRIS version 7 and OMI-SP version 4 data is used.

From Fig. 4.9, with the exception of a strip along the equator, the tropical OmO VCDs are generally at or below the assumed maximum of 3×10^{15} molecules/cm². Similar to

the simulations in Hilboll et al. (2013), the OmO VCDs in the northern midlatitudes reach upwards of approximately 7×10^{14} molecules/cm², but are even higher towards the edge of coverage. The OmO VCDs are significantly larger than expected between about 40°S to 20°S in the period of April to July, around the edge of the OSIRIS coverage.

Fig. 4.10 compares, between OMI and OmO, the changes in tropospheric NO₂ VCDs relative to 2005 in the five regions analyzed in Fig. 3 of Krotkov et al. (2016), for OSIRIS version 7 and OMI-SP version 4 data. The crosses in Fig. 4.10 denote de-seasonalized monthly VCDs while the circles and error bars denote their yearly means and standard deviations, respectively. The de-seasonalized monthly VCDs are obtained by first, for each month from January to December, calculating the mean of all VCDs of the given month from the full 2005-2019 period. Next, the resulting mean monthly VCDs are subtracted from the corresponding monthly mean of each individual year. Finally, to make the de-seasonalized monthly VCDs be relative to the year 2005, the mean de-seasonalized monthly VCD for 2005 is subtracted from all de-seasonalized monthly VCDs. To handle outliers, de-seasonalized monthly VCDs from a given instrument are only included if there are at least 100 VCDs in the given month, year, and geographic region of interest. The threshold of 100 is chosen as increasing to 150 results in almost no difference and increasing further to 200 results in the coverage suffering.

The trends in Fig. 4.10 follow closely to those in Fig. 3 of Krotkov et al. (2016). There is a larger OmO-OMI discrepancy towards the end of the time series (years 2018 and 2019). It should be noted that, due to the aging OSIRIS instrument, there are fewer measurements towards the end of the time series, affecting the number of OmO data points. Fig. 4.10 shows that over the Ohio River Valley and southwestern Pennsylvania, the OmO tropospheric VCDs are approximately 1×10^{15} molecules/cm² lower on average than those of OMI. This is the only region out of the selected set that has a positive OmO bias relative to OMI in the last couple of years; the other regions have a negative bias.

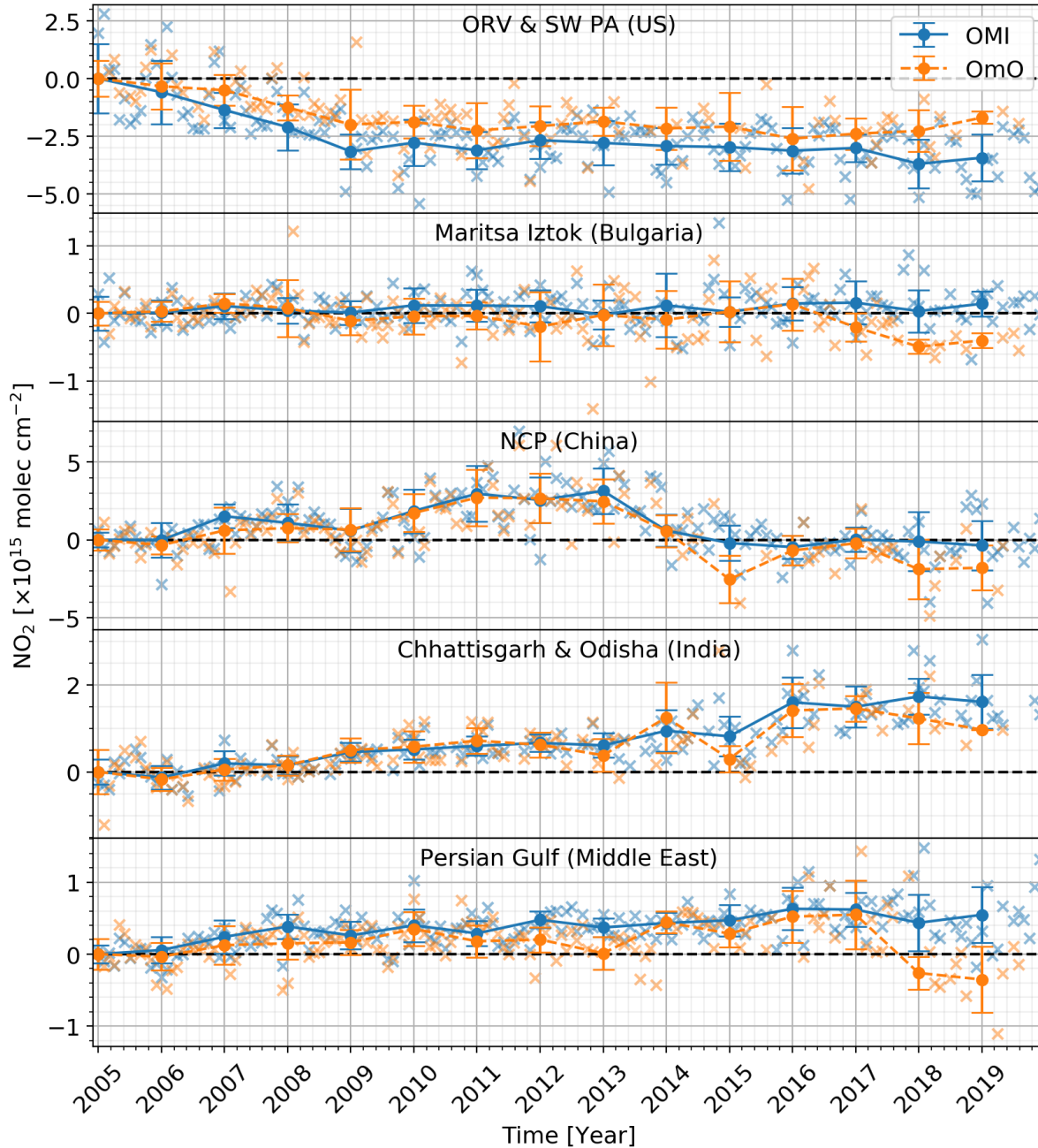


Figure 4.10. Comparison between OmO and OMI changes in tropospheric NO_2 VCDs relative to 2005. The regions are the same as those used for Fig. 3 of Krotkov et al. (2016); from top to bottom: Ohio River Valley and southwestern Pennsylvania (corners 38°N - 81.6°W , 39°N - 83°W , 40.6°N - 78°W , 41.7°N - 79.2°W), Maritsa Iztok power plants in Bulgaria (bounded by 40.5 - 43.8°N , 23.7 - 28.1°E), North China Plain (bounded by 34 - 38°N , 112 - 118°E), Chhattisgarh and Odisha (bounded by 21 - 25°N , 81 - 85°E), and the Persian Gulf (corners 22.6°N - 54.1°E , 25.6°N - 56.5°E , 29.5°N - 46.9°E , 30.6°N - 49.8°E).

4.3.5 OSIRIS-TROPOMI Limb-Nadir Matching Analysis

Fig. 4.11 compares OmO and TROPOMO tropospheric maps for four different days spread out over the year 2018, where there is measurement coverage overlap between OSIRIS, OMI, and TROPOMI. The four days of 2018, March 3, May 18, October 19, and December 20, are chosen as a balance between the amount of coverage overlap and the proximity to the equinoxes and solstices. Proximity to the equinoxes and solstices is chosen to provide the extreme and median yearly seasonal scenarios. The maps result from the use of OSIRIS version 7, OMI-SP version 4, and TROPOMI version 1.3 NO₂ data. There appears to be a bias between corresponding TROPOMO and OmO maps, with the TROPOMO maps being larger than the OmO maps and the bias being independent on geographic location. The larger gaps in the OmO maps relative to the TROPOMO maps are due to increased gaps in the data of the aging OMI instrument relative to the successor TROPOMI instrument.

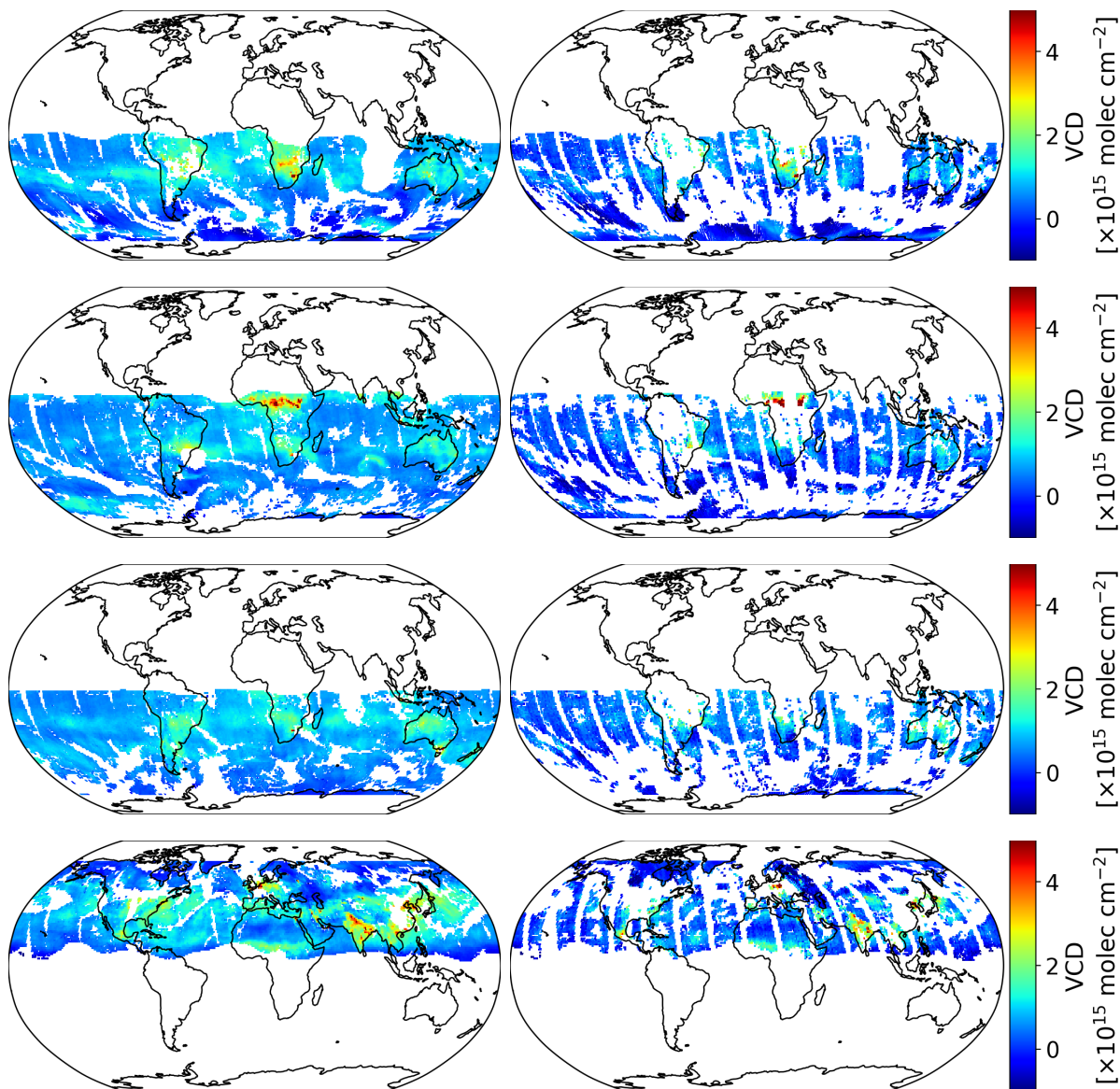


Figure 4.11. Comparison of TROPOMO (left column) and OmO (right column) tropospheric VCD maps for 2018-10-19 (first row), 2018-12-20 (second row), 2019-03-03 (third row), and 2019-05-18 (last row). The maps result from OSIRIS version 7, OMI-SP version 4, and TROPOMI version 1.3 NO_2 data.

4.3.6 TROPOMI-minus-OSIRIS Product Validation

Fig. 4.12 compares the OMI and TROPOMI results over the Pacific for the same four days as the OmO and TROPOMO maps in Fig. 4.11. OSIRIS version 7, OMI-SP version 4, and

TROPOMI version 1.3 NO₂ data are used.

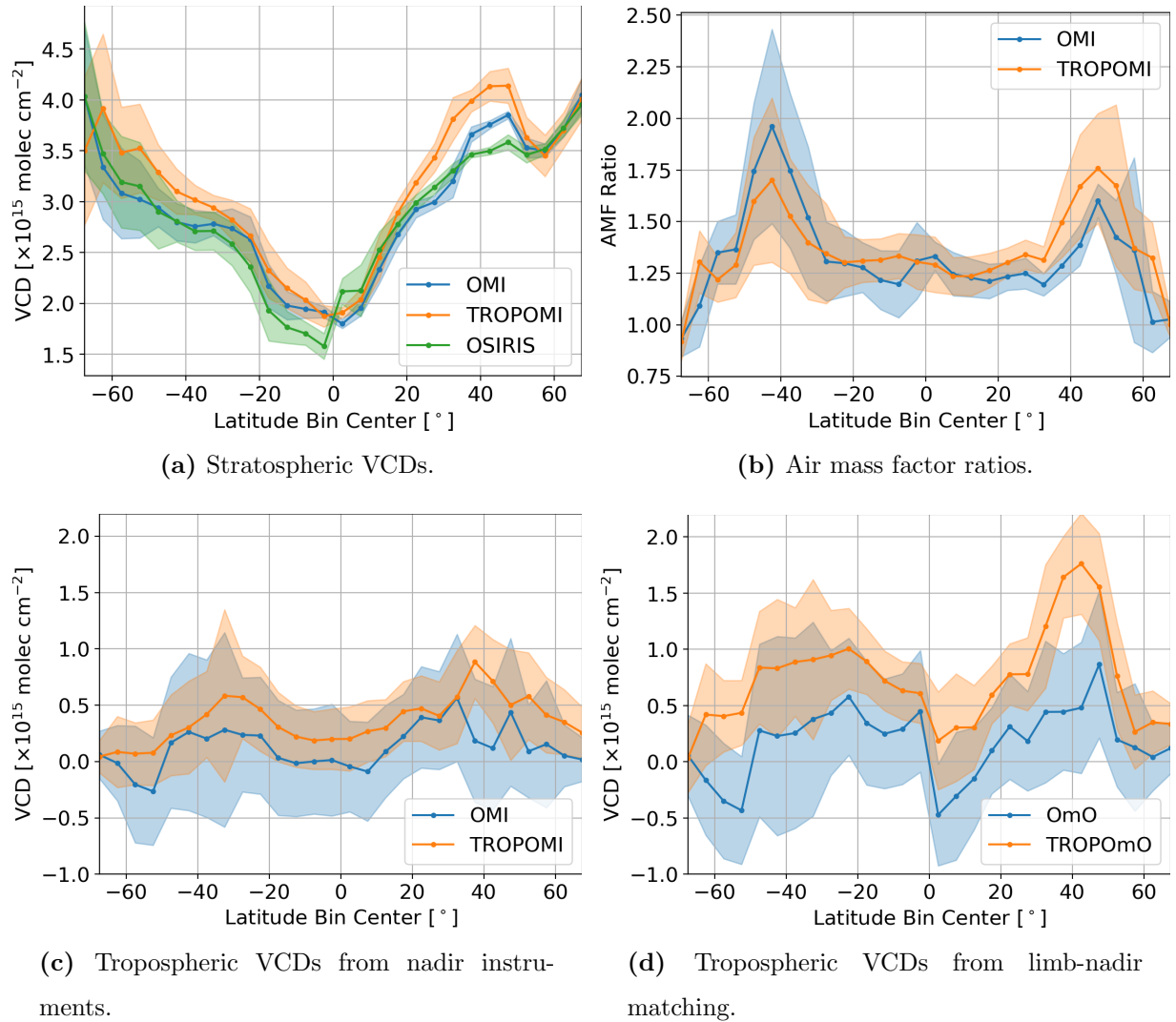


Figure 4.12. Mean and standard deviation (shaded regions) of OMI and TROPOMI results over the Pacific (180°W - 150°W) for 2018-10-19, 2018-12-20, 2019-03-03, and 2019-05-18. OSIRIS version 7, OMI-SP version 4, and TROPOMI version 1.3 NO₂ data are used.

Fig. 4.12 shows a positive bias of both the tropospheric and stratospheric TROPOMI VCDs relative to those of OMI. The TROPOMo tropospheric VCDs are on average roughly 0.5×10^{15} molecules/ cm^2 higher than the OmO tropospheric VCDs, which appears to be consistent with the bias between the OmO and TROPOMo tropospheric VCD maps of Fig. 4.11. The

maximum difference is approximately 1.2×10^{15} molecules/cm² near 40°N. The TROPOMI, OMI, and OmO tropospheric VCDs in the Pacific are at or below both the expected 3×10^{14} molecules/cm² in the tropics and the 7×10^{14} molecules/cm² in the northern midlatitudes. The TROPOMI tropospheric VCDs in the Pacific, however, exceed the expected maximum values, especially near 40°N.

4.4 Discussion

4.4.1 OSIRIS Gridded Stratospheric NO₂ VCD Maps

The bias of -0.5×10^{15} molecules/cm² in the OSIRIS version 6 stratospheric VCD maps (Fig. 4.3(a)) relative to the OSIRIS version 3 VCD maps (Fig. 4.3(c)) can be mostly explained by the nearly-constant bias of approximately -1×10^8 molecules/cm³ in the version 6 stratospheric density profiles compared to the version 3 profiles (Fig. 4.1), given that the profiles are integrated over roughly 0.3×10^7 to 0.4×10^7 cm of altitude. This is consistent with the fact that the bias is significantly reduced when using OSIRIS version 7 data (Fig. 4.3(b)), which is closer to the version 3 data (Fig. 4.2). A secondary source of the bias is the difference between the present work and the work by Adams et al. (2016) due to the photochemical box model input parameters (bottom rows of Figs. 4.4 and 4.5). Future work, detailed in Section 4.5.2, is recommended to determine the effect of the photochemical box model input parameters on the NO₂ density scaling.

4.4.2 OSIRIS-minus-OMI Tropospheric NO₂ VCDs

The positive bias in the OmO tropospheric VCDs (Fig. 4.8) between 50°S and 60°N relative to the results of Adams et al. (2016) can be principally explained by the positive bias of up to 0.2×10^{15} molecules/cm² in OMI stratospheric VCDs due to the OMI-SP data version (Fig. 4.6) and negative bias of up to approximately 0.2×10^{15} molecules/cm² in the OSIRIS stratospheric VCDs due to the photochemical box model input parameters (bottom row of Fig. 4.4). Note from Eq. (2.44) that the OmO tropospheric VCD is defined as

$$V_{\text{trop}}^{\text{OmO}} = V_{\text{trop}}^{\text{OMI}} + (V_{\text{strat}}^{\text{OMI}} - V_{\text{strat}}^{\text{OSIRIS}}) \cdot A_{\text{strat}}^{\text{OMI}} / A_{\text{trop}}^{\text{OMI}}. \quad (4.2)$$

Thus, the biases in the OMI and OSIRIS stratospheric VCDs ($V_{\text{strat}}^{\text{OMI}}$ and $V_{\text{strat}}^{\text{OSIRIS}}$) are magnified by the OMI stratosphere-to-troposphere AMF ratio ($A_{\text{strat}}^{\text{OMI}}/A_{\text{trop}}^{\text{OMI}}$), which is generally between 1 and 2 (e.g., see Fig. 4.12(b)). There is also a possibility of a discrepancy in the OMI AMFs between the version 2 and 4 OMI-SP NO₂ datasets, which should be investigated as part of the future work.

In the validation of the OmO tropospheric VCDs over the Pacific Ocean (Fig. 4.9), the high OmO VCDs near the edge of the coverage between about 40°S and 20°S in the period of April to July could be explained by the diurnal effect caused by the high solar zenith angle for the OSIRIS measurements (Hendrick et al., 2006; McLinden et al., 2006). Another possible source is the effect of the scaling with the photochemical box model. There are significant diurnal changes in the NO₂ concentration near the solar terminator where the OSIRIS coverage ends. It is possible that scaling the OSIRIS profiles with the photochemical box model data does not properly account for these diurnal NO₂ effects near the solar terminator, either due to the photochemical box model itself or to the method of using it to scale the OSIRIS profiles. As this has the largest effect for higher SZAs, the maximum SZA of 88° used to filter the input OSIRIS NO₂ data could be lowered to reduce the overall error.

From the select-region trend analysis of Fig. 4.10, the OmO and OMI tropospheric VCDs in each select region agree with each other from 2005 to 2017, and with the results of Krotkov et al. (2016), within error. The OmO-OMI discrepancy for 2018 and 2019 is at least partially explained by the decrease in the number of OmO measurements due to the aging OSIRIS instrument. From the expression for the OmO tropospheric VCDs (Eq. (4.2)), a discrepancy between OMI and OmO tropospheric VCDs could be due to a discrepancy between the OSIRIS and OMI stratospheric VCDs or to the OMI stratosphere-to-troposphere AMF ratio. Note that for the regions used in the analysis, the corners range in latitude from approximately 21°N to 44°N. From the monthly OMI and OSIRIS stratospheric NO₂ VCD analysis in Fig. 4.7, 2018 and 2019 around this latitude range generally shows larger OSIRIS stratospheric VCDs relative to those of OMI, especially in 2019. This could help explain the discrepancy in the last few years, but there are likely other differences such as those of the OMI tropospheric and stratospheric AMFs due to the OMI-SP data version. This should be

investigated in the future work.

The overall negative bias of the OmO VCD trends relative to those of OMI for the Ohio River Valley and southwestern Pennsylvania in Fig. 4.10 is not clearly explained by the trends in the OSIRIS and OMI stratospheric VCDs in Fig. 4.7. Future work should include more analyses of the trends over different regions to determine if the aforementioned bias is an anomaly or if it occurs in other regions and time periods and should be investigated further to determine the cause.

4.4.3 TROPOMI-minus-OSIRIS Tropospheric NO₂ VCDs

Roughly half of the OmO-TROPOMI tropospheric VCD bias in Fig. 4.11 appears to be due to the OMI-TROPOMI tropospheric VCD bias (Fig. 4.12(c)). According to the OmO-OMI tropospheric VCD difference in Eq. (4.1), the other half of the OmO-TROPOMI tropospheric VCD bias results from the OMI-TROPOMI stratospheric VCD bias (Fig. 4.12(a)) multiplied by the stratosphere-to-troposphere AMF ratio. As the stratosphere-to-troposphere AMF ratio is generally greater than 1, the OMI-TROPOMI stratospheric VCD bias is smaller than the tropospheric VCD bias but has a similar effect on the OmO-TROPOMI tropospheric VCD bias. The fact that the TROPOMI tropospheric VCDs in the Pacific are not below the expected 3×10^{14} molecules/cm² in the tropics and 7×10^{14} molecules/cm² in the midlatitudes implies that the TROPOMI tropospheric VCDs have a positive bias.

The OMI-TROPOMI biases do not appear to be consistent with the previously discovered negative bias of 20% to 30% in TROPOMI tropospheric VCDs relative to those of OMI for measurements from February to June 2018 (C. Wang et al., 2020) or the positive bias of approximately 5% in the geometric column densities, which are an approximation of the total column densities, in July 2018 (van Geffen et al., 2020). An analysis into the scenarios where there are differences in the OMI and TROPOMI datasets and into the causes of these differences would provide a better understanding of the limitations in using different instruments for the non-coincident limb-nadir matching method.

4.5 Conclusion and Future Work

The present chapter assessed the method by Adams et al. (2016) of estimating tropospheric NO₂ column densities by matching the stratospheric NO₂ column densities measured by a limb-viewing instrument to the combined troposphere-stratosphere NO₂ column densities measured by a nadir-viewing instrument and then subtracting the stratospheric column densities from the combined troposphere-stratosphere column densities. This method allows for the tropospheric concentration estimates to be dependent on highly-validated limb-viewing remote sensing instrument data instead of relying on chemical transport models or on assumptions about the distribution of atmospheric species. The present work has led to the development of a version 7 OSIRIS NO₂ number density profile dataset that shows agreement above the tropopause with the heritage, validated version 3 dataset within retrieval error bounds. However, the remaining biases in the non-coincident limb-nadir matching results suggest that more work is required to conclude the effectiveness of the method. This is discussed in more detail in Section 4.5.2.

4.5.1 Conclusion

The present chapter demonstrates agreement between the latest, version 7 OSIRIS NO₂ profile number densities and the validated version 3 data within the version 7 retrieval error bounds above the tropopause (Fig. 4.2). The bias in the version 7 profile number densities relative to version 3 profile number densities is on average 10%, but drops to 1% when only considering altitudes above 19 km. The version 7 data is expected to replace the current version 6 data as the standard, publicly available OSIRIS NO₂ product.

The non-coincident limb-nadir matching algorithm of the present work is validated against that by Adams et al. (2016) by comparing OSIRIS gridded stratospheric NO₂ VCD maps using the present algorithm to a sample of data from 4 March 2008, provided by Dr. Adams. This comparison shows less than 10% absolute bias in the OSIRIS gridded stratospheric NO₂ VCD maps of the present work relative to those of Adams et al. (2016) (top rows of Figs. 4.4 and 4.5). The algorithm of the present work is then used to reanalyze the OmO product

with newer OSIRIS, OMI, and photochemical box model data, and to analyze results with data from OSIRIS and TROPOMI, the OMI-successor instrument.

The overall positive bias in the OmO maps of the present work (Fig. 4.8), with version 7 OSIRIS NO₂ data, version 4 OMI-SP NO₂ data, and PRATMO⁺⁺, compared to those of Adams et al. (2016), with version 3 OSIRIS NO₂ data, version 2 OMI-SP NO₂ data, and PRATMO⁺, appear to be explained primarily by differences due to the photochemical box model input parameters (bottom rows of Figs. 4.4 and 4.5) and to differences between the version 4 and 2 OMI-SP NO₂ data (Fig. 4.6). For example, it is shown that up to approximately 0.5×10^{15} molecules/cm² of bias could be due to the photochemical box model parameters and up to roughly 0.2×10^{15} molecules/cm² due to the difference in OMI-SP NO₂ data version. Future work towards understanding these biases is detailed in Section 4.5.2.

It is shown that the OmO tropospheric VCDs over the Pacific Ocean are generally at or below the expected maximum values (Fig. 4.9) and that there is agreement between OmO and OMI tropospheric VCD trends in select regions (Fig. 4.10). This indicates overall agreement between the OmO VCDs and their expected values. These results, along with the convenience of taking advantage of separate, non-coincident limb- and nadir-viewing instruments, demonstrates the potential benefit of the non-coincident limb-nadir matching method in deriving tropospheric NO₂ pollution concentrations. Nonetheless, future work, discussed in Section 4.5.2, is recommended to better understand the constraints of the method.

Comparisons between OmO and TROPOMI results indicate that there may be a positive bias in the TROPOMI tropospheric and stratospheric VCDs relative to the corresponding OMI VCDs, with the bias independent of latitude. Existing TROPOMI-OMI comparisons (van Geffen et al., 2020; C. Wang et al., 2020) could be supplemented with future investigations into the temporal and spatial dependencies of the aforementioned VCD biases to uncover the limitations in using different instruments for the non-coincident limb-nadir matching technique.

4.5.2 Future Work

Future work towards the reanalysis of OSIRIS-OMI limb-nadir matching should include sensitivity studies to the photochemical box model input parameters and an analysis of the differences due to the OMI-SP data version. For the sensitivity study to photochemical box model input parameters, an error range for each input parameter would allow for an error range in the photochemical box model NO₂ number density to be determined, which in turn would give an error range in the final OmO tropospheric VCDs. To simplify the sensitivity study, the input parameters to be varied could be limited to those with the largest expected error ranges. For the analysis of the effect of the OMI-SP data version, an expected worst-case mean bias in the OmO tropospheric VCDs can be calculated by first estimating the worst-case mean bias in the tropospheric NO₂ VCDs, stratospheric NO₂ VCDs, tropospheric AMFs, and stratospheric AMFs due to using the OMI-SP version 4 dataset instead of the version 2 dataset.

Additionally, further analysis in the trends of individual regions is recommended to better understand yearly and spatial dependencies in the biases. Spatial dependency analyses would help explain if the 1×10^{15} molecules/cm² negative bias in the OmO tropospheric VCDs relative to the OMI tropospheric VCDs found in the Ohio River Valley and southwestern Pennsylvania is anomalous. Yearly dependency analyses over the years 2005 to present would help explain the larger OmO-OMI tropospheric VCD discrepancy in 2018 and 2019 compared to the years 2005 to 2017.

Future work towards the understanding of the OMI-TROPOMI biases should include investigations into latitude- and seasonal-dependencies of the tropospheric VCDs, stratospheric VCDs, tropospheric AMFs, and stratospheric AMFs. Moreover, the aforementioned analyses of the yearly dependencies in OMI data would help determine the degree to which OMI biases could be causing the OMI-TROPOMI biases.

5 Conclusion

5.1 Conclusions

The first goal of this thesis is to investigate the difference in ozone retrieval error associated with implementing a radiative transfer model with a more realistic geometry than the planned VLIDORT model to retrieve tropospheric ozone pollution concentrations over Canada using future measurements from the TEMPO instrument. The intention of this goal is to quantify potential benefits of implementing a radiative transfer model with a spherical geometry for all orders of scattering to retrieve ozone profiles over Canada with future TEMPO measurements compared to implementing the planned VLIDORT model, which assumes a plane-parallel Earth-atmosphere geometry for multiple-scattered light. This goal is addressed by comparing simulated-TEMPO ozone retrieval results using the SASKTRAN HR engine, with a spherical Earth-atmosphere geometry for all orders of scattering, to those using the SASKTRAN DO engine, with a plane-parallel Earth-atmosphere geometry for all orders of scattering. The second goal of this thesis is to assess the feasibility of using the non-coincident limb-nadir matching method to estimate tropospheric NO₂ densities (Adams et al., 2016) by reanalyzing OSIRIS-OMI results with newer NO₂ datasets and analyzing OSIRIS-TROPOMI results. Addressing this second goal led to the additional result of an improved OSIRIS level 2 NO₂ data product.

Towards the first goal, the comparisons herein show that the SASKTRAN DO engine (plane-parallel geometry) gives lower ozone retrieval error than the SASKTRAN HR engine (spherical geometry) for the high viewing zenith angles of Canadian measurements, especially for the high solar zenith angles of measurements near local sunset or sunrise. For simulated TEMPO measurements one hour past local sunrise, the ozone retrieval error for the DO en-

gine over the Canadian Oil Sands is shown to be up to 80% in December, up to 50% in June, and up to 25% in March or September. For simulated TEMPO measurements at 13:00 local time, the ozone retrieval error for the DO engine over the Canadian Oil Sands is shown to be up to 15%. In all cases, the ozone retrieval error for the HR engine is up to one order of magnitude smaller than that of the DO engine. Although the VLIDORT model planned for future TEMPO ozone retrievals assumes a spherical Earth-atmosphere geometry up to the single-scattered light and a plane-parallel geometry for higher-order scattering, the present results demonstrate the potential benefits of using a radiative transfer model with a more realistic geometry for all orders of scattering instead of the planned VLIDORT model to retrieve tropospheric ozone with future TEMPO measurements for the purpose of Canadian air quality forecasting.

The work towards the second goal elucidated the application of non-coincident limb-nadir matching to the monitoring of tropospheric pollutants, and there is further potential application for this method given the quantity of limb- and nadir-viewing instruments in operation. However, more work is needed to further assess the limitations of the method and analyze possible constraints when applied to other instruments.

Comparisons between versions 3 and 6 OSIRIS NO₂ profile data show a negative bias in the version 6 data. Consequent modifications to the OSIRIS NO₂ retrieval algorithm by the Atmospheric Research Group at the University of Saskatchewan has resulted in a newer version 7 data product which agrees with the highly-validated version 3 data within the version 7 retrieval error bounds. The version 7 data product is expected to replace the current publicly available version 6 data product.

The reanalysis of Adams et al. (2016) OSIRIS-OMI limb-nadir matching with the newer version 7 OSIRIS NO₂ data, the newer version 4 OMI-SP NO₂ data, and the photochemical box model NO₂ dataset with different input parameters shows a positive bias of up to approximately 0.2×10^{15} molecules/cm² in the version 4 OMI-SP stratospheric NO₂ VCDs relative to those of version 2 and a negative bias of up to roughly 0.5×10^{15} molecules/cm² in the OSIRIS stratospheric NO₂ VCDs due to the photochemical box model input parameters.

The OMI-SP stratospheric VCD bias is largest closer to the equator.

The average positive bias of approximately 0.5×10^{15} molecules/cm² in the TROPomO tropospheric VCDs relative to those of OmO is found to be caused by TROPOMI-OMI tropospheric and stratospheric VCD biases. The tropospheric VCD bias is greater than the stratospheric VCD bias, but the stratosphere-to-troposphere AMF ratio results in the two having equal contributions to the TROPomO-OmO tropospheric VCD bias.

5.2 Future Work

Future work towards the first goal includes analyses of the effects of the radiative transfer model geometric assumptions on different orders of scattering. This would serve to better understand the differences in future TEMPO ozone retrievals over Canada between using a radiative transfer model like the SASKTRAN HR engine and using one like VLIDORT that is planned to be used for the TEMPO retrievals. The present work also suggests the value in a comparison of retrieval results between using a radiative transfer model like the SASKTRAN HR engine and using the actual VLIDORT model. Furthermore, an investigation of the effect of measurement noise on the simulated-TEMPO ozone retrievals would provide a more thorough assessment of the best radiative transfer model for future TEMPO ozone pollution retrievals over Canada.

Future work towards the second goal includes sensitivity studies to the variations due to the photochemical box model input parameters, analyses of the biases between OMI-SP data versions, further analyses in spatial and yearly dependencies of the OmO-OMI biases, and studies into latitudinal and seasonal dependencies of the OMI-TROPOMI biases. Error range estimates of the photochemical box model input parameters would provide a measure of corresponding error ranges in both the photochemical box model NO₂ densities and the final tropospheric NO₂ densities resulting from the non-coincident limb-nadir matching. Worst-case mean bias estimates of the OMI tropospheric and stratospheric VCDs and AMFs due to the OMI-SP data version would provide a projection of the worst-case mean bias in the final tropospheric VCDs resulting from the non-coincident limb-nadir matching. The estimates of

biases in the OmO and TROPomO tropospheric VCDs resulting from photochemical box model input parameters and the OMI-SP data version would help ascertain the limitations of the non-coincident limb-nadir matching method.

Analyses of the spatial dependencies of OmO tropospheric VCDs would help explain the anomalous 1×10^{15} molecules/cm² negative bias in the OmO tropospheric VCDs relative to the OMI tropospheric VCDs found in the Ohio River Valley and southwestern Pennsylvania. Investigations of the yearly dependencies of OmO tropospheric VCDs from 2005 to the present would aid in understanding the larger discrepancy between OmO and OMI tropospheric VCDs in 2018 and 2019 compared to the years 2005 to 2017. Finally, latitudinal and seasonal dependencies in the bias between OMI and TROPOMI tropospheric and stratospheric VCDs and AMFs would further explain the demonstrated OmO-TROPomO biases and increase the understanding of possible limitations in applying the non-coincident limb-nadir matching technique with different instruments.

References

- Adams, C., Strong, K., Batchelor, R. L., Bernath, P. F., Brohede, S., Boone, C., . . . Zhao, X. (2012). Validation of ACE and OSIRIS ozone and NO₂ measurements using ground-based instruments at 80° N. *Atmospheric Measurement Techniques*, 5(5), 927–953. <https://doi.org/10.5194/amt-5-927-2012>
- Adams, C., Normand, E. N., McLinden, C. A., Bourassa, A. E., Lloyd, N. D., Degenstein, D. A., . . . Eskes, H. J. (2016). Limb–nadir matching using non-coincident NO₂ observations: Proof of concept and the OMI-minus-OSIRIS prototype product. *Atmospheric Measurement Techniques*, 9(8), 4103–4122. <https://doi.org/10.5194/amt-9-4103-2016>
- Bates, D. R. (1984). Rayleigh scattering by air. *Planetary and Space Science*, 32(6), 785–790. [https://doi.org/10.1016/0032-0633\(84\)90102-8](https://doi.org/10.1016/0032-0633(84)90102-8)
- Bates, S. (2021). Reduced African Grassland Fires Contribute to Air Quality Improvements. NASA. Retrieved March 30, 2021, from <http://www.nasa.gov/feature/esnt/2021/nasa-study-finds-reduced-african-grassland-fires-contribute-to-short-lived-air-quality>
- Beirle, S., Köhl, S., Pukite, J., & Wagner, T. (2010). Retrieval of tropospheric column densities of NO₂ from combined SCIAMACHY nadir/limb measurements. *Atmospheric Measurement Techniques*, 3(1), 283–299. <https://doi.org/10.5194/amt-3-283-2010>
- Belmonte Rivas, M., Veeckind, P., Eskes, H., & Levelt, P. (2015). OMI tropospheric NO₂ profiles from cloud slicing: Constraints on surface emissions, convective transport and lightning NO_x. *Atmospheric Chemistry and Physics*, 15(23), 13519–13553. <https://doi.org/10.5194/acp-15-13519-2015>
- Boersma, K. F., Eskes, H. J., Veeckind, J. P., Brinksma, E. J., van der A, R. J., Sneep, M., . . . Bucsela, E. J. (2007). Near-real time retrieval of tropospheric NO₂ from OMI. *Atmospheric Chemistry and Physics*, 7(8), 2103–2118. Retrieved August 21, 2020, from <https://hal.archives-ouvertes.fr/hal-00296205>
- Boningari, T., & Smirniotis, P. G. (2016). Impact of nitrogen oxides on the environment and human health: Mn-based materials for the NO_x abatement. *Current Opinion in Chemical Engineering*, 13, 133–141. <https://doi.org/10.1016/j.coche.2016.09.004>
- Bourassa, A. E., Degenstein, D. A., & Llewellyn, E. J. (2008). SASKTRAN: A spherical geometry radiative transfer code for efficient estimation of limb scattered sunlight. *Journal of Quantitative Spectroscopy and Radiative Transfer*, 109(1), 52–73. <https://doi.org/10.1016/j.jqsrt.2007.07.007>
- Brewer, A. W., Mcelroy, C. T., & Kerr, J. B. (1973). Nitrogen Dioxide Concentrations in the Atmosphere. *Nature*, 246(5429), 129–133. <https://doi.org/10.1038/246129a0>
- Brion, J., Chakir, A., Charbonnier, J., Daumont, D., Parisse, C., & Malicet, J. (1998). Absorption Spectra Measurements for the Ozone Molecule in the 350–830 nm Region.

- Journal of Atmospheric Chemistry*, 30(2), 291–299. <https://doi.org/10.1023/A:1006036924364>
- Brion, J., Chakir, A., Daumont, D., Malicet, J., & Parisse, C. (1993). High-resolution laboratory absorption cross section of O₃. Temperature effect. *Chemical Physics Letters*, 213(5), 610–612. [https://doi.org/10.1016/0009-2614\(93\)89169-I](https://doi.org/10.1016/0009-2614(93)89169-I)
- Brohede, S. M., Haley, C., McLinden, C., Sioris, C., Murtagh, D., V. Petelina, S., . . . Taha, G. (2007). Validation of Odin/OSIRIS stratospheric NO₂ profiles. *Journal of Geophysical Research*, 112. <https://doi.org/10.1029/2006JD007586>
- Brohede, S. M., McLinden, C. A., Urban, J., Haley, C. S., Jonsson, A. I., & Murtagh, D. (2008). Odin stratospheric proxy NO_y measurements and climatology. *Atmospheric Chemistry and Physics*, 8(19), 5731–5754. <https://doi.org/10.5194/acp-8-5731-2008>
- Broman, L., Gumbel, J., & Christensen, O. M. (2021). New insights on polar mesospheric cloud particle size distributions from a two-satellite common volume study. *Journal of Atmospheric and Solar-Terrestrial Physics*, 105594. <https://doi.org/10.1016/j.jastp.2021.105594>
- Bucsela, E. J., Krotkov, N. A., Celarier, E. A., Lamsal, L. N., Swartz, W. H., Bhartia, P. K., . . . Pickering, K. E. (2013a). A new stratospheric and tropospheric NO₂ retrieval algorithm for nadir-viewing satellite instruments: Applications to OMI. *Atmospheric Measurement Techniques*, 6(10), 2607–2626. <https://doi.org/10.5194/amt-6-2607-2013>
- Bucsela, E. J., Krotkov, N. A., Celarier, E. A., Lamsal, L. N., Swartz, W. H., Bhartia, P. K., . . . Pickering, K. E. (2013b). A new stratospheric and tropospheric NO₂ retrieval algorithm for nadir-viewing satellite instruments: Applications to OMI. *Atmospheric Measurement Techniques*, 6(10), 2607–2626. <https://doi.org/10.5194/amt-6-2607-2013>
- Bucsela, E. J., Celarier, E., Wenig, M., Gleason, J., Veefkind, J., Boersma, K., & Brinksma, E. (2006). Algorithm for NO₂ vertical column retrieval from the Ozone Monitoring Instrument. *Geoscience and Remote Sensing, IEEE Transactions on*, 44, 1245–1258. <https://doi.org/10.1109/TGRS.2005.863715>
- Bucsela, E. J., Celarier, E. A., Gleason, J. L., Krotkov, N. A., Lamsal, L. N., Marchenko, S. V., & Swartz, W. H. (2016). *OMNO₂ README Document Data Product Version 3.0*. NASA. NASA.
- Burrows, J. P., Hölzle, E., Goede, A. P. H., Visser, H., & Fricke, W. (1995). SCIAMACHY—scanning imaging absorption spectrometer for atmospheric cartography. *Acta Astronautica*, 35(7), 445–451. [https://doi.org/10.1016/0094-5765\(94\)00278-T](https://doi.org/10.1016/0094-5765(94)00278-T)
- Burrows, J. P., Weber, M., Buchwitz, M., Rozanov, V., Ladstätter-Weißmayer, A., Richter, A., . . . Perner, D. (1999). The Global Ozone Monitoring Experiment (GOME): Mission Concept and First Scientific Results. *Journal of the Atmospheric Sciences*, 56(2), 151–175. [https://doi.org/10.1175/1520-0469\(1999\)056<0151:TGOMEG>2.0.CO;2](https://doi.org/10.1175/1520-0469(1999)056<0151:TGOMEG>2.0.CO;2)
- Chaloulakou, A., Mavroidis, I., & Gavriil, I. (2008). Compliance with the annual NO₂ air quality standard in Athens. Required NO_x levels and expected health implications. *Atmospheric Environment*, 42(3), 454–465. <https://doi.org/10.1016/j.atmosenv.2007.09.067>
- Chameides, W. L. (1978). The photochemical role of tropospheric nitrogen oxides. *Geophysical Research Letters*, 5(1), 17–20. <https://doi.org/10.1029/GL005i001p00017>

- Chance, K. V., & Spurr, R. J. D. (1997). Ring effect studies: Rayleigh scattering, including molecular parameters for rotational Raman scattering, and the Fraunhofer spectrum. *Applied Optics*, *36*(21), 5224–5230. <https://doi.org/10.1364/AO.36.005224>
- Chehade, W., Weber, M., & Burrows, J. P. (2014). Total ozone trends and variability during 1979–2012 from merged data sets of various satellites. *Atmospheric Chemistry and Physics*, *14*(13), 7059–7074. <https://doi.org/10.5194/acp-14-7059-2014>
- Choi, S., Joiner, J., Choi, Y., Duncan, B. N., Vasilkov, A., Krotkov, N., & Bucsela, E. J. (2014). First estimates of global free-tropospheric NO₂ abundances derived using a cloud-slicing technique applied to satellite observations from the Aura Ozone Monitoring Instrument (OMI). *Atmospheric Chemistry and Physics*, *14*(19), 10565–10588. <https://doi.org/10.5194/acp-14-10565-2014>
- Daumont, D., Brion, J., Charbonnier, J., & Malicet, J. (1992). Ozone UV spectroscopy I: Absorption cross-sections at room temperature. *Journal of Atmospheric Chemistry*, *15*(2), 145–155. <https://doi.org/10.1007/BF00053756>
- Degenstein, D. A., Bourassa, A. E., Roth, C. Z., & Llewellyn, E. J. (2009). Limb scatter ozone retrieval from 10 to 60 km using a multiplicative algebraic reconstruction technique. *Atmospheric Chemistry and Physics*, *9*(17), 6521–6529. <https://doi.org/10.5194/acp-9-6521-2009>
- Dubé, K., Bourassa, A., Zawada, D., Degenstein, D., Damadeo, R., Flittner, D., & Randel, W. (2021). Accounting for the photochemical variation in stratospheric NO₂ in the SAGE III/ISS solar occultation retrieval. *Atmospheric Measurement Techniques*, *14*(1), 557–566. <https://doi.org/10.5194/amt-14-557-2021>
- Ehhalt, D., Prather, M., Dentener, F., Derwent, R., Dlugokencky, E., Holland, E., ... McFarland, M. (2001). Atmospheric Chemistry and Greenhouse Gases. *Climate Change 2001: The Scientific Basis. Contributions of Working Group I to the Third Assessment Report of the Intergovernmental Panel on Climate Change* (p. 881). Cambridge University Press. <https://www.ipcc.ch/report/ar3/wg1/chapter-4-atmospheric-chemistry-and-greenhouse-gases/>
- Fabry, C., & Buisson, H. (1921). A Study of the Ultra-Violet End of the Solar Spectrum. *Astrophysical Journal*, *54*(5), 297–322. <https://doi.org/10.1086/142647>
- van Geffen, J. H. G. M., Boersma, K. F., Eskes, H. J., Sneep, M., Linden, M. T., Zara, M., & Veefkind, J. P. (2020). S5P TROPOMI NO₂ slant column retrieval : Method, stability, uncertainties and comparisons with OMI. *Atmospheric Measurement Techniques*, *13*(3), 1315–1335. <https://doi.org/10.5194/amt-13-1315-2020>
- van Geffen, J. H. G. M., Eskes, H. J., Boersma, K. F., Maasakkers, J. D., & Veefkind, J. P. (2019). *TROPOMI ATBD of the total and tropospheric NO₂ data products*. Royal Netherlands Meteorological Institute.
- Grainger, J. F., & Ring, J. (1962). Anomalous Fraunhofer Line Profiles. *Nature*, *193*(4817), 762–762. <https://doi.org/10.1038/193762a0>
- Greenblatt, G. D., & Ravishankara, A. R. (1990). Laboratory studies on the stratospheric NO_x production rate. *Journal of Geophysical Research: Atmospheres*, *95*(D4), 3539–3547. <https://doi.org/10.1029/JD095iD04p03539>
- Haley, C. S., & Brohede, S. M. (2007). Status of the Odin/OSIRIS stratospheric O₃ and NO₂ data products. *Canadian Journal of Physics*, *85*(11), 1177–1194. <https://doi.org/10.1139/p07-114>

- Haley, C. S., Brohede, S. M., Sioris, C. E., Griffioen, E., Murtagh, D. P., McDade, I. C., ... Goutail, F. (2004). Retrieval of stratospheric O₃ and NO₂ profiles from Odin Optical Spectrograph and Infrared Imager System (OSIRIS) limb-scattered sunlight measurements. *Journal of Geophysical Research: Atmospheres*, *109*(D16). <https://doi.org/10.1029/2004JD004588>
- Hansen, J. E., & Travis, L. D. (1974). Light scattering in planetary atmospheres. *Space Science Reviews*, *16*(4), 527–610. <https://doi.org/10.1007/BF00168069>
- Heath, D. F., Mateer, C. L., & Krueger, A. J. (1973). The Nimbus-4 Backscatter Ultraviolet (BUV) atmospheric ozone experiment — tow years' operation. *Pure and Applied Geophysics*, *106*(1), 1238–1253. <https://doi.org/10.1007/BF00881076>
- Hedin, A. E. (1991). Extension of the MSIS Thermosphere Model into the middle and lower atmosphere. *Journal of Geophysical Research: Space Physics*, *96*(A2), 1159–1172. <https://doi.org/10.1029/90JA02125>
- Hendrick, F., van Roozendaal, M., Kylling, A., Petritoli, A., Rozanov, A., Sanghavi, S., ... De Maziere, M. (2006). Intercomparison exercise between different radiative transfer models used for the interpretation of ground-based zenith-sky and multi-axis DOAS observations. *Atmospheric Chemistry and Physics*, *6*. <https://doi.org/10.5194/acpd-5-7929-2005>
- Hilboll, A., Richter, A., Rozanov, A., Hodnebrog, Ø., Heckel, A., Solberg, S., ... Burrows, J. P. (2013). Improvements to the retrieval of tropospheric NO₂ from satellite - stratospheric correction using SCIAMACHY limb/nadir matching and comparison to Oslo CTM2 simulations. *Atmospheric Measurement Techniques*, *6*(3), 565–584. <https://doi.org/10.5194/amt-6-565-2013>
- Hoogen, R., Rozanov, V. V., & Burrows, J. P. (1999). Ozone profiles from GOME satellite data: Algorithm description and first validation. *Journal of Geophysical Research: Atmospheres*, *104*(D7), 8263–8280. <https://doi.org/10.1029/1998JD100093>
- Hou, W., Wang, J., Xu, X., Reid, J. S., Janz, S. J., & Leitch, J. W. (2020). An algorithm for hyperspectral remote sensing of aerosols: 3. Application to the GEO-TASO data in KORUS-AQ field campaign. *Journal of Quantitative Spectroscopy and Radiative Transfer*, *253*, 107161. <https://doi.org/10.1016/j.jqsrt.2020.107161>
- van de Hulst, H. C. (1948). Scattering in a Planetary Atmosphere. *The Astrophysical Journal*, *107*, 220. <https://doi.org/10.1086/145005>
- Jaeglé, L., Webster, C. R., May, R. D., Fahey, D. W., Woodbridge, E. L., Keim, E. R., ... Pfister, L. (1994). In situ measurements of the NO₂/NO ratio for testing atmospheric photochemical models. *Geophysical Research Letters*, *21*(23), 2555–2558. <https://doi.org/10.1029/94GL02717>
- Jaeglé, L., Steinberger, L., V. Martin, R., & Chance, K. (2005). Global partitioning of NO_x sources using satellite observations: Relative roles of fossil fuel combustion, biomass burning and soil emissions. *Faraday Discussions*, *130*(0), 407–423. <https://doi.org/10.1039/B502128F>
- Joiner, J., & Vasilkov, A. P. (2006). First results from the OMI rotational Raman scattering cloud pressure algorithm. *IEEE Transactions on Geoscience and Remote Sensing*, *44*(5), 1272–1282. <https://doi.org/10.1109/TGRS.2005.861385>
- Kalnay, E., Kanamitsu, M., Kistler, R., Collins, W., Deaven, D., Gandin, L., ... Joseph, D. (1996). The NCEP/NCAR 40-Year Reanalysis Project. *Bulletin of the American*

- Meteorological Society*, 77, 437–472. [https://doi.org/10.1175/1520-0477\(1996\)077<0437:TNYRP>2.0.CO;2](https://doi.org/10.1175/1520-0477(1996)077<0437:TNYRP>2.0.CO;2)
- Krotkov, N. A., Lamsal, L. N., Celarier, E. A., Swartz, W. H., Marchenko, S. V., Bucsela, E. J., ... Zara, M. (2017). The version 3 OMI NO₂ standard product. *Atmospheric Measurement Techniques*, 10(9), 3133–3149. <https://doi.org/10.5194/amt-10-3133-2017>
- Krotkov, N. A., McLinden, C. A., Li, C., Lamsal, L. N., Celarier, E. A., Marchenko, S. V., ... Streets, D. G. (2016). Aura OMI observations of regional SO₂ and NO₂ pollution changes from 2005 to 2015. *Atmospheric Chemistry and Physics*, 16(7), 4605–4629. <https://doi.org/omi>
- Lamsal, L. N., Krotkov, N. A., Vasilkov, A., Marchenko, S., Qin, W., Yang, E.-S., ... Bucsela, E. (2021). Ozone Monitoring Instrument (OMI) Aura nitrogen dioxide standard product version 4.0 with improved surface and cloud treatments. *Atmospheric Measurement Techniques*, 14(1), 455–479. <https://doi.org/10.5194/amt-14-455-2021>
- Last, J. A., Sun, W. M., & Witschi, H. (1994). Ozone, NO, and NO₂: Oxidant air pollutants and more. *Environmental Health Perspectives*, 102(suppl 10), 179–184. <https://doi.org/10.1289/ehp.94102s10179>
- Lelieveld, J., & Dentener, F. J. (2000). What controls tropospheric ozone? *Journal of Geophysical Research: Atmospheres*, 105(D3), 3531–3551. <https://doi.org/10.1029/1999JD901011>
- Leue, C., Wenig, M., Wagner, T., Klimm, O., Platt, U., & Jähne, B. (2001). Quantitative analysis of NO_x emissions from Global Ozone Monitoring Experiment satellite image sequences. *Journal of Geophysical Research: Atmospheres*, 106(D6), 5493–5505. <https://doi.org/10.1029/2000JD900572>
- Levelt, P. F., van den Oord, G. H. J., Dobber, M., Malkki, A., Visser, H., de Vries, J., ... Saari, H. (2006). The ozone monitoring instrument. *IEEE Transactions on Geoscience and Remote Sensing*, 44(5), 1093–1101. <https://doi.org/10.1109/TGRS.2006.872333>
- Liu, X., Bhartia, P. K., Chance, K., Spurr, R. J. D., & Kurosu, T. P. (2010). Ozone profile retrievals from the Ozone Monitoring Instrument. *Atmospheric Chemistry and Physics*, 10(5), 2521–2537. <https://doi.org/10.5194/acp-10-2521-2010>
- Liu, X., Chance, K., Sioris, C. E., Spurr, R. J. D., Kurosu, T. P., Martin, R. V., & Newchurch, M. J. (2005). Ozone profile and tropospheric ozone retrievals from the Global Ozone Monitoring Experiment: Algorithm description and validation. *Journal of Geophysical Research: Atmospheres*, 110(D20). <https://doi.org/10.1029/2005JD006240>
- Liu, X., Chance, K., Abad, G. G., Houck, J., Bak, J., Chan Miller, C., ... Suleiman, R. (2020). *TEMPO Algorithms* (Science team presentation). Retrieved January 15, 2021, from <http://tempo.si.edu/presentations.html>
- Llewellyn, E. J., Lloyd, N. D., Degenstein, D. A., Gattinger, R. L., Petelina, S. V., Bourassa, A. E., ... Nordh, L. (2004). The OSIRIS instrument on the Odin spacecraft. *Canadian Journal of Physics*, 82(6), 411–422. <https://doi.org/10.1139/p04-005>
- Lorente, A., Borsdorff, T., Butz, A., Hasekamp, O., aan de Brugh, J., Schneider, A., ... Landgraf, J. (2021). Methane retrieved from TROPOMI: Improvement of the data product and validation of the first 2 years of measurements. *Atmospheric Measurement Techniques*, 14(1), 665–684. <https://doi.org/10.5194/amt-14-665-2021>

- Malicet, J., Daumont, D., Charbonnier, J., Parisse, C., Chakir, A., & Brion, J. (1995). Ozone UV spectroscopy. II. Absorption cross-sections and temperature dependence. *Journal of Atmospheric Chemistry*, *21*(3), 263–273. <https://doi.org/10.1007/BF00696758>
- Marchenko, S., Krotkov, N. A., Lamsal, L. N., Celarier, E. A., Swartz, W. H., & Bucsela, E. J. (2015). Revising the slant column density retrieval of nitrogen dioxide observed by the Ozone Monitoring Instrument. *Journal of Geophysical Research: Atmospheres*, *120*(11), 5670–5692. <https://doi.org/10.1002/2014JD022913>
- Martin, R. V., Chance, K., Jacob, D. J., Kurosu, T. P., Spurr, R. J. D., Bucsela, E. J., . . . Koелеmeijer, R. B. A. (2002). An improved retrieval of tropospheric nitrogen dioxide from GOME. *Journal of Geophysical Research: Atmospheres*, *107*(D20), ACH 9-1-ACH 9–21. <https://doi.org/10.1029/2001JD001027>
- Mayer, H. (1999). Air pollution in cities. *Atmospheric Environment*, *33*(24), 4029–4037. [https://doi.org/10.1016/S1352-2310\(99\)00144-2](https://doi.org/10.1016/S1352-2310(99)00144-2)
- McLinden, C. A., Haley, C. S., & Sioris, C. E. (2006). Diurnal effects in limb scatter observations. *Journal of Geophysical Research: Atmospheres*, *111*(D14). <https://doi.org/10.1029/2005JD006628>
- McPeters, R. D., Labow, G. J., & Johnson, B. J. (1997). A satellite-derived ozone climatology for balloonsonde estimation of total column ozone. *Journal of Geophysical Research: Atmospheres*, *102*(D7), 8875–8885. <https://doi.org/10.1029/96JD02977>
- Musselman, R. C., & Massman, W. J. (1998). Ozone flux to vegetation and its relationship to plant response and ambient air quality standards. *Atmospheric Environment*, *33*(1), 65–73. [https://doi.org/10.1016/S1352-2310\(98\)00127-7](https://doi.org/10.1016/S1352-2310(98)00127-7)
- Peat, C. (n.d.). *AURA - Orbit*. Retrieved April 3, 2021, from <https://www.heavens-above.com/orbit.aspx?satid=28376&lat=0&lng=0&loc=Unspecified&alt=0&tz=CET&cul=en>
- Platt, U., & Stutz, J. (2008). Scattered-light DOAS Measurements. In U. Platt & J. Stutz (Eds.), *Differential Optical Absorption Spectroscopy: Principles and Applications* (pp. 329–377). Springer. https://doi.org/10.1007/978-3-540-75776-4_9
- Prather, M., & Jaffe, A. H. (1990). Global impact of the Antarctic ozone hole: Chemical propagation. *Journal of Geophysical Research*, *95*(D4), 3473. <https://doi.org/10.1029/JD095iD04p03473>
- Richter, A., & Burrows, J. P. (2002). Tropospheric NO₂ from GOME measurements. *Advances in Space Research*, *29*(11), 1673–1683. [https://doi.org/10.1016/S0273-1177\(02\)00100-X](https://doi.org/10.1016/S0273-1177(02)00100-X)
- Riebeek, H. (2009). *Catalog of Earth Satellite Orbits*. Retrieved August 14, 2020, from <https://earthobservatory.nasa.gov/features/OrbitsCatalog>
- Rodgers, C. D. (2000). *Inverse Methods for Atmospheric Sounding: Theory and Practice*. World Scientific.
- Rozanov, V. V., Diebel, D., Spurr, R. J. D., & Burrows, J. P. (1997). GOMETRAN: A radiative transfer model for the satellite project GOME, the plane-parallel version. *Journal of Geophysical Research: Atmospheres*, *102*(D14), 16683–16695. <https://doi.org/10.1029/96JD01535>
- Singer, S. F., & Wentworth, R. C. (1957). A method for the determination of the vertical ozone distribution from a satellite. *Journal of Geophysical Research (1896-1977)*, *62*(2), 299–308. <https://doi.org/10.1029/JZ062i002p00299>

- Sioris, C. E., Kurosu, T. P., Martin, R. V., & Chance, K. (2004). Stratospheric and tropospheric NO₂ observed by SCIAMACHY: First results. *Advances in Space Research*, *34*(4), 780–785. <https://doi.org/10.1016/j.asr.2003.08.066>
- Sioris, C. E., Rieger, L. A., Lloyd, N. D., Bourassa, A. E., Roth, C. Z., Degenstein, D. A., ... McLinden, C. A. (2017). Improved OSIRIS NO₂ retrieval algorithm: Description and validation. *Atmospheric Measurement Techniques*, *10*, 1155–1168. <https://doi.org/10.5194/amt-10-1155-2017>
- Spurr, R. J. D. (2006). VLIDORT: A linearized pseudo-spherical vector discrete ordinate radiative transfer code for forward model and retrieval studies in multilayer multiple scattering media. *Journal of Quantitative Spectroscopy and Radiative Transfer*, *102*(2), 316–342. <https://doi.org/10.1016/j.jqsrt.2006.05.005>
- Spurr, R. J. D., Kurosu, T., Chance, K., Oss, R., Stammes, P., Kelder, H., ... Stammes, K. (2001). The Lidort Package: A Generic Forward-Model Radiative Transfer Tool For The Simultaneous Generation Of Intensities And Weighting Functions For Atmospheric Retrieval. *European Space Agency, (Special Publication) ESA SP*.
- Tai, A. P. K., Martin, M. V., & Heald, C. L. (2014). Threat to future global food security from climate change and ozone air pollution. *Nature Climate Change*, *4*(9), 817–821. <https://doi.org/10.1038/nclimate2317>
- Valks, P., Pinardi, G., Richter, A., Lambert, J.-C., Hao, N., Loyola, D., ... Emmadi, S. (2011). Operational total and tropospheric NO₂ column retrieval for GOME-2. *Atmospheric Measurement Techniques*, *4*(7), 1491–1514. <https://doi.org/10.5194/amt-4-1491-2011>
- Vandaele, A. C., Hermans, C., Simon, P. C., Carleer, M., Colin, R., Fally, S., ... Coquart, B. (1998). Measurements of the NO₂ absorption cross-section from 42 000 cm⁻¹ to 10 000 cm⁻¹ (238–1000 nm) at 220 K and 294 K. *Journal of Quantitative Spectroscopy and Radiative Transfer*, *59*(3), 171–184. [https://doi.org/10.1016/S0022-4073\(97\)00168-4](https://doi.org/10.1016/S0022-4073(97)00168-4)
- Veefkind, J. P., Aben, I., McMullan, K., Förster, H., de Vries, J., Otter, G., ... Levelt, P. F. (2012). TROPOMI on the ESA Sentinel-5 Precursor: A GMES mission for global observations of the atmospheric composition for climate, air quality and ozone layer applications. *Remote Sensing of Environment*, *120*, 70–83. <https://doi.org/10.1016/j.rse.2011.09.027>
- Vountas, M., Rozanov, V. V., & Burrows, J. P. (1998). RING EFFECT: IMPACT OF ROTATIONAL RAMAN SCATTERING ON RADIATIVE TRANSFER IN EARTH'S ATMOSPHERE. *Journal of Quantitative Spectroscopy and Radiative Transfer*, *60*(6), 943–961. [https://doi.org/10.1016/S0022-4073\(97\)00186-6](https://doi.org/10.1016/S0022-4073(97)00186-6)
- Wallace, J. M., & Hobbs, P. V. (2006). 1 - Introduction and Overview. In J. M. Wallace & P. V. Hobbs (Eds.), *Atmospheric Science (Second Edition)* (pp. 1–23). Academic Press. <https://doi.org/10.1016/B978-0-12-732951-2.50006-5>
- Wang, C., Wang, T., Wang, P., & Rakitin, V. (2020). Comparison and Validation of TROPOMI and OMI NO₂ Observations over China. *Atmosphere*, *11*(6), 636. <https://doi.org/10.3390/atmos11060636>
- Wang, W., Cheng, T., van der A, R. J., de Laat, J., & Williams, J. E. (2021). Verification of the Atmospheric Infrared Sounder (AIRS) and the Microwave Limb Sounder (MLS) ozone algorithms based on retrieved daytime and night-time ozone. *Atmospheric Measurement Techniques*, *14*(2), 1673–1687. <https://doi.org/10.5194/amt-14-1673-2021>

- Waters, J., Froidevaux, L., Harwood, R., Jarnot, R., Pickett, H., Read, W., . . . Walch, M. (2006). The Earth observing system microwave limb sounder (EOS MLS) on the aura Satellite. *IEEE Transactions on Geoscience and Remote Sensing*, *44*(5), 1075–1092. <https://doi.org/10.1109/TGRS.2006.873771>
- Wennberg, P. O., Cohen, R. C., Stimpfle, R. M., Koplow, J. P., Anderson, J. G., Salawitch, R. J., . . . Wofsy, S. C. (1994). Removal of Stratospheric O₃ by Radicals: In Situ Measurements of OH, HO₂, NO, NO₂, ClO, and BrO. *Science*, *266*(5184), 398–404. <https://doi.org/10.1126/science.266.5184.398>
- Williams, E. J., Parrish, D. D., & Fehsenfeld, F. C. (1987). Determination of nitrogen oxide emissions from soils: Results from a grassland site in Colorado, United States. *Journal of Geophysical Research: Atmospheres*, *92*(D2), 2173–2179. <https://doi.org/10.1029/JD092iD02p02173>
- Zawada, D. J., Dueck, S. R., Rieger, L. A., Bourassa, A. E., Lloyd, N. D., & Degenstein, D. A. (2015). High-resolution and Monte Carlo additions to the SASKTRAN radiative transfer model. *Atmospheric Measurement Techniques*, *8*(6), 2609–2623. <https://doi.org/10.5194/amt-8-2609-2015>
- Zoogman, P., Liu, X., Suleiman, R. M., Pennington, W. F., Flittner, D. E., Al-Saadi, J. A., . . . Chance, K. (2017). Tropospheric emissions: Monitoring of pollution (TEMPO). *Journal of Quantitative Spectroscopy and Radiative Transfer*, *186*, 17–39. <https://doi.org/10.1016/j.jqsrt.2016.05.008>

Appendix A

Maximum Latitude Difference Between TEMPO Line of Sight Intersections with Atmospheric Layers

Consider the TEMPO instrument, above the equator, pointed towards the Canadian Oil Sands (57°N). This is illustrated in Fig. A.1, with the Earth approximated as a sphere and with certain lengths and angles exaggerated for demonstration purposes. The radius of the spherical Earth is taken as the average Earth radius, $R_0 = 6\,371$ km, the distance from TEMPO to the center of the Earth is taken as $r_{\text{sat}} = 42\,157$ km ($R_0 + 35\,786$ km), and the latitude of the intersection between the TEMPO line of sight (LOS) and the ground is taken as $\phi_0 = 57^\circ$. The latitude of the surface of the Earth directly below the intersection between the TEMPO LOS and the 80-km-altitude atmospheric layer is denoted by ϕ_{80} , the angle between the TEMPO LOS and the line from the center of the Earth to the LOS-ground intersection is denoted by β_0 , and the angle between the TEMPO LOS and the line from the center of the Earth to the LOS-80-km-altitude intersection is denoted by β_{80} .

Note that the highest latitude where the LOS of TEMPO intersects the surface of the Earth tangentially is

$$\phi_{\text{tan}} = \arccos\left(\frac{R_0}{r_{\text{sat}}}\right) \approx 81.308^\circ. \quad (\text{A.1})$$

Thus, as $\phi_{80} < \phi_0 < 81.308^\circ$, both β_0 and β_{80} must be greater than 90° .

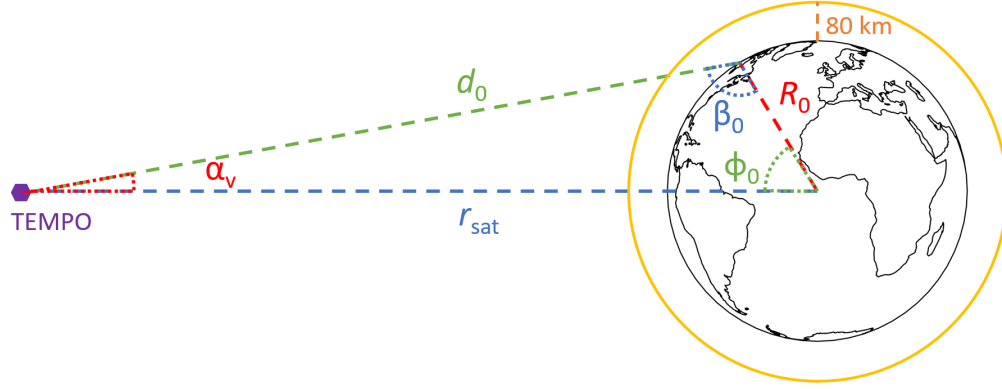
The distance from TEMPO to the LOS-ground intersection, d_0 , is found using the cosine law with the triangle formed between TEMPO, the center of the Earth, and the LOS-ground intersection (Fig. A.1(a)). This is given by

$$\begin{aligned} d_0 &= \left(r_{\text{sat}}^2 + R_0^2 - 2 \cdot r_{\text{sat}} \cdot R_0 \cos \phi_0\right)^{0.5} \\ &\approx 39\,054.34 \text{ km}. \end{aligned} \quad (\text{A.2})$$

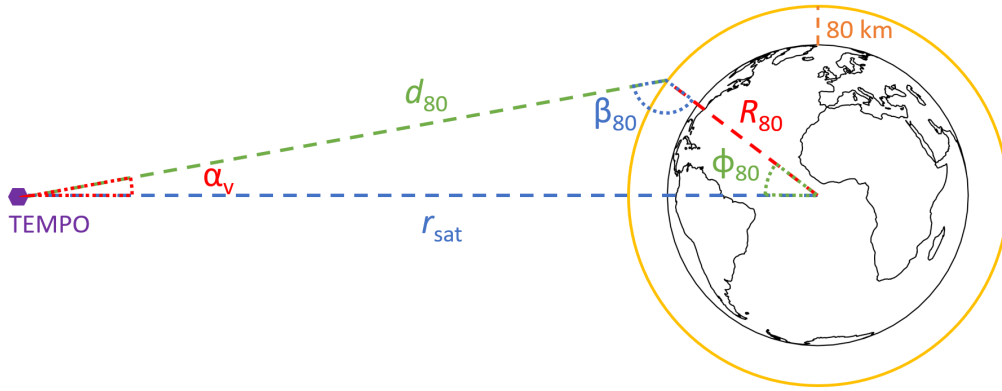
For the same triangle, the angle between the line from TEMPO to the center of the Earth and the TEMPO LOS, α_v , is found using the sine law as follows.

$$\begin{aligned} \frac{\sin \alpha_v}{R_0} &= \frac{\sin \phi_0}{d_0} \\ \alpha_v &= \arcsin\left(\frac{R_0}{d_0} \sin \phi_0\right) \\ &\approx 7.864^\circ. \end{aligned} \quad (\text{A.3})$$

Consider the triangle formed between TEMPO, the center of the Earth, and the LOS intersection with 80-km altitude (Fig. A.1(b)). The angle between the LOS and the line from the



(a) Ground intersection



(b) 80-km altitude intersection

Figure A.1. Geometry of TEMPO line of sight atmospheric intersections when measuring towards the Canadian Oil Sands. Lengths and angles are not to scale.

center of the Earth to the LOS-80-km-altitude intersection, β_{80} , is calculated using the sine law as follows.

$$\frac{\sin \alpha_v}{R_{80}} = \frac{\sin \beta_{80}}{r_{\text{sat}}}$$

$$\beta_{80} = 180^\circ - \arcsin\left(\frac{r_{\text{sat}}}{R_{80}} \sin \alpha_v\right) \quad (\text{A.4})$$

$$\approx 116.611^\circ,$$

where the $\arcsin()$ term is subtracted from 180° as $\arcsin(x)$ is defined with range $(-90^\circ, 90^\circ]$ and $\beta_{80} > 90^\circ$. Finally, the latitude below the LOS-80-km-altitude intersection point is

$$\phi_{80} = 180^\circ - \alpha_v - \beta_{80} \quad (\text{A.5})$$

$$\approx 55.526^\circ.$$

Thus, the difference in latitude between the two LOS intersections is approximately $\phi_0 - \phi_{80} \approx 1.5^\circ$.

Appendix B

Time Offset Between MLS and OMI Measurements Over the Same Geographic Location

Fig. B.1 depicts the geometry of MLS and OMI measurements at some time t_0 , as well as the position of Aura after a time interval t_{offset} , with lengths exaggerated for demonstration purposes. The Earth is approximated as a sphere with a radius (r_{Earth}) equal to the average Earth radius. The Aura orbit is approximated as a perfectly circular orbit concentric with the Earth, with an of altitude r_{sat} . This assumption is reasonable as the perigee and apogee only differ by around 3 km (Peat, n.d.). As OMI viewing zenith angles are generally low, it is assumed that OMI is always measuring straight down towards the Earth.

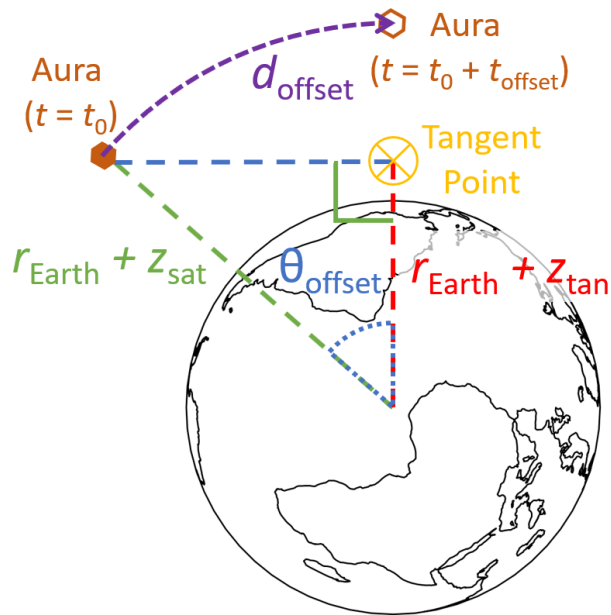


Figure B.1. Depiction of Aura linear distance offset and angular offset between an MLS tangent-point measurement at time $t = t_0$ and the point at time $t = t_0 + t_{\text{offset}}$ where OMI measures over the tangent-point latitude and longitude of said MLS measurement. r_{Earth} is the average radius of the Earth, z_{sat} is the average altitude of the Aura satellite above the mean Earth radius, and z_{tan} is the tangent-point altitude at time $t = t_0$. Lengths and angles are not to scale.

At time t_0 , OMI is measuring straight down (green dashed line in Fig. B.1) and MLS is measuring across the limb of the Earth in front of Aura (blue dashed line in Fig. B.1) with

tangent-point altitude z_{tan} . Over time interval t_{offset} , Aura travels along an orbit arc length of d_{offset} (dashed purple line in Fig. B.1), or an orbital angular distance of θ_{offset} . At this point (time $t_0 + t_{\text{offset}}$), Aura is directly above the tangent point of time t_0 and OMI is measuring towards the corresponding tangent-point latitude and longitude. The time interval t_{offset} corresponds to the expected time offset between MLS and OMI measurements over the same geographic coordinates, and can be calculated as

$$t_{\text{offset}} = \frac{d_{\text{offset}}}{v_{\text{sat}}}, \quad (\text{B.1})$$

where v_{sat} is the Aura satellite linear speed. The Aura linear speed can be approximated as

$$v_{\text{sat}} = \frac{2\pi (r_{\text{Earth}} + z_{\text{sat}})}{T}, \quad (\text{B.2})$$

where T is the Aura satellite orbital period. The Aura orbit arc length distance offset and angular offset can be calculated as

$$\begin{aligned} d_{\text{offset}} &= (r_{\text{Earth}} + z_{\text{sat}}) \theta_{\text{offset}}, \text{ and} \\ \theta_{\text{offset}} &= \arccos \left(\frac{r_{\text{Earth}} + z_{\text{tan}}}{r_{\text{Earth}} + z_{\text{sat}}} \right), \end{aligned} \quad (\text{B.3})$$

respectively. Substituting Eqs. (B.2) and (B.3) into Eq. (B.1) results in

$$t_{\text{offset}} = \left(\frac{T}{2\pi} \right) \arccos \left(\frac{r_{\text{Earth}} + z_{\text{tan}}}{r_{\text{Earth}} + z_{\text{sat}}} \right). \quad (\text{B.4})$$

Take the average Earth radius (r_{Earth}) as 6 371 km, z_{sat} as the average Aura altitude above the mean Earth surface height (705 km), and the Aura orbital period (T) as 98.8 minutes (Waters et al., 2006). The tangent altitude (z_{tan}) for MLS ozone retrievals is between 0 and 60 km. The time offset for the extreme tangent altitudes of 0 km and 60 km is 7.08 minutes and 6.77 minutes, respectively. The average between these two extremes is approximately 6.9 minutes. Thus, it can be assumed that OMI measures over the tangent point geographic location approximately 6.9 minutes after MLS has measured data for said tangent point.